# ELASTIC RELAXATION AND INCIPIENT PLASTICITY AT VICINAL SURFACES OF COPPER AND NICKEL STUDIED BY MOLECULAR STATICS AND DYNAMICS SIMULATIONS

Nuša Pukšič

**Doctoral Dissertation**
**Jožef Stefan International Postgraduate School**
**Ljubljana, Slovenia**

**Supervisor:** Prof. Dr. Monika Jenko, Institute of Metals and Technology, Lepi pot 11, Ljubljana, Slovenia
**Co-Supervisor:** Assist. Prof. Dr. Matjaž Godec, Institute of Metals and Technology, Lepi pot 11, Ljubljana, Slovenia

**Evaluation Board:**
Prof. Dr. Maja Remškar, Chair, Jožef Stefan Institute, Jamova cesta 39, Ljubljana, Slovenia
Assist. Prof. Dr. Igor Belič, Member, Institute of Metals and Technology, Lepi pot 11, Ljubljana, Slovenia
Prof. Dr. Christian Teichert, Member, Montanuniversitaet Leoben, Franz-Josef-Straße 18, Leoben, Austria

MEDNARODNA PODIPLOMSKA ŠOLA JOŽEFA STEFANA
JOŽEF STEFAN INTERNATIONAL POSTGRADUATE SCHOOL




Nuša Pukšič

# ELASTIC RELAXATION AND INCIPIENT PLASTICITY AT VICINAL SURFACES OF COPPER AND NICKEL STUDIED BY MOLECULAR STATICS AND DYNAMICS SIMULATIONS

**Doctoral Dissertation**

# ELASTIČNA RELAKSACIJA IN ZAČETKI PLASTIČNE DEFORMACIJE SOSEDNJIH POVRŠIN BAKRA IN NIKLJA, OBRAVNAVANIH Z MOLEKULARNO STATIKO IN DINAMIKO

**Doktorska disertacija**

**Supervisor:** Prof. Dr. Monika Jenko

**Co-Supervisor:** Assist. Prof. Dr. Matjaž Godec

Ljubljana, Slovenia, 2017

# Acknowledgments

This thesis was funded by the Slovenian Research Agency (ARRS).

I would like to express my sincere gratitude to my supervisor Prof. Dr. Monika Jenko and my co-supervisor Assist. Prof. Dr. Matjaž Godec for the opportunity, support and help.

My gratitude also goes to Sonja Jalševac for her care and detailed organizing.

My sincere thanks goes to Dr. Paul J McGuiness for his help writing the articles related to this thesis and for language editing.

On a more personal level, my thanks goes to Andrej, and to my parents for guidance, support, encouragement and open doors, and to my sister Eva as well as Katja, Katarina, Barbara, Irena, Darja, Nataša and Igor for lively and fruitful conversations.

# Abstract

While a lot is known about the deformation of metallic surfaces from experiments, elasticity theory and simulations, this investigation represents the first molecular-dynamics-based simulation of uniaxial deformation for the vicinal surfaces of copper and nickel. These vicinal surfaces are composed of terraces divided by equidistant, mono-atomic steps. The periodicity of vicinals makes them good candidates for a study of the influences of surface steps on surface dynamics.

To minimize the surface energy, atoms in the near-surface region are displaced and in the cases of vicinal surfaces form complex displacement fields spanning multiple layers into the bulk. The displacement fields in turn lead to elastic fields in the near-surface region that are material-dependent and specific for each surface orientation with alternating regions of compressive and tensile strains. The influence of the displacements of the near-surface atoms on the deformation mechanisms of vicinal surfaces was investigated by uniaxial deformation of two sets of surfaces: (1 1 19) vicinal to (001), and (9 9 11) and (10 10 8), both vicinal to (111). In addition to having different terrace orientations, steps also have distinct microfacets. The (1 1 19) surface has (111) oriented step microfacets, while the (9 9 11) surface has (001) oriented microfacets, also called A-step, and the (10 10 8) surface has $(\overline{1}\overline{1}1)$ oriented microfacets, also called B-step.

In the cases of the (1 1 19) surfaces, deformation mechanisms are dependent on the material as well as the strain polarity. Most notably, bulk dislocation nucleation sites exist in nickel, but not in copper.

In the cases of the investigated surfaces vicinal to (111), copper and nickel have analogous deformation mechanisms, while deformation mechanisms vary with respect to the surface orientation and polarity of strain.

We conclude that the displacement fields of vicinal surfaces play a role in the deformation mechanisms of vicinal surfaces.

The material-dependent positioning and activity of the nucleation sites are particularly noticeable in the cases of the (1 1 19) surfaces, where dislocations nucleate at the surface steps in copper, while in nickel dislocations form in the bulk in tensile deformation and in the bulk as well as at the steps in compressive deformation.

The influence of the polarity of the strain is noticeable in all the cases through the yield-stress asymmetry exhibited by both materials. In multiple cases it is additionally emphasized by the difference in the deformation mechanisms, of which the most glaring example are the (10 10 8) surfaces, that only deform by the parallel stacking faults aligned with the steps in compressive deformation, but not in tensile deformation.

The deformation mechanisms are very much dependent on the inclination of the strain axis as is evidenced by the comparison of the deformation mechanisms of the three vicinal surfaces. For instance, we have observed twinning in the deformation of (1 1 19) surfaces, but not in the other cases. In addition, as was expected from the values of their stacking-fault energies, transitions of the deformation mechanisms from dislocation emission to stacking-fault nucleation to twinning occur at smaller strains in copper than in nickel.

# Povzetek

Čeprav o deformaciji kovinskih površin veliko vemo iz eksperimentov, teorije elastičnosti in simulacij, je to prva raziskava deformacije sosednjih površin bakra in niklja z metodo molekularne dinamike. Sosednje površine sestavljajo terase, predeljene z enoatomnimi stopnicami. Zaradi periodičnosti so sosednje površine primerne za raziskovanje vpliva stopnic na dinamiko površine.

Da minimizirajo površinsko energijo, se atomi v okolici površine premaknejo in v primeru sosednjih površin ustvarijo polje premikov, ki se razteza več plasti v notranjost materiala. Polja premikov ustvarijo elastična polja, katerih oblika je odvisna od materiala in od orientacije površine. Vpliv polja premikov na mehanizme deformacije sosednjih površin smo raziskali z eno-osno deformacijo dveh setov sosednjih površin: (1 1 19), ki je sosednja (001), ter (9 9 11) in (10 10 8), ki sta sosednji (111). Izbrane površine imajo tudi različno orientirane stranice teras, in sicer ima površina (1 1 19) stranice z normalo (111), površina (9 9 11) stranice z normalo (001), imenovane stopnica A, in površina (10 10 8) ima stranice z normalo $(\overline{1}11)$, imenovane stopnica B.

In addition to having different terrace orientations, steps also have distinct microfacets. The (1 1 19) surface has (111) oriented step microfacets, while the (9 9 11) surface has (001) oriented microfacets, also called A-step, and the (10 10 8) surface has $(\overline{1}11)$ oriented microfacets, also called B-step.

V primeru (1 1 19) površin so mehanizmi deformacije odvisni od materiala in od polaritete raztezka. Recimo, dislokacije se v niklju porajajo tudi pod površino, v bakru pa ne.

V primeru površin sosednjih (111), imata baker in nikelj analogne mehanizme deformacije, ki pa so različni za različne orientacije površine in glede na polariteto raztezka.

Prišli smo do zaključka, da polja premikov vplivajo na mehanizme deformacije sosednjih površin.

Da sta položaj in aktivnost centrov, kjer se porajajo dislokacije, odvisna od materiala, je opazno na primeru (1 1 19) površin, kjer se dislokacije porajajo izključno ob stopnicah na površini v bakru, medtem ko se v niklju porajajo več atomskih plasti pod površino pri raztezanju in hkrati ob stopnicah na površini in v notranjosti pri krčenju.

Vpliv polaritete raztezka je opazen v vseh primerih v razliki med mejo plastičnosti pri raztezanju in krčenju. V več primerih je dodatno poudarjena z razliko med mehanizmi deformacije, ki je najbolj izražena na primeru (10 10 8) površin, ki se deformirajo s serijo vzporednih napak zloga, poravnanih s stopnicami na površini, pri krčenju, a ne pri raztezanju.

Da so mehanizmi deformacije odvisni od naklona raztezka, je razvidno iz primerjave vseh treh sosednjih površin. Recimo, dvojčenje se pojavi pri deformaciji (1 1 19) površin, ampak ne v drugih primerih. Prav tako, kot je bilo pričakovati iz vrednosti energije napake zloga za baker in nikelj, se prehodi med mehanizmi deformacije iz porajanja dislokacij v napake zloga v dvojčenje zgodijo v bakru pri nižjih raztezkih kot pri niklju.

# Contents

**List of Figures** xiii

**List of Tables** xv

**List of Algorithms** xvii

**Abbreviations** xix

**Symbols** xxi

**1 Introduction** 1
- 1.1 Motivation . . . 1
- 1.2 Hypotheses . . . 3
- 1.3 Research Objective . . . 4
- 1.4 Significance of This Research . . . 4

**2 Background** 7
- 2.1 Stress and Strain . . . 7
- 2.2 Elastic Description of Surfaces . . . 8
  - 2.2.1 Surface stress of flat surfaces . . . 8
  - 2.2.2 Elastic description of vicinal surfaces . . . 9
- 2.3 Defects and Plastic Deformation in Metallic Materials . . . 10
  - 2.3.1 Point defects . . . 11
  - 2.3.2 Line defects . . . 11

**3 Simulation Methodology** 13
- 3.1 Introduction to Molecular Dynamics Simulations . . . 13
- 3.2 Materials . . . 14
- 3.3 Software . . . 16
- 3.4 Substrates' Configuration . . . 16
- 3.5 Minimization . . . 19
- 3.6 Equilibration . . . 20
- 3.7 Simulations of Deformation . . . 20

**4 Elastic Fields of Vicinal Surfaces** 23
- 4.1 Relaxation and Elastic Strain of Low-Index Surfaces . . . 23
- 4.2 Relaxation of Vicinal Surfaces . . . 24
  - 4.2.1 Displacement fields . . . 24
  - 4.2.2 Elastic strain . . . 27

**5 Plastic Deformation** 37
- 5.1 Plastic deformation of the (001) and (1 1 19) surfaces . . . 37

5.1.1 Tensile deformation . . . 40
5.1.2 Compressive deformation . . . 42
5.1.3 Summary . . . 44
5.2 Plastic deformation of the (111) surface and its vicinals, (9 9 11) and (10 10 8) . . . 45
5.2.1 Tensile deformation . . . 45
5.2.1.1 (9 9 11) . . . 45
5.2.1.2 (10 10 8) . . . 49
5.2.2 Compressive deformation . . . 50
5.2.2.1 (9 9 11) . . . 51
5.2.2.2 (10 10 8) . . . 52
5.2.3 Summary . . . 55

**6 Conclusions** **57**
6.1 Contribution to Science . . . 57
6.2 Outlook . . . 58

**Appendix A LAMMPS Script: Minimization** **61**

**Appendix B LAMMPS Script: Equilibration** **63**

**Appendix C LAMMPS Script: Deformation** **65**

**Appendix D Article: A comparison of the uniaxial deformation of copper and nickel (1 1 19) surfaces: a molecular dynamics study** **67**

**Appendix E Article: Molecular dynamics simulations of plastic deformation of metallic surfaces** **77**

**References** **83**

**Bibliography** **89**

**Biography** **91**

# List of Figures

Figure 2.1: A schematic representation of the surface step. . . . . 10
Figure 2.2: A reduced representation of the surface step. . . . . 10

Figure 3.1: Substrate orientation within simulation box for **z** = (1 1 19). . . . . 17
Figure 3.2: Substrate orientation within simulation box for the (111) vicinals. . . . 18
Figure 3.3: Substrate orientation within simulation box for **z** = (19 19 1). . . . . 18
Figure 3.4: Step microfacets of the (1 1 19) and (19 19 1) vicinal surfaces. . . . . 19
Figure 3.5: Step microfacets of the (9 9 11) and (10 10 8) vicinal surfaces. . . . . 20

Figure 4.1: A schematic representation of the surface atoms. . . . . 24
Figure 4.2: Displacement fields of Cu and Ni (1 1 19) vicinal surfaces. . . . . 26
Figure 4.3: Displacement fields of Cu and Ni (9 9 11) vicinal surfaces. . . . . 27
Figure 4.4: Displacement fields of Cu and Ni (10 10 8) vicinal surfaces. . . . . 28
Figure 4.5: Displacement fields of Cu and Ni (19 19 1) vicinal surfaces. . . . . 29
Figure 4.6: Displacements in the $z$ direction of Cu and Ni (1 1 19) vicinal surfaces at 0 K. . . . . 30
Figure 4.7: Displacements in the $z$ direction of Cu and Ni (9 9 11) and (10 10 8) surfaces at 0 K. . . . . 31
Figure 4.8: Displacements in the $z$ direction of Cu and Ni (19 19 1) surfaces at 0 K. 32
Figure 4.9: Elastic strain field $\epsilon_{zz}$ of Cu and Ni (1 1 19) vicinal surfaces. . . . . 33
Figure 4.10: Elastic strain field $\epsilon_{zz}$ of Cu and Ni (9 9 11) vicinal surfaces. . . . . 33
Figure 4.11: Elastic strain field $\epsilon_{zz}$ of Cu and Ni (10 10 8) vicinal surfaces. . . . . 33
Figure 4.12: Elastic strain field $\epsilon_{zz}$ of Cu and Ni (19 19 1) vicinal surfaces. . . . . 34
Figure 4.13: Elastic strain field $\epsilon_{zy}$ of Cu and Ni (1 1 19) vicinal surfaces. . . . . 34
Figure 4.14: Elastic strain field $\epsilon_{zy}$ of Cu and Ni (9 9 11) vicinal surfaces. . . . . 34
Figure 4.15: Elastic strain field $\epsilon_{zy}$ of Cu and Ni (10 10 8) vicinal surfaces. . . . . 35
Figure 4.16: Elastic strain field $\epsilon_{zy}$ of Cu and Ni (19 19 1) vicinal surfaces. . . . . 35

Figure 5.1: Stress-strain curves of Cu and Ni (001) and (1 1 19) surfaces. . . . . 38
Figure 5.2: Deformation evolution of Cu(1 1 19) deformed in tension. . . . . 40
Figure 5.3: Deformation evolution of Ni(1 1 19) deformed in tension. . . . . 41
Figure 5.4: Deformation evolution of Cu(1 1 19) deformed in compression. . . . . 43
Figure 5.5: Deformation evolution of Ni(1 1 19) deformed in compression. . . . . 44
Figure 5.6: Stress-strain curves of Cu and Ni (111), (9 9 11) and (10 10 8) surfaces. 46
Figure 5.7: Tensile deformation of the Cu(9 9 11) surface. . . . . 47
Figure 5.8: Tensile deformation of the Ni(9 9 11) surface. . . . . 48
Figure 5.9: Tensile deformation of the Cu(10 10 8) surface. . . . . 49
Figure 5.10: Tensile deformation of the Ni(10 10 8) surface. . . . . 50
Figure 5.11: Compressive deformation of the Cu(9 9 11) surface. . . . . 51
Figure 5.12: Compressive deformation of the Ni(9 9 11) surface. . . . . 52
Figure 5.13: Compressive deformation of the Cu(10 10 8) surface. . . . . 53

Figure 5.14: Compressive deformation of the Ni(10 10 8) surface. . . . . 54

# List of Tables

Table 2.1: Typical values of stacking-fault energy. . . . . 12

Table 3.1: Axis vectors and primary slip systems with Schmid factors for simulated substrates. . . . . 17

Table 4.1: Atomic relaxation of the low-index surfaces at 0 K. . . . . 23
Table 4.2: Magnitudes of displacements of step edge atoms. . . . . 25

Table 5.1: Roughness profiles for Cu and Ni (1 1 19) vicinals. . . . . 39

# List of Algorithms

Algorithm A.1: A sample LAMMPS script for the minimization of surface energy. . 61

Algorithm B.1: A sample LAMMPS script for equilibration to 10 K. . . . . 63

Algorithm C.1: A sample LAMMPS script for simulations of deformation. . . . . 65

# Abbreviations

| | | |
|---|---|---|
| Al | ... | aluminum |
| Au | ... | gold |
| BCC | ... | body-centered cubic |
| Cu | ... | copper |
| EAM | ... | embedded atom method |
| FCC | ... | face-centered cubic |
| FIB | ... | focused ion beam |
| GB | ... | grain boundary |
| LAMMPS | ... | Large-scale Atomic/Molecular Massively Parallel Simulator |
| MD | ... | molecular dynamics |
| nc | ... | nanocrystalline |
| Ni | ... | nickel |
| ns | ... | nanoscale |
| NPT | ... | ensemble with a constant number of particles $N$, pressure $P$ and temperature $T$ |
| NVE | ... | ensemble with a constant number of particles $N$, volume $V$ and energy $E$ |
| NVT | ... | ensemble with a constant number of particles $N$, volume $V$ and temperature $T$ |
| OVITO | ... | Open Visualization Tool |
| Pt | ... | platinum |
| sd | ... | steepest descent algorithm |
| SFE | ... | stacking fault energy |
| Si | ... | silicone |
| TEM | ... | transmission electron microscopy |

# Symbols

| | | |
|---|---|---|
| $a$ | ... | step width |
| $a_0$ | ... | lattice constant |
| $\boldsymbol{a}$ | ... | acceleration |
| $A_0$ | ... | original cross-section |
| $\mathbf{b}$ | ... | Burgers vector |
| $C_{\mathrm{S}}$ | ... | centro-symmetry parameter |
| $D_{ij}$ | ... | Green tensor |
| $E$ | ... | the modulus of elasticity or Young's modulus |
| $E_i$ | ... | total energy of an atom $i$ |
| $\boldsymbol{F}$ | ... | force |
| $F(\rho)$ | ... | embedding energy |
| $h$ | ... | step height |
| $k_B$ | ... | Boltzmann's constant |
| $L$ | ... | simulation box length |
| $L_0$ | ... | initial simulation box length |
| $M$ | ... | mass matrix |
| $m$ | ... | Schmid factor |
| $\mathbf{n}_s$ | ... | strain direction |
| $P$ | ... | applied load |
| $R$ | ... | strain rate |
| $R_{\mathrm{a}}$ | ... | arithmetic average of absolute values |
| $r_{ij}$ | ... | interatomic distance |
| $\rho$ | ... | atomic electron density |
| $S_A$ | ... | surface area |
| $S_{AB}$ | ... | interfacial area between two homogeneous phases A and B |
| $\mathbf{s}_P$ | ... | slip plane normal |
| $\mathbf{s}_D$ | ... | slip direction |
| $T$ | ... | temperature |
| $\Delta t$ | ... | timestep |
| $U$ | ... | potential |
| $u$ | ... | displacement |
| $V$ | ... | volume |
| $\boldsymbol{v}$ | ... | velocity |
| $W$ | ... | elastic energy |
| $w_2(i)$ | ... | pair-wise potential |
| $w_3(i,j)$ | ... | triplet term in the potential |
| $\delta W^{\mathrm{interf}}$ | ... | interfacial elastic energy change |
| $z_m$ | ... | median $z$ coordinate |
| $\delta(x)$ | ... | Dirac function |
| $\epsilon$ | ... | strain |

$\epsilon_e$ ... engineering strain
$\mathbf{\Gamma}$ ... torque
$\nu$ ... Poisson's ratio
$\sigma$ ... stress
$\boldsymbol{\sigma}$ ... point force
$\sigma_e$ ... engineering stress
$\sigma_y$ ... yield strength

# Chapter 1

# Introduction

## 1.1 Motivation

Interfaces play a vital role in the bulk properties of crystalline materials. The role is even more pronounced in nanocrystalline (nc) or nanoscale (ns) materials in which the ratio of surfaces to bulk increases.

In the past 20 years investigations of stress and strain effects in the field of surface physics have become increasingly important as the manufacture of nc and ns materials and devices has become more widespread, leading to studies based on a combination of theoretical, computational and experimental investigations [1]. As a result, the definitions of surface stress and surface strain that allow for numerical thermodynamic studies based on atomistic models have now been established, and elastically mediated interactions between various surface defects, such as "steps" and "islands", have been described [1].

The hardness of low-index surfaces compared to the underlying bulk material was investigated, showing that surface effects are noticeable for nanoscale materials. The mechanical properties of vicinal surfaces are additionally affected by the steps on the surface and the elastic fields generated by the relaxation of the near-surface atoms. Vicinal surfaces are produced by cutting a crystal close to a dense plane, and consist of terraces divided by equidistant monoatomic steps. When cutting or growing polycrystalline materials, such surfaces are unavoidable. As is the case with grain boundaries, the steps on the surface may provide favorable nucleation sites for dislocations and stacking faults, key elements of plastic deformation. This dissertation centers on the plasticity of low-index and vicinal surfaces in face-centered cubic (FCC) materials, with a specific focus on the nucleation of defects at surfaces of copper and nickel.

Due to the lack of bonds on the surfaces of metallic materials the atoms close to the surface tend to relax from their bulk positions to better accommodate this lack, with either a contraction or a dilation of the interlayer distances. In some extreme cases the surfaces reconstruct and form a pattern that is distinctly different from the bulk symmetry of the material. The elastic fields that arise from the relaxation of vicinal surfaces were studied by molecular statics and dynamics simulations for a range of FCC metals: Cu, Ni, Au, Pt, Al [1]–[8]. The displacements follow a similar pattern in all the cases: the corner atoms and the terrace edge atoms are displaced the most and in opposite directions, the rest of the atoms gradually approach the bulk positions and the displacements form vertices beneath the terraces. The placement of the vertices and the amplitude of the displacements vary with regard to the metallic material considered and also with regard to the low-index surface orientation and width of the terraces in each case. It is expected that this diversity translates into a diversity of responses to deformation as is the case for grain boundaries with diverse misorientation angles. For example, in homoepitaxial growth, steps on a

surface can act as nucleation centres by influencing the diffusion of adsorbed species, while in catalytic reactions stepped surfaces often have a different catalytic activity to that of flat surfaces [4], [9]–[13]. Controlled deformation also appears to be a potential tool for the self-organization of surfaces, applicable in a bottom-up approach to the nanostructuring of materials.

Elasticity also provides pressure maps that can help predict the stress release resulting from atomic rearrangements[1]; however, on the subject of vicinal surfaces under an externally applied stress the data from both experiments and simulations are scarce.

Experiments on the nanoscale can be very time-consuming and costly, requiring expensive equipment, particularly sensors; however, they confirm an array of unusual mechanical properties of ns materials [14]. This serves as a motivation to use atomistic simulations in order to better understand the deformation mechanisms on the nanoscale. In previous studies of the mechanical properties of nc materials and thin films by molecular statics and dynamics, most of the research was centered on the influence of phase and grain boundaries on the response of the material to an external load or deformation. And when molecular dynamics (MD) simulations of the plastic deformation of nc materials are considered, the focus is mainly on the generation of dislocations at the grain boundaries (GBs) and the effectiveness of the grain boundaries (GBs) in slowing the rate of plastic deformation [15]–[19].

In polycrystals with a grain size on the micron scale dislocations are nucleated and emitted within grains, mostly in areas with prior defect content or impurities [20]. As the grain size decreases, the emission of dislocations from the GBs becomes important [20], [21]. Further, below a certain critical grain size, usually on the order of 10 nm, dislocation nucleation becomes limited while grain-boundary sliding and grain rotation become dominant deformation mechanisms [20].

With the rapid rise of computational capabilities, atomic simulations of plasticity phenomena in some cases preceded the experimental observation of the same phenomena [21]. Yamakov and coworkers [22], [23] predicted deformation twinning in aluminum with molecular dynamics simulations before the experimental TEM evidence of deformation twinning in nc Al was gathered by Chen and colleagues [24]. However, a clear understanding of the deformation mechanisms at the nanoscale are vital to the design and reliability of engineered nanodevices.

In the studies of mechanical properties of nc materials and thin films by molecular statics and dynamics most of the research is centered on the influence of phase and grain boundaries on the response of a material to external load or deformation. In nc materials free surfaces are ignored as the surface-to-bulk ratio is small and the influence of the surfaces on the mechanical properties is limited. In the case of thin films low-index surfaces - (001), (110) and (111) - are investigated in a vast majority of the cases. In the case of nc materials, deformation is most often induced by uniaxial or biaxial deformation. In the case of thin films, the studies of nano-indentation are the most common.

When plastic deformation of nc materials is considered, the focus is mainly on the generation of defects at the GBs and their effectiveness in slowing the rate of plastic deformation [15]–[18], [25], [26].

Nano-indentation studies focus on dislocation nucleation beneath the indenter. The stress is applied using a frictionless rigid indenter. Although the stress applied in this manner is nonuniform, it can lead to homogeneous defect nucleation in a perfect crystal. The substrates are thin films [27]–[29] with controlled impurities, i.e., vacancies [30], voids [31], grain boundaries [32] and steps [33]–[36], added in some cases.

As nanowires have a large surface-to-bulk ratio, the most comprehensive studies of the influence of free surfaces on the mechanical properties of metallic materials using molecular

dynamics were made with samples of nanowires [37]–[41]. For instance, in nanowires, the orientation of the surface can influence which deformations are energetically favorable, overriding the crystallographically preferred deformation mechanisms [40].

Molecular dynamics (MD) simulations serve as an effective tool for analyzing dislocation nucleation mechanisms in nc FCC materials [22], [23], [42]–[44]. The time- and length-scales of typical molecular dynamics calculations center the studies on diffusion, defects (their nucleation and interaction), and mechanical properties of nanowires, thin films and nanocrystalline samples. Thus, MD studies address questions on a range of topics: how equidistant steps and terraces could be used as templates or as nucleation sites, how precipitates nucleate and grow in a metallic matrix and how they interact with other defects, how mechanical properties depend on the surface condition of a sample or how the prevalent type of GBs in nc thin films can influence the mechanical properties, and more.

The most common metallic materials investigated are metals with the face-centered cubic (FCC) lattice: Cu, Ni, Al, Au, and Pt; and with the body-centered cubic (BCC) lattice: Fe. For these materials satisfactory potentials exist, which reproduce the properties of these metals as compared with the experimental results, which gives us confidence that the results of the simulations depict the actual behavior of the materials studied.

Although the relaxations of vicinal surfaces are recognized as important aspects of surface elasticity, and the local symmetry and order of a metallic material are known to influence the mechanical properties, there was very little effort put into the study of the combination of the two. In addition, although the importance of the surfaces for the deformation mechanism on the nano-scale was noted, only the effects of nominal surfaces were studied so far, with main focus on nanowires.

As the steps on the surface importantly influence the local distribution of atoms in the near-surface region, they are expected to have a pronounced effect on the mechanical response of the metallic thin films as well. In this study molecular dynamics simulations of copper and nickel thin films with vicinal surfaces under an externally applied uniaxial strain were performed and the beginning of plastic deformation was studied in order to determine the stability of the surface steps during deformation and their influence on the deformation mechanisms. The vicinal surfaces we chose all have a dense array of steps with terraces consisting of ten atomic rows, and yet the distances between the steps are large enough to ensure that the interaction between the steps is weak: the relaxations of the step edge atoms are only slightly modified by the presence of the other steps [4].

## 1.2 Hypotheses

In MD simulations, bicrystals are mainly used in the simulations of grain-boundary behavior and monocrystalline thin films or multilayered films are typical for the investigation of the surface effects, for example in MD simulations of nano-indentation.

Monocrystalline films were chosen for this research to isolate free surface effects from grain-boundary influences. Copper and nickel were chosen as two FCC metals with similar deformation mechanisms but noticeably different stacking fault energies (SFE). Vicinal surfaces were chosen in addition to the low-index surfaces as they present an interesting case for studying dislocation nucleation behavior because of the regular steps and terraces. Those form a displacement field that stretches several layers into the bulk and disrupts the lattice symmetry of the near-surface atoms. As lattice symmetry plays an important role in the deformation mechanisms of metals, we expect that this will impact on the deformation mechanisms of the vicinal surfaces.

To include material-specific properties in a molecular statics or dynamics simulation, potentials are used. As the fitting process is complex and different choices are available

for the fitting parameters, not all potentials are equally suitable for a specific simulation objective. Potentials by Mishin *et al.* for Ni [45] and by Mishin *et al.* for Cu [46] were chosen as they are widely used in similar studies.

In light of this, the following hypotheses were formed:

1. The elastic fields emerging on the vicinal surfaces due to the presence of equidistant steps disrupt the lattice symmetry of the near-surface atoms and play a role in the response of the surfaces to uniaxial tensile and compressive strains, leading to material-dependent positioning and activity of the nucleation sites.

2. The required strain and mechanisms of dislocation nucleation are different for tensile deformation compared to compressive deformation. In the case of vicinal surfaces, the same nucleation sites are activated at different strains and alternative nucleation sites exist.

3. Defect nucleation mechanisms at the onset of plasticity vary with regard to strain-axis inclination and are additionally influenced by the stacking-fault energy of a material. The stacking-fault energy of nickel is higher than that of copper. In light of this, any possible transitions of deformation mechanisms from dislocation emission to stacking-fault nucleation to twinning will occur at lesser strains in copper than in nickel.

## 1.3 Research Objective

The research objective of this dissertation is to use molecular statics and dynamics simulations to examine the structure and dislocation nucleation and emission behavior of low-index and vicinal surfaces in FCC copper and nickel. This is achieved by designing and performing systematic studies, based on the aforementioned hypotheses. LAMMPS Molecular Dynamics Simulator [47] is used for all the MD simulations.

The first hypothesis centers on describing the importance of surface steps and features in resulting elastic fields as nucleation sites. For this purpose structure and energetics of low-index and chosen vicinal surfaces are investigated and material-dependent features of the elastic fields of vicinal surfaces are identified. To minimize the energies of the surfaces and find the relaxed positions of the atoms in the near-surface region, the damped dynamics method is used [48].

To address the second hypothesis, uniaxial tensile and compressive strains are applied to the simulated samples. Materials are not equally resistant to tensile and compressive deformation. In this dissertation, special interest is taken in the stress required for activation of the nucleation sites at the vicinal surfaces and how nucleation and emission of dislocations are influenced by the polarity of the strain.

To evaluate the third hypothesis, two considerations are made. First, (001) and (111) surfaces with their vicinal(s) are chosen for the simulations, as the surface to strain-axis inclination changes from case to case. In this manner a wider range of dislocation nucleation mechanisms and the influence of the inclination angle can be evaluated. And secondly, two materials (copper and nickel) with different stacking-fault energies (SFE) are chosen.

## 1.4 Significance of This Research

The elastic fields of vicinal surfaces were studied by MD for a range of FCC metals: Cu, Ni, Au, Pt, Al [2]–[5]. For all the FCC metals studied, the displacements of atoms from their bulk positions form vertices beneath the terraces, reaching several layers into the bulk.

The placement of the vertices and the amplitude of the displacements vary with regard to the metal considered and also with regard to the nominal surface and terrace width of each case.

Steps interact with each other and the contributions can be of diverse origin [5]. Steps entropically repel, since two steps cannot cross each other [5]. Due to the displacement fields generated by the steps to achieve the minimal energy state of the crystal surface, steps interact elastically through these long-range relaxation fields generated by local atomic relaxations at the steps, as well as electronically through the modification of the density of states, electrostatically due to the presence of electrostatic dipoles at the steps, and thermally through the modification of their vibrational free energy [5].

At low temperature, such as the 10 K at which our simulations were performed, entropic and phononic contributions are negligible and only electronic, electrostatic and elastic contributions have to be considered [5]. Electronic interactions decay exponentially [5], and already in the cases such as our chosen vicinals steps interact only electrostatically or elastically. Generally, for metallic surfaces the elastic interaction energy is much higher than the electrostatic contribution [5].

Elastic constants near surfaces are different from their values in the bulk of solids [1], influenced by the lower coordination of the surface. Atomistic calculations show that inhomogeneity such as atomic steps near the indented surface can appreciably reduce the nucleation stress in nano-indentation. Nano-indentation of Au(111) near a step showed that the plane in which dislocation loops form changes with respect to the distance from a step [33].

Our research shows that vicinal surfaces are in general softer than the bulk and deform at lower stress than the bulk.

Our research also shows that a switch in active slip systems is possible in the case of vicinal surfaces deformed with uniaxial loading, but that it occurs for specific orientations of the surfaces and strains.

Using copper, a comparison was made of two geometries: a film and a line [18]. The bottom of the films was constrained by the film/substrate interface, but the sidewall surfaces of the lines were free to deform [18]. The indentation penetration depth decreased as the film thickness decreased for the continuous films, whereas the penetration depth increased as the line width decreased for the patterned lines [18].

The deformation of single crystal metal nanowires, with various crystallographic orientations loaded in tension and compression, was investigated by Park *et al.* [41]. The effects of free surfaces on the deformation modes were demonstrated by the compressive deformation of (100){100} and (100){110} wires, which have identical (100) normal orientations but different side surfaces. The (100){100} wires deform by twinning, but in the (100){110} wires, twins are geometrically prevented from forming low energy {111} side surfaces, thus one of the driving forces for twinning is reduced, and twins are not observed [41]. Instead, partial dislocations and dispersed stacking faults with various orientations form [41].

The disparity in the yield strengths observed in tension versus compression, also called the yield strength asymmetry, is due to the different deformation mechanisms operating under tension versus compression as well as the effect of tensile surface stresses [41]. The yield stress asymmetry is driven by the energy barriers for the nucleation of partial dislocations or full dislocations or twins and crystallography of different inelastic deformation mechanisms observed in tension versus compression, meaning that the energy barriers depend on the angles between the strain axis and main crystallographic directions in the sample as well as the constraints posed by free surfaces or other boundaries.

The thin films in our research also exhibited a significant yield stress asymmetry that

was due to the differences in the deformation mechanisms observed in tension versus compression.

In light of the research presented here, this thesis extends the field of study into the plasticity of vicinal surfaces of metallic thin films under uniaxial loading.

# Chapter 2

# Background

## 2.1 Stress and Strain

Stress $\sigma$ and strain $\epsilon$ are used as measures of deformation. For materials that are stressed at relatively low levels, for metallic materials this is to strains of about 0.005, stress $\sigma$ and strain $\epsilon$ are proportional to each other [49],

$$\sigma = E\epsilon. \tag{2.1}$$

This is Hooke's law, and E (GPa) is the modulus of elasticity, or Young's modulus, and is a measure of the interatomic bonding forces [49].

In metals permanent deformation is accomplished by slip, which is a process that involves the motion of dislocations [49]. From atomistic perspective, plastic deformation corresponds to the breaking of bonds with original atom neighbors and then reforming bonds with new neighbors after a large number of atoms have moved relative to one another. When external stress is removed, the atoms cannot return to their original positions.

For metals that experience a gradual transition from the elastic to plastic regime, the point of yielding may be determined as the initial departure from linearity of the stress–strain curve. By convention a straight line is drawn parallel to the elastic portion of the stress–strain curve at the strain offset of 0.002. The stress corresponding to the intersection of this line and the stress–strain curve as it bends away form linearity is defined as the yield strength $\sigma_y$ [49].

For some materials the elastic–plastic transition is very well defined and occurs abruptly [49]. At the upper yield point, the start of plastic deformation is accompanied by an actual decrease in stress. With continued deformation the stress fluctuates slightly about some constant value, called the lower yield point. For metals that behave this way, the yield strength is taken as equal to the the lower yield point, since it is well defined and relatively insensitive to the testing procedure.

In our study the abrupt elastic-plastic transition is the norm.

When a metal thin film is subjected to uniaxial tension or compression its length will tend to elongate or shorten, and its cross-sectional area will change by an amount that depends on the Poisson's ratio $\nu$ of the material. When the cross-sectional area is assumed constant during deformation, the stress is called engineering stress and is calculated using the original cross-section of the thin film [49]:

$$\sigma_{\mathrm{e}} = \frac{P}{A_0} \tag{2.2}$$

where $P$ is the applied load, and $A_0$ is the original cross-sectional area.

In this study, the simulations of the tensile and compressive uniaxial deformations were performed at 10 K, applying engineering strain at a strain rate of $\pm$ 2.5% ps$^{-1}$. For details see Section 3.7.

## 2.2 Elastic Description of Surfaces

Although elasticity theory mostly centers on continuum description of materials, it nevertheless allows us to describe surfaces and even elastically mediated interactions among various surface defects such a steps and islands. The strain fields induced by various surface defects can profoundly affect the morphology of the surface [1].

Elasticity provides pressure maps which help predict stress release upon atomic rearrangements, for example during slip. Elasticity also appears to be a potential tool for self-organization of surfaces applicable in the bottom-up approach to nano-structuring of materials [1].

### 2.2.1 Surface stress of flat surfaces

Let us first consider an elastically strained flat surface. Elastic properties of such a surface can be described as excess quantities of bulk stress and strain [1]. We can extend any bulk elastic property of a material by a surface contribution. Other well-known excess interfacial quantities are for instance: the number of particles, the elastic constants, the entropy or the volume of the interfacial zone [1].

To demonstrate the principle of excess quantities, we consider two homogeneous phases A and B separated by an interface $S_{AB}$. We take the elastic energy as a model extensive quantity for which we may calculate the surface excess at the interface of the two materials. We can calculate the change in total elastic energy produced by an infinitesimal bulk deformation $\delta\epsilon_{ij}$ by [1]:

$$\delta W = \int_V \sum_{ij} \sigma_{ij}(z)\delta\epsilon_{ij}(z)\,\mathrm{d}V, \tag{2.3}$$

where $\sigma_{ij}$ and $\epsilon_{ij}$ are the components of the bulk stress and strain tensors.

The two homogeneous materials A and B are characterized by their own stress and strain tensors $\sigma_{ij}^m$ and $\epsilon_{ij}^m$ with $m$ =A,B. To proceed, we assume a gradual transition between their respective properties along the interface. We define the interfacial elastic energy change $\delta W^{\mathrm{interf}}$ as [1]:

$$\delta W^{\mathrm{interf}} = \int_{z_A}^{z_B} \sum_{ij} \sigma_{ij}(z)\delta\epsilon_{ij}(z)\,\mathrm{d}V - \sum_{ij} \sigma_{ij}^A(z)\delta\epsilon_{ij}^A(z)V^A - \sum_{ij} \sigma_{ij}^B(z)\delta\epsilon_{ij}^B(z)V^B, \tag{2.4}$$

where $\sigma_{ij}(z)$ and $\epsilon_{ij}(z)$ define the true bulk stress and strain profiles across the interface, $V^m$ are the volumes of the bulk phases extrapolated to the dividing surface.

Supposing there is no relative gliding between the materials during deformation and imposing mechanical equilibrium, which requires that the normal components of the stress tensor are homogeneous throughout the material, and also taking into account the orthogonality, we derive that the parallel components of the strain and the perpendicular components of the stress do not present interfacial excess [1] and can be expressed as:

$$\mathbf{s} = \begin{pmatrix} s_{11} & s_{12} & 0 \\ s_{21} & s_{22} & 0 \\ 0 & 0 & 0 \end{pmatrix}, \mathbf{e} = \begin{pmatrix} 0 & 0 & e_{13} \\ 0 & 0 & e_{23} \\ e_{31} & e_{32} & e_{33} \end{pmatrix}. \tag{2.5}$$

In the case when one phase is the vacuum, that has neither stress nor strain, the surface stress and strain can be given as [1]:

$$s_{ij}^{\text{surf}} = \frac{1}{S_A}\left[\int_{z_A}^{z_0} \sigma_{ij}^{||}(z)\,\mathrm{d}V - \sigma_{ij}^{||A}V^A\right], \tag{2.6}$$

$$e_{ij}^{\text{surf}} = \frac{1}{S_A}\left[\int_{z_A}^{z_0} \epsilon_{ij}^{\perp}(z)\,\mathrm{d}V - \epsilon_{ij}^{\perp A}V^A\right]. \tag{2.7}$$

The surface stress is in general non-zero even if there is no stress in the bulk. It can be positive (tensile stress) or negative (compressive stress). In addition, the value of the surface stress depends on the crystallographic face.

For nominal surfaces that do not reconstruct, the difference between the ideal and the actual surface plane equals the surface strain $e_{zz}^{\text{surf}} = u(z_0) - u^A(z_0)$. Surface strains for the nominal surfaces of the materials in this study are given in Section 4.1. The strains are compressive, and are largest for the (110) surfaces and smallest for the (111) surfaces.

The elastic energy change of a surface bordering on vacuum due to a small deformation parallel to the surface, $\delta\epsilon_{ij}^{||}$, depends only on the surface stress [1]:

$$\delta W^{\text{surf}} = S_A \sum_{ij} \delta\epsilon_{ij}^{||} s_{ij}^{\text{surf}}. \tag{2.8}$$

### 2.2.2 Elastic description of vicinal surfaces

Vicinal surfaces consist of terraces separated by equidistant steps of monotone height. The elastic interaction of steps is important for a consistent description of the properties of vicinal surfaces. The atoms belonging to step edges, and in some cases those belonging to step corners, have a different number of close neighbors than equivalent atoms in the bulk, see for instance the atomically resolved representations of the steps of vicinal surfaces used in this study, shown in Fig. 3.4 and Fig. 3.5. Thus, steps affect a lattice distortion that propagates from the step on the surface and into the bulk. The asymptotic displacement field due to the step can be calculated by continuum theory of elasticity but it diverges at the step [1]. Similarly, the displacement field can be calculated by molecular dynamics simulations, by finding the minimal energy state of the vicinal surface. The procedure used in our study is described in Section 3.5, and the results are given in Section 4.2.

Surface steps can be modeled using the concept of point forces [1]. This enables us to calculate the displacement fields of vicinal surfaces. The strain field induced by a single step adds to the strain field of other steps.

Let us consider a step on a vicinal surface whose terraces are normal to the **z** axis, the step is infinite in the **y** direction, has a width $a$ and a height $h$, see Fig. 2.1.

The simplest force distribution one can use is two point forces $\boldsymbol{\sigma}_a$ and $\boldsymbol{\sigma}_b$ applied at the upper and lower edge of the step:

$$\mathbf{F}(\mathbf{x}) = \boldsymbol{\sigma}_a\delta(x+a)\delta(z-h) + \boldsymbol{\sigma}_b\delta(x)\delta(y) \tag{2.9}$$

where $\delta(x)$ denotes the Dirac function. As the step is infinite $F_y = 0$.

To simplify, the model of a step is reduced to a set of forces applied to a planar surface, see Fig. 2.2. Two point forces separated by a distance $a$ give the following force distribution:

$$\mathbf{F}(\mathbf{x}) = \boldsymbol{\sigma}_a\delta(x+a)\delta(z) + \boldsymbol{\sigma}_b\delta(x)\delta(z). \tag{2.10}$$

Employing this force distribution and the Green tensor for a semi-infinite medium bounded by a planar surface, $D_{ij}(\mathbf{x}, \mathbf{x}')$, we derive the displacement field from [1]:

$$u_i(\mathbf{x}) = -\sum_j \int D_{ij}(\mathbf{x}, \mathbf{x}')F_j(\mathbf{x}')\,\mathrm{d}^3x'. \tag{2.11}$$

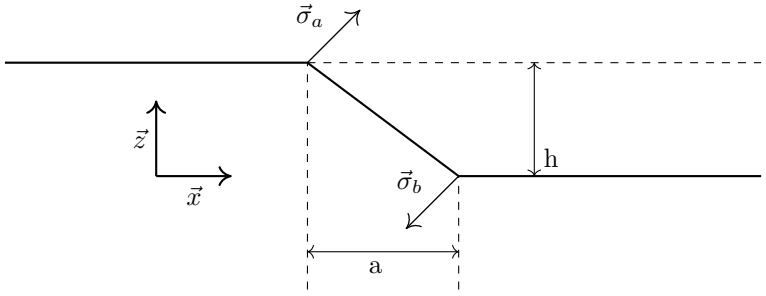



Figure 2.1: A schematic representation of the surface step of a width $a$ and a height $h$. The terraces are normal to the **z** axis, the step is infinite in the **y** direction. Two point forces $\boldsymbol{\sigma}_a$ and $\boldsymbol{\sigma}_b$ are applied at the upper and lower edge of the step.

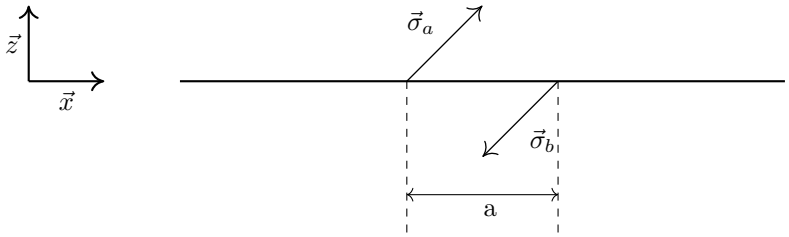



Figure 2.2: A reduced representation of the surface step. Two point forces $\boldsymbol{\sigma}_a$ and $\boldsymbol{\sigma}_b$ are applied to a planar surface.

The displacement field due to a line of dipolar forces is obtained by differentiating the Green tensor with respect to $x$ and integrating along the length of the step $y$ from $-\infty$ to $\infty$ (a detailed derivation can be found in [1]). The displacement field at the surface $z = 0$ is [1]:

$$u_x(x, y, 0) = \frac{2(1-\nu^2)}{\pi E} \frac{a\sigma'_{ax}}{x}, \quad u_y(x, y, 0) = 0, \quad u_z(x, y, 0) = \frac{2(1-\nu^2)}{\pi E} \frac{hs_{xx}}{x} \tag{2.12}$$

This field diverges at the point of location of the forces, but describes the asymptotic behavior a few atomic distances removed from the point of application of the forces.

At the surface the strain component perpendicular to the interface equals $\epsilon_{zz}(z = 0) = \partial u_z/\partial z|_{z=0} = 0$.

The general functional dependence of the displacements $u_z(x, y, 0)$ was reproduced in our results the surface strain component $\epsilon_{zz}$ was indeed negligible at the surface, see Section 4.2.

## 2.3 Defects and Plastic Deformation in Metallic Materials

Many of the properties of materials are sensitive to deviations from crystalline perfection and often specific characteristics are deliberately manipulated by the introduction of particular defects [49].

A crystalline defect is by definition any region where the microscopic arrangement of atoms differs from that of a perfect crystal [49].

In solid-state systems the centro-symmetry parameter, $C_S$, is used to determine whether the atom is part of a perfect lattice, a part of a dislocation or stacking fault, or perhaps

at a surface. This parameter is computed using the following formula [50]

$$C_{\mathrm{S}} = \sum_{i=1}^{N/2} |\mathbf{R}_i + \mathbf{R}_{i+N/2}|^2 \tag{2.13}$$

where the $N$ nearest neighbors of each atom are identified and $\mathbf{R}_i$ and $\mathbf{R}_{i+N/2}$ are vectors from the central atom to a pair of nearest neighbors. $N$ is an input parameter, and corresponds to the number of nearest neighbors in the underlying lattice of atoms ( for FCC lattices $N$ equals 12). There are $N(N-1)/2$ possible neighbor pairs that can contribute to this formula. The sum is computed for each possible pair, and the $N/2$ smallest are used. As such, $C_{\mathrm{S}}$ parameter is a measure of the local lattice disorder around a given atom and is especially useful in molecular dynamics simulations, where the neighbors of each atom are continually tracked for the purposes of calculating a trajectory and all atoms' positions are known at all times.

For an atom positioned at a lattice site, surrounded by atoms on a perfect lattice, the centro-symmetry parameter $C_{\mathrm{S}}$ will be 0. At temperatures above 0 K, it will be near 0 due to small thermal vibrations. If an atom is next to a vacancy, the symmetry is broken, and the parameter will be a larger positive value. An atom at a surface, missing multiple neighbors, will have a large positive parameter.

### 2.3.1 Point defects

Point defects can be vacancies or interstitials. All crystalline solids contain vacancies. The fraction of vacancies $N_v/N$ in metals just below the melting temperature is on the order of $10^{-4}$ [49]. In metals, which in general have very closely packed lattices, self-interstitials introduce large distortions in the surrounding crystal and are thus unlikely and exist in significantly lower concentrations than vacancies [49].

As our study focuses on systems at a relatively low temperature of 10 K that contain at most 800.000 atoms, the effect of point defects can be neglected.

### 2.3.2 Line defects

Line defects, such as stacking faults and dislocations, are essential in describing the mechanisms of plastic deformation. Dislocations play a crucial role in the process of slip. Dislocation densities in actual crystals depend on the preparation of the specimen, but range from $10^2$ to $10^{12}$ cm$^{-3}$ [49].

Along the dislocation, the crystal is substantially distorted. In consequence, the additional distortion required to move the dislocation sideways for one lattice constant requires relatively little additional applied stress [49]. The Burgers vector **b** is the most characteristic feature of a dislocation, defining the direction and the magnitude of slip [49].

In general, a dislocation is any closed curve in the crystal with the following properties [49]:

- Away from the closed curve the crystal is locally only negligibly different from the perfect crystal.
- In the neighborhood of the closed curve the atomic positions are substantially different from the original crystalline sites.
- A nonvanishing Burgers vector exists.

Let us first trace a closed curve in the perfect crystal passing through a succession of lattice sites, then traverse the same sequence of lattice sites on a curve that surrounds a

dislocation. The vector **b** by which the endpoint of the second path fails to coincide with the starting point is called the Burgers vector **b** of the dislocation [49].

Dislocation with a unit strength is a dislocation with a Burgers vector **b** equal to one lattice spacing [49]. The energy of the dislocation is proportional to the length of its Burgers vector [49]. In close-packed systems dislocations of strength less than unity are possible, since less than one lattice unit separates atoms in the closely packed directions.

A dislocation can switch from one plane to another if it contains the direction of the Burgers vector in a process called cross-slip [51].

When the strength of dislocation exceeds unity, the dislocation may dissociate into two dislocations, a leading and a trailing Shockley partial dislocation [49]. The area bounded by the two dissociate dislocations is a stacking fault. The equilibrium width of the partial dislocations depends on the stacking-fault energy. The wider the region between the partial dislocations, the lower the energy of the stacking fault. In the case of a high stacking-fault energy, cross-slip is more likely. Due to this correlation, it is important that the potentials used in molecular dynamics simulations of plasticity phenomena reproduce the stacking fault energies of the modeled materials.

Table 2.1: Typical values of stacking-fault energy ($mJ/m^2$) [52].

| Material | Silver | Gold | Copper | Nickel | Aluminum |
|---|---|---|---|---|---|
| SFE ($mJ/m^2$) | 16 | 32 | 41 | 125 | 150 |

When two leading Shockley partials combine, they form a new dislocation with a Burgers vector that is not in the slip plane. This is the Lomer–Cottrell dislocation also called the stair-rod dislocation. It is immobile in the slip plane, acting as a barrier against other dislocations in the plane forcing them to pile up behind it.

There also exists a more complex kind of slip, in which a family of coherent dislocations forms in successive crystal planes [49]. The result of the passage of a coherent family of dislocations through a crystal is a region in which the crystalline ordering is the mirror image of the original crystal. This process is called twinning, and the mirroring region is known as a deformation twin [49].

In crystals, not all directions are equally favorable for slip. Close-packed planes and directions are preferred in general. In addition, the angles the direction of strain forms with the slip plane normals and slip directions are important. Primary slip systems are defined as having the largest Schmid factors for the given strain direction, and are calculated as [49]

$$m = (\mathbf{s}_P \cdot \mathbf{n}_s)(\mathbf{s}_D \cdot \mathbf{n}_s), \tag{2.14}$$

where $\mathbf{s}_P$, $\mathbf{s}_D$ and $\mathbf{n}_s$ denote the slip plane normal, slip direction and strain direction.

# Chapter 3

# Simulation Methodology

## 3.1 Introduction to Molecular Dynamics Simulations

Molecular dynamics (MD) simulations are used for calculating the trajectories of a system of interacting particles by numerically solving the Newton's equations of motion, wherein the forces between the particles and potential energy are defined by interatomic potentials [47]. The trajectory of a single molecular dynamics simulation of a physical system may be used to determine macroscopic thermodynamic properties of the given system [47].

At the nanoscale, continuum theories reach their limits and the atomic scale of materials becomes important [53]. For instance, the long-range elastic fields of a dislocation are well described by the continuum elasticity theory, but the description diverges near the dislocation core and the discrete atomic nature has to be considered for the zone of singularity [53]. Analogously, the continuum description of a vicinal surface diverges at the steps. MD is one of the most used tools to investigate nanoscale behaviors of materials, especially for the problems which require the model sizes too big for quantum simulation to be feasible, but the atomic resolution is desired or required. Specifically, there have been many MD studies of dislocation motion, because MD is still the most flexible methodology available for the understanding of the underlying atomic-level mechanisms governing the complex plastic deformation behavior in materials [53]. MD simulations are well suited for the study of dislocation motion due to their size- and time-scales, and because they are relatively inexpensive compared to TEM experiments, in which dislocation motion can also be observed.

The MD simulations can be computationally expensive in two aspects: the number of atoms and the number of timesteps [47]. An adequate number of atoms in a simulation is required to avoid boundary condition artifacts and to adequately describe the system. The length scale for atomic coordinates is Angstroms [47]. To ensure that the vibrational motion of the atoms is accurately tracked, the timestep size is constrained to the femtosecond scale [47]. This means that many thousands of atoms are needed to fill even nanosized volumes and at least tens of thousands of timesteps are necessary to simulate even picoseconds of "real" time [47].

The time evolution of positions and velocities in a MD simulation is called a trajectory. Given the initial positions and velocities, we can calculate all future (or past) positions and velocities by integrating a set of coupled differential equations [47]. The Newton's equation of motion for a conservative physical system is given by [47]

$$M\ddot{\boldsymbol{x}}(t) = \boldsymbol{F}(\boldsymbol{x}(t)) = -\nabla U(\boldsymbol{x}(t)) \tag{3.1}$$

where $M$ is the mass matrix, typically diagonal with mass $m_k$ for every particle, $\boldsymbol{x}(t) = (\boldsymbol{x}_1(t), \ldots, \boldsymbol{x}_N(t))$ is the position vector of $N$ objects, $t$ is the time, $U$ is the scalar potential

function, and $\boldsymbol{F}$ is the negative gradient of the potential giving the forces on the particles. The potential energy function $U(\boldsymbol{x}(t))$ of the system is usually referred to simply as the "potential". For various choices of the potential function $U$, the same methodology can be used to describe the trajectories of diverse physical systems.

The task of the simulation software is to construct a sequence of points $\boldsymbol{x}_n$ that closely follow the points $\boldsymbol{x}(t_n)$ on the trajectory of the exact solution. Velocity Verlet is the standard algorithm for numerical integration in MD. Starting with an initial position $\boldsymbol{x}(0) = \boldsymbol{x}_0$ and an initial velocity $\boldsymbol{v}(0) = \dot{\boldsymbol{x}}(0) = \boldsymbol{v}_0$, at every time step the following equations are used to update positions, velocities and accelerations [54]:

$$\boldsymbol{v}_{n+1/2} = \boldsymbol{v}_n + \frac{1}{2}\Delta t \boldsymbol{a}_n \tag{3.2}$$

$$\boldsymbol{x}_{n+1} = \boldsymbol{x}_n + \Delta t \boldsymbol{v}_{n+1/2} \tag{3.3}$$

$$M\boldsymbol{a}_{n+1} = \boldsymbol{F}_{n+1} = -\nabla U(x_{n+1}) \tag{3.4}$$

$$\boldsymbol{v}_{n+1} = \boldsymbol{v}_{n+1/2} + \frac{1}{2}\Delta t \boldsymbol{a}_{n+1}. \tag{3.5}$$

The velocities are updated twice and the positions are updated using the intermediate velocity.

## 3.2 Materials

To describe the material we wish to simulate a potential function $U$ is needed. Ideally, in the cases of long–range forces, such as Coulombic interactions, each atom interacts with all others, which is computationally too costly for MD [47]. Instead, short–range force models are used extensively in MD [47]. In such models electronic screening effectively limits the range of influence of the interatomic forces being modeled or the long–range interactions are simply truncated to lessen the computational load [47].

Starting from a fully quantum description two main approximations are required, so we can then construct a classical potential [53]:

1. The first approximation is the Born-Oppenheimer approximation, stating that the electrons are so fast that they can be considered to react instantaneously to the motion of their nuclei. This approximation allows us to treat the electrons separately from their nuclei.

2. The second approximation is that the nuclei can be considered as point particles that follow classical Newtonian dynamics.

The potential functions are typically formulated as a sum over interactions between the particles of the system [55]. An example of a pair potential is the Lennard–Jones potential, used for calculating van der Waals forces or describing noble gases, in which the total potential energy can be calculated from the sum of energy contributions between pairs of atoms [55]:

$$U(r) = 4\varepsilon\left[\left(\frac{\sigma}{r}\right)^{12} - \left(\frac{\sigma}{r}\right)^{6}\right], \tag{3.6}$$

where $r$ is the interatomic distance and the $\varepsilon$ and $\sigma$ are free parameters defining the energy and the length scales. Such pairwise potentials are unable to adequately describe metals or semiconductors [56], thus, more complex potentials need to be considered. In many-body potentials, the potential energy includes the effects of three (or more) particles interacting with each other [57]:

$$U = \sum_i w_2(i) + \sum_{i,j} w_3(i,j) \tag{3.7}$$

where $w_2(i)$ and $w_3(i,j)$ are the pair and triplet terms.

Model analytical functions are chosen for the pair-wise, $w_2(i)$, and triplet, $w_3(i,j)$, terms, and appropriate parameters are found by fitting those model analytical functions to physical properties that describe a given system. Such an approach was adopted by Stillinger and Weber [57] to describe Si with a combination of exponential and trigonometric terms:

$$w_2(r) = \begin{cases} A(Br^{-p} - r^{-q})\exp[(r-a)^{-1}] & \text{if } r > a \\ 0 & \text{if } r \leq a \end{cases} \tag{3.8}$$

$$w_3(\boldsymbol{r}_i, \boldsymbol{r}_j, \boldsymbol{r}_k) = h(r_{ij}, r_{ik}, \theta_{jik}) + h(r_{ji}, r_{jk}, \theta_{ijk}) + h(r_{ki}, r_{kj}, \theta_{ikj}), \tag{3.9}$$

where $\theta_{jik}$ is the angle between $\boldsymbol{r}_j$ and $\boldsymbol{r}_k$ subtended at vertex $i$, etc. The same cutoff $a$ applies to $h$ functions, and within the specified cutoff functions $h$ take the following form:

$$h(r_{ij}, r_{ik}, \theta_{jik}) = \lambda \exp[\gamma(r_{ij} - a)^{-1} + \gamma(r_{ik} - a)^{-1}](\cos\theta_{jik} + \tfrac{1}{3})^2, \tag{3.10}$$

and otherwise vanish identically. The trigonometric part was chosen specifically to favor pairs of bonds emanating from the vertex $i$ with the desired tetrahedral geometry.

This potential has seven free parameters, which were chosen so that the diamond structure was the most stable one at low pressure, and that melting point and liquid structure were in reasonable agreement with experiment [57]. The set of free parameters provided by Stillinger and Weber [57] was quite successful in describing Si, it did however considerably underestimate the cohesive energy of the crystal.

A similar approach was taken by Ercolessi *et al.* [56] to describe gold by what they called the glue model, geared toward noble and near-noble metals with very broad filled d bands that do not form directional bonds. They extended the potential by a many-body term, taking into account that the energy of an atom depends nonlinearly on its coordination. The total potential energy of an atom is then given by

$$U = \frac{1}{2}\sum_{i \neq j} \phi(r_{ij}) + \sum_{i=1}^{N} U(n_i), \tag{3.11}$$

where the $U(n_i)$ term is called "the glue" and $n_i$ is the generalized coordination of atom $i$ given by

$$n_i = \sum_{j=1}^{N-1} \rho(r_{ij}) \tag{3.12}$$

where $\rho(r_{ij})$ is a monotonically decreasing function of distance, so that nearby atoms contribute more to $n_i$ than more remote atoms. Sets of polynomials were chosen to describe $\phi$, $\rho$, and $U(n_i)$. The accompanying parameters were determined by fitting to physical properties of gold, and the resulting potential successfully predicts the occurrence of surface reconstruction on all the low-index surfaces of Au.

Current state of the art potentials for close-packed metals are based on the embedded atom method (EAM) [58], [59], where the total energy $E_i$ of an atom $i$ is given by

$$E_i = \sum_{i \neq j} F(\rho(r_{ij})) + \frac{1}{2}\sum_{i \neq j} \phi(r_{ij}) \tag{3.13}$$

where $F$ is the embedding energy which is a function of the atomic electron density $\rho$, and $\phi$ is an electrostatic, pair-wise interaction. In this view, the energy of an atom is dependent on the local electron density provided by the other atoms of the system. The total energy of an atom is equated to the cohesive energy of a metal and the embedding energy term

is derived from the density-functional theory expression for the cohesive energy of a solid by assuming that (i) the kinetic, exchange and correlation energy functional depends only on the local electron density and its lower derivatives, and (ii) the local electron density of the solid can be described as a linear superposition of the densities of the individual atoms [58]. Following these assumptions, both, $\rho$ and $\phi$, are functions of only the interatomic distances, $r_{ij}$, of all neighbors $j$ of atom $i$ within the cutoff distance [59].

In this study the embedded-atom method (EAM) potentials developed by Mishin *et al.* for Cu [46] and by Mishin *et al.* for Ni [45] were used. The semi-empirical potential function for Cu was based on exponentials [46] and for Ni was based on cubic splines through a set of fixed points [45]. The cutoff distances for the potentials used in this study were 0.5507 nm for Cu [46] and 0.5804 nm for Ni [45]. The lattice constants for these potentials at 0 K are $a_0^{Cu} = 0.3615nm$ and $a_0^{Ni} = 0.3520nm$.

## 3.3 Software

In this study the LAMMPS Molecular Dynamics Simulator [47], [59] software was used for the MD simulations. Sample LAMMPS scripts for the main parts of the simulations are available in Appendices A, B and C.

OVITO [60] was used in post-processing, to visualize the results of the simulations, and analyze displacement fields, elastic fields and dislocations. The Dislocation Extraction Algorithm (DXA) [61] was used to detect and visualize dislocations. The DXA analyzes the original atomistic representation of a crystal and produces a line-based representation of the dislocation network. It determines the Burgers vector of each dislocation segment and identifies dislocation junctions, by first identifying the parts of the crystal that can be mapped to a perfect crystal and those that cannot, then constructing a surface that separates the two, also called the interface mesh. By sequentially constructing Burgers circuits from the atoms that fall onto the interface mesh, Burgers vectors of dislocation segments are calculated.

Gnuplot [62] was used for plotting.

## 3.4 Substrates' Configuration

The simulations were performed on an array of substrates, divided throughout this thesis into three sets of low-index surfaces with their vicinals for convenience: (1 1 19) vicinal to (0 0 1), (19 19 1) vicinal to (1 1 0), and (9 9 11) and (10 10 8) both vicinal to (1 1 1).

Details on substrate orientation in the simulation box and primary slip systems are given in Table 3.1 and graphically represented in Fig. 3.1, Fig. 3.2 and Fig. 3.3.

The boundaries of the simulation boxes were periodic in the $\boldsymbol{x}$ and $\boldsymbol{y}$ directions and fixed in the $\boldsymbol{z}$ direction. For vicinal surfaces, the simulation box was subject to requirements for periodicity of the terraces in the $\boldsymbol{y}$ direction. The number of steps and terraces included was 8. The width of the simulation boxes in the $\boldsymbol{x}$ direction was $L_x = 30|\boldsymbol{x}|$, where $|\boldsymbol{x}|$ is the length of the axis vector in each case, as given in Table 3.1.

In the $\boldsymbol{z}$ direction the simulated films were bound by a free surface at the top and by a layer of fixed atoms at the bottom to prevent the loss of atoms at the border of the simulation box and to simulate defect-free bulk. The thickness of this frozen layer was 1.2 nm. These atoms were fixed at the positions they had when equilibrated to 10 K and were remapped at every deformation of the simulation box. All the forces acting on these atoms were otherwise reset to zero. The height of the slabs measured orthogonal to the terraces was 35 unit cells along the basis vector aligned with the terrace normal of each case.

Table 3.1: Axis vectors and primary slip systems with Schmid factors for each simulated substrate. The $\boldsymbol{y}$ axis is also the strain direction and the $\boldsymbol{z}$ axis the surface normal for each case. Primary slip systems listed are the ones that have the largest Schmidt factors for the given strain direction. Schmid factors were calculated using Eq. 2.14. For the (001), (1 1 19) and (110) surfaces two slip directions are active in each slip plane.

| Axis vectors | | | Primary slip systems | |
|---|---|---|---|---|
| $\boldsymbol{x}$ | $\boldsymbol{y}$ | $\boldsymbol{z}$ | Slip systems | Schmid factor |
| (1 $\bar{1}$ 0) | (110) | (001) | $\{111\}\langle 0\bar{1}1\rangle$,$\langle\bar{1}01\rangle$<br>$\{11\bar{1}\}\langle 011\rangle$,$\langle 101\rangle$ | 0.408 |
| (1 $\bar{1}$ 0) | (19 19 $\bar{2}$) | (1 1 19) | $\{111\}\langle 0\bar{1}1\rangle$,$\langle\bar{1}01\rangle$ | 0.425 |
| (2 $\bar{2}$ 1) | (00$\bar{1}$) | (110) | $\{111\}\langle 0\bar{1}1\rangle$,$\langle\bar{1}01\rangle$<br>$\{\bar{1}11\}\langle 0\bar{1}1\rangle$,$\langle 101\rangle$<br>$\{1\bar{1}1\}\langle 011\rangle$,$\langle\bar{1}01\rangle$<br>$\{11\bar{1}\}\langle 011\rangle$,$\langle 101\rangle$ | 0.408 |
| (1 $\bar{1}$ 0) | (1 1 -38) | (19 19 1) | $\{\bar{1}11\}\langle 0\bar{1}1\rangle$<br>$\{1\bar{1}1\}\langle\bar{1}01\rangle$ | 0.418 |
| (1 $\bar{1}$ 0) | (11$\bar{2}$) | (111) | $\{\bar{1}11\}\langle 0\bar{1}1\rangle$<br>$\{1\bar{1}1\}\langle\bar{1}01\rangle$ | 0.408 |
| (1 $\bar{1}$ 0) | (11 11 -18) | (9 9 11) | $\{\bar{1}11\}\langle 0\bar{1}1\rangle$<br>$\{1\bar{1}1\}\langle\bar{1}01\rangle$ | 0.377 |
| (1 $\bar{1}$ 0) | (8 8 -20) | (10 10 8) | $\{\bar{1}11\}\langle 0\bar{1}1\rangle$<br>$\{1\bar{1}1\}\langle\bar{1}01\rangle$ | 0.433 |

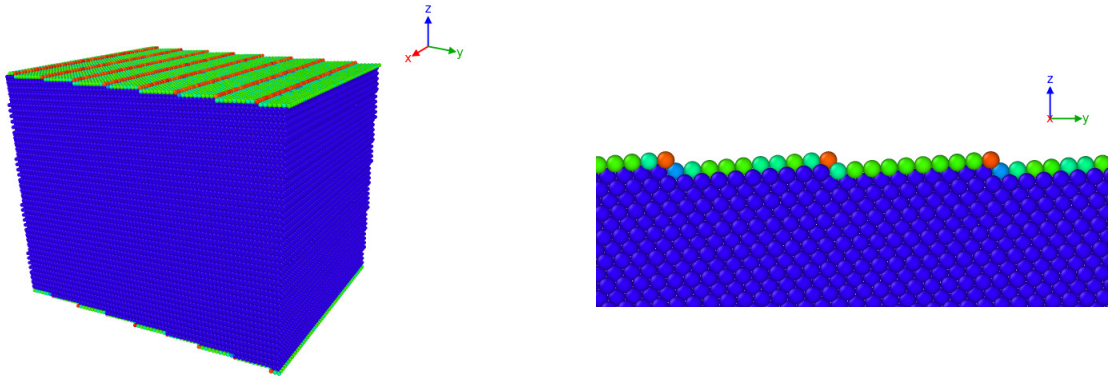
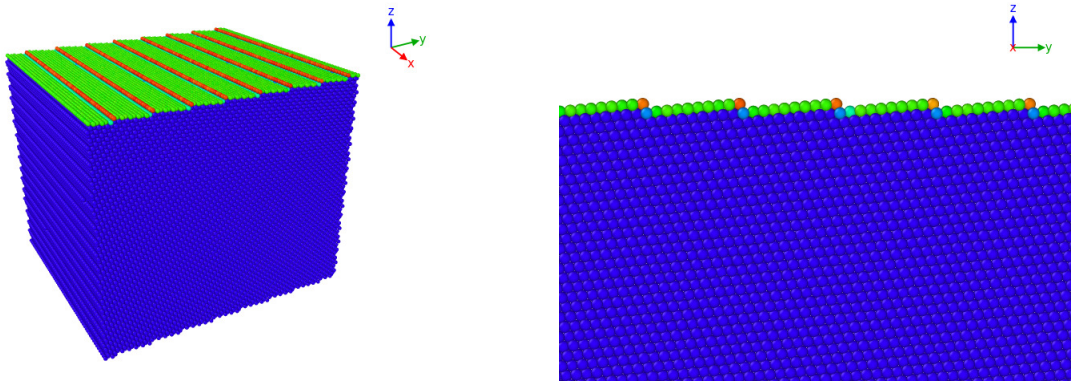
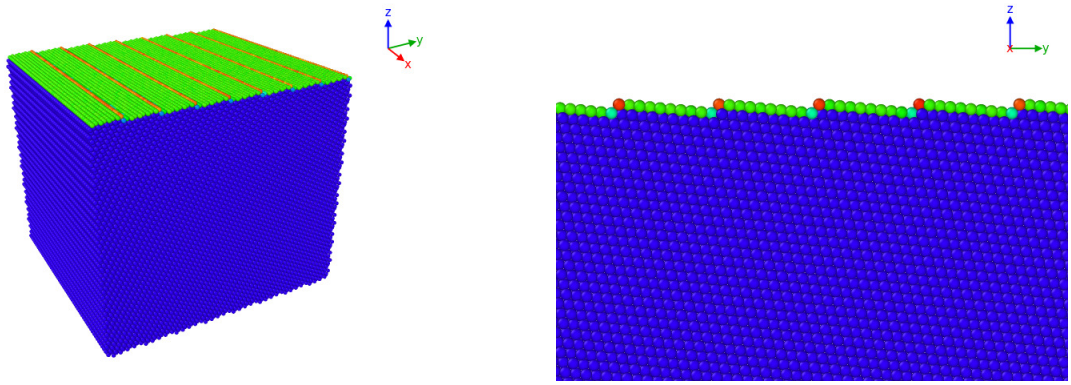



Figure 3.1: Graphic representation of the substrate orientation within the simulation box (left) and a side view of steps (right) for the vicinal surface with the normal $\mathbf{z}$ = (1 1 19).



(a) **z** = (9 9 11)



(b) **z** = (10 10 8)

Figure 3.2: Graphic representation of the substrate orientation within the simulation box (left) and a side view of steps (right) for the surfaces vicinal to (111).

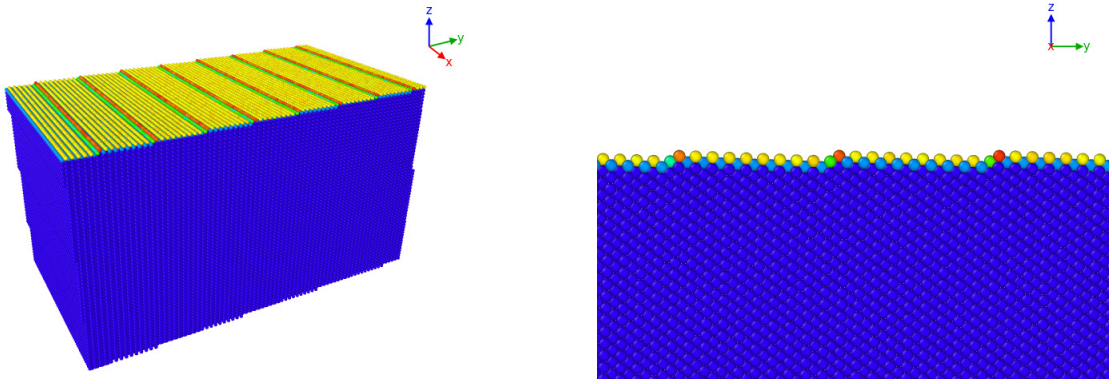
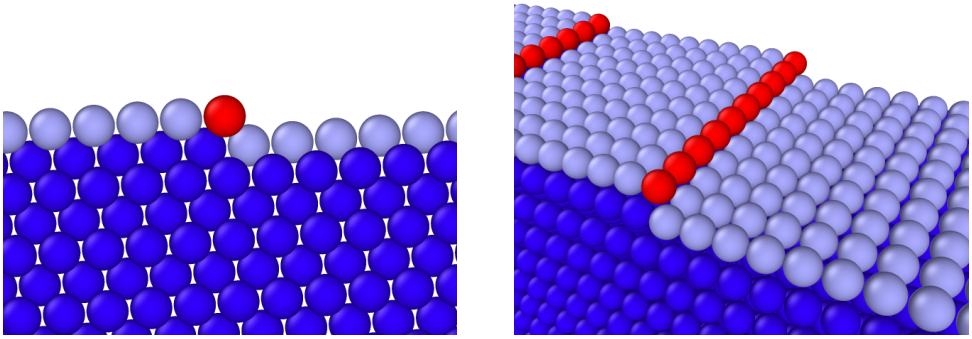
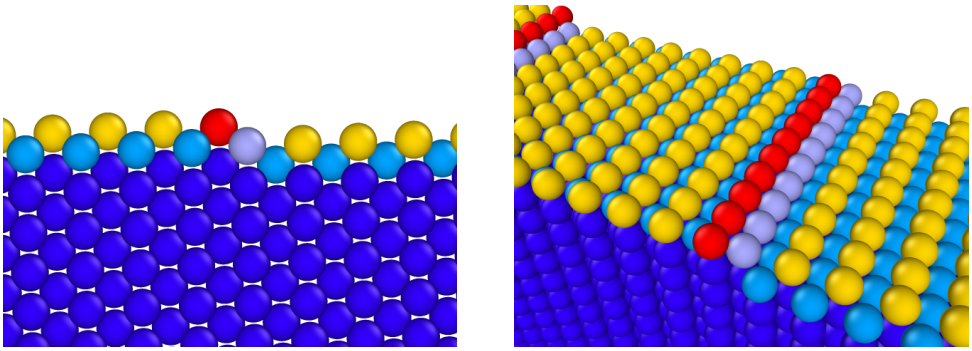


Figure 3.3: Graphic representation of the substrate orientation within the simulation box (left) and a side view of steps (right) for the vicinal surface with the normal **z** = (19 19 1).

In addition to having different terrace orientations, steps also have distinct microfacets. Vicinals to (001) and (110), shown in Fig. 3.4, both have (111) oriented step microfacets. The (9 9 11) surface has (001) oriented microfacets, also called A-step, shown in Fig 3.5a. The (10 10 8) surface has ($\overline{1}\overline{1}1$) oriented microfacets, also called B-step, shown in Fig 3.5b.



(a) $\mathbf{z}$ = (1 1 19)



(b) $\mathbf{z}$ = (19 19 1)

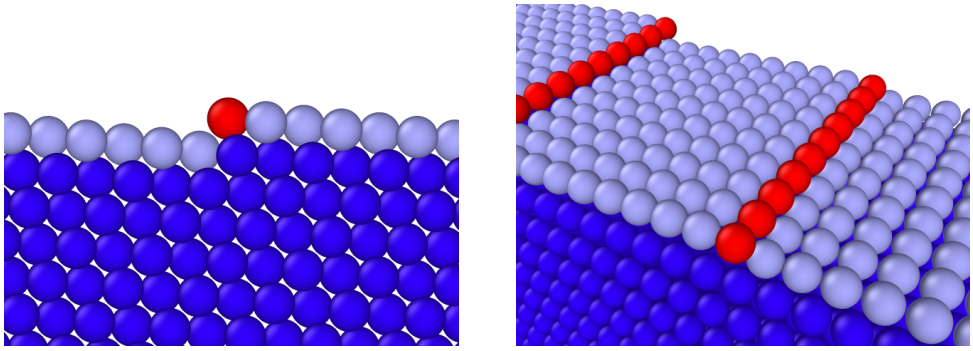
Figure 3.4: Atomically resolved representation of the step microfacets for the (1 1 19) and (19 19 1) vicinal surfaces. The (1 1 19) surface is shown in (a) and the (19 19 1) surface is shown in (b). Both surfaces have (111) oriented step microfacets. A side view is shown on the left, and a projection in shown on the right. Atoms are colored according to the centrosymmetry parameter $C_S$. Step edge atoms are in red and fully coordinated atoms in dark blue. The (110) surface is the least dense of all the low-index surfaces, thus, its terrace atoms are in yellow.

## 3.5 Minimization

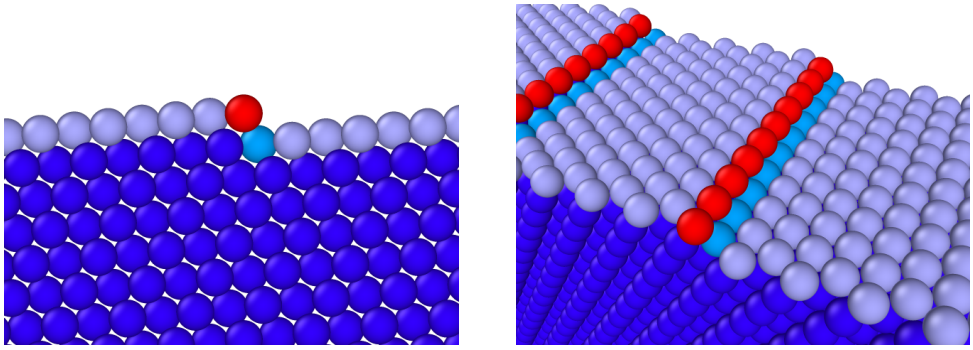
Classical minimization procedure called the steepest descent algorithm (*sd*) [59] was used to find minimal energy states of the low-index surfaces at 0 K. At each iteration, the search direction is set to the largest negative gradient of energy [59].

To find minimal energy states of the vicinal surfaces, damped dynamics [48] were used to find minimal energy states of the vicinal surfaces, resulting in the displacement fields. This method introduces slight thermal vibrations to the atoms in the system. In the LAMMPS code the method is implemented in the *quickmin* style of the minimization [59].

A sample minimization script is provided in App. A.



(a) $\mathbf{z} = (9\ 9\ 11)$



(b) $\mathbf{z} = (10\ 10\ 8)$

Figure 3.5: Atomically resolved representation of the step microfacets for the (9 9 11) and (10 10 8) vicinal surfaces. The (9 9 11) surface has (001) oriented microfacets, also called the A-step (a). The (10 10 8) surface has $(\overline{1}\overline{1}1)$ oriented microfacets, also called the B-step (b). A side view is shown on the left, and a projection in shown on the right. Atoms are colored according to the centrosymmetry parameter $C_S$. Step edge atoms are in red and fully coordinated atoms in dark blue.

## 3.6 Equilibration

All substrates were equilibrated to 10 K. Equilibration is required before simulations of deformation could be performed. A sample equilibration script is provided in App. B.

NVT ensemble (constant number of particles, volume and temperature) was used to equilibrate the systems to the desired temperature of 10 K [59].

Timestep was set to 1 fs. Equilibration was run for 50 ps.

## 3.7 Simulations of Deformation

To simulate tensile and compressive strains, the simulation box was deformed using *fix deform* in the $y$ direction and a NPT barostat was used to relax the simulation box in the $x$ direction accordingly to keep pressure in that direction to zero [59]. In the $z$ direction the substrate was left free. A sample LAMMPS script is provided in App. C.

The *trate* style in the *fix deform* family changes a dimension of the box at a "constant true strain rate" [59]. The box length $L$ changes non-linearly with time as [59]

$$L(t) = L_0 \exp(R \cdot \mathrm{d}t) \tag{3.14}$$

where d$t$ is the elapsed time and $R$ the strain rate, which was set to $\pm$ 2.5 % ps$^{-1}$ in our simulations.

# Chapter 4

# Elastic Fields of Vicinal Surfaces

In this chapter, results of the atomic relaxations of surfaces at 0 K are given. The low-index surfaces relax by a change in interlayer distances of the few topmost atomic layers. The vicinal surfaces relax by a complex displacement field, stretching several atomic layers into the bulk. The displacement of the near-surface atoms from their ideal bulk positions in turn leads to a local elastic field.

## 4.1 Relaxation and Elastic Strain of Low-Index Surfaces

The results of the atomic relaxation calculations for the low-index surfaces are given in Table 4.1 as interlayer distances for the topmost layers and for bulk for comparison, as well as the displacement of the surface layer. The interlayer distance between the first and the second layers, $l_{1-2}$, is shorter than the bulk value, $l_{bulk}$, in all the cases. The interlayer distance between the fourth and fifth layers of atoms $l_{4-5}$ already matches the bulk value $l_{bulk}$ for the (001) and (111) surfaces.

The displacement of the surface layer, $d_{surf}$, equals the surface strain, $\epsilon_{zz}^{surf}$.

Table 4.1: Results of the atomic relaxation of the low-index surfaces of copper and nickel. Interlayer distances are given in nm for the topmost layers, $l_{i-j}$, and in the bulk, $l_{bulk}$. The displacement of the surface layer, $d_{surf}$, is also given in nm.

| | | Interlayer distances (nm) | | | | | Displacement (nm) |
|---|---|---|---|---|---|---|---|
| Element | Surface | $l_{1-2}$ | $l_{2-3}$ | $l_{3-4}$ | $l_{4-5}$ | $l_{bulk}$ | $d_{surf}$ |
| Cu | (001) | 0.1777 | 0.1797 | 0.1807 | 0.1808 | 0.1807 | -0.040 |
| | (110) | 0.1217 | 0.1278 | 0.1267 | 0.1282 | 0.1278 | -0.068 |
| | (111) | 0.2053 | 0.2084 | 0.2087 | 0.2088 | 0.2087 | -0.036 |
| Ni | (001) | 0.1741 | 0.1739 | 0.1760 | 0.1760 | 0.1760 | -0.040 |
| | (110) | 0.1223 | 0.1231 | 0.1238 | 0.1247 | 0.1245 | -0.040 |
| | (111) | 0.2007 | 0.2029 | 0.2033 | 0.2032 | 0.2032 | -0.028 |

The relaxation of the interlayer distances is temperature dependent [4]. Nevertheless, a comparison of relaxation trends in our study at 0 K with experimental results obtained at room temperature is possible. The data provided by LEED experiments indicates for Cu [63], [64] and for Ni [65], [66], that the (001) and (111) surfaces contract, and the amplitude of the contraction decreases with each layer, while the relaxation of the (110) surfaces is oscillatory, the first and third interlayer distances are contracted and the second interlayer

distance is dilated with regard to the bulk value. The contraction of the (001) and (111) surfaces is reproduced in our study. The oscillatory nature of the relaxation of the (110) surfaces is present but not as pronounced in our simulations as in the LEED data, as was expected due to the temperature discrepancy.

## 4.2 Relaxation of Vicinal Surfaces

The results for relaxation of the vicinal surfaces are given as displacement fields. Additionally, the displacements in the $z$ direction are compared with the displacements of the topmost layers of the low-index surfaces.

Elastic strain resulting from the displacement fields is also shown.

A schematic representation of the surface atoms and the numbering and notation used in the description of the displacements of the topmost atoms is shown in Fig. 4.1. The number 1 is the step edge atom, the number 10 is the terrace corner atom. Atoms numbered 2 through 9 are terrace atoms.

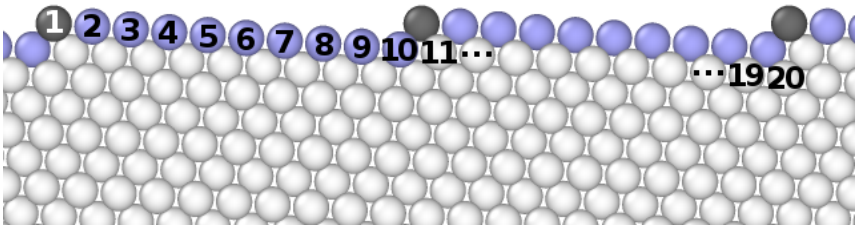



Figure 4.1: A schematic representation of the surface atoms and the numbering used in the description of the displacements of the topmost atoms. Although (1 1 19) surface is used in the schematic, this numbering applies to all vicinal surfaces studied. Number 1 is the step edge atom, number 10 is the terrace corner atom. Atoms numbered 2 – 9 are terrace atoms.

### 4.2.1 Displacement fields

Step edge (SE) atoms are displaced the most, effectively reducing the step height. A comparison of the magnitudes of the displacements of the SE atoms is given in Table 4.2. The magnitudes of displacements of the SE atoms are given in nm, $d_{SE}$, as a fraction of the lattice constant, $d_{SE}/a_0$, and as a fraction of the interlayer distance for the corresponding low-index surface, $d_{SE}/d_{1-2}$. Displacements are greater in Cu in absolute value and as compared to the lattice constant. The third row, $d_{SE}/d_{1-2}$, gives an estimate of the step height reduction. The step height reduction is in the range of 5 – 9 % in Cu and 3 – 7 % in Ni. Lattice constants are $a_0^{Cu} = 0.3615$ nm and $a_0^{Ni} = 0.3520$ nm. The values of $d_{1-2}$ are given in Table 4.1 for each low-index surface.

The displacement fields are graphically represented in Figures 4.2, 4.3, 4.4, and 4.5. The arrows show the direction of the displacements and are proportional to the magnitude of the displacements.

In the case of the (1 1 19) surfaces, see Fig. 4.2, the displacements in copper form a vortex underneath the terrace and extend up to 10 layers into the bulk, while the displacements in nickel are confined to the 5 topmost layers with no discernible vortex.

In the cases of the (111) vicinals, (9 9 11) in Fig. 4.3 and (10 10 8) in Fig. 4.4, the displacements form vortices underneath the steps in copper and in nickel.

Table 4.2: A comparison of the magnitudes of displacements of the step edge (SE) atoms given in nm, $d_{SE}$, as a fraction of the lattice constant, $d_{SE}/a_0$, and as a fraction of the interlayer distance for the corresponding low-index surface, $d_{SE}/d_{1-2}$. Displacements are greater in Cu in absolute value and as compared to the lattice constant. The third row, $d_{SE}/d_{1-2}$, gives an estimate of the step height reduction. The step height reduction is in the range of 5 – 9 % in Cu and 3 – 7 % in Ni. Lattice constants are $a_0^{Cu} = 0.3615$ nm and $a_0^{Ni} = 0.3520$ nm. The values of $d_{1-2}$ are given in Table 4.1 for each low-index surface.

| Element | | (1 1 19) | (9 9 11) | (10 10 8) | (19 19 1) |
|---|---|---|---|---|---|
| Cu | $d_{SE}$ (nm) | 0.0128 | 0.0117 | 0.0114 | 0.0109 |
| | $d_{SE}/a_0^{Cu}$ | 0.0354 | 0.0324 | 0.0315 | 0.0302 |
| | $d_{SE}/d_{1-2}$ | 0.0720 | 0.0570 | 0.0555 | 0.0896 |
| Ni | $d_{SE}$ (nm) | 0.0077 | 0.0065 | 0.0081 | 0.0081 |
| | $d_{SE}/a_0^{Ni}$ | 0.0219 | 0.0185 | 0.0230 | 0.0230 |
| | $d_{SE}/d_{1-2}$ | 0.0442 | 0.0324 | 0.0404 | 0.0662 |

In the cases of the (19 19 1) surfaces, see Fig. 4.5, the vortices also form underneath the steps.

Displacements in the $z$ direction of Cu and Ni vicinal surfaces at 0 K, compared with the displacements of the top two layers of low-index surfaces are shown in Fig. 4.6 for the (1 1 19) surfaces, Fig. 4.7 for the (111) surface vicinals and Fig. 4.8 for the (19 19 1) surfaces.

How the atoms are counted is shown in Fig. 4.1. Number 1 is the step edge atom, numbers 2 – 9 are terrace atoms, number 10 is the terrace corner atom, numbers 11 – 20 denote atoms in the second row underneath the terrace.

Dots denote the displacements of atoms of vicinal surfaces, and lines the displacements of the two topmost layers of low-index surfaces corresponding to each vicinal surface: (001) for the (1 1 19) vicinal, see Fig. 4.6, (111) for the (9 9 11) and (10 10 8) vicinals (shown in one figure, see Fig. 4.7) and (011) for the (19 19 1) vicinal, see Fig. 4.8. The pattern of the displacements is similar in the two materials, with the amplitude of the displacements being larger for Cu than for Ni.

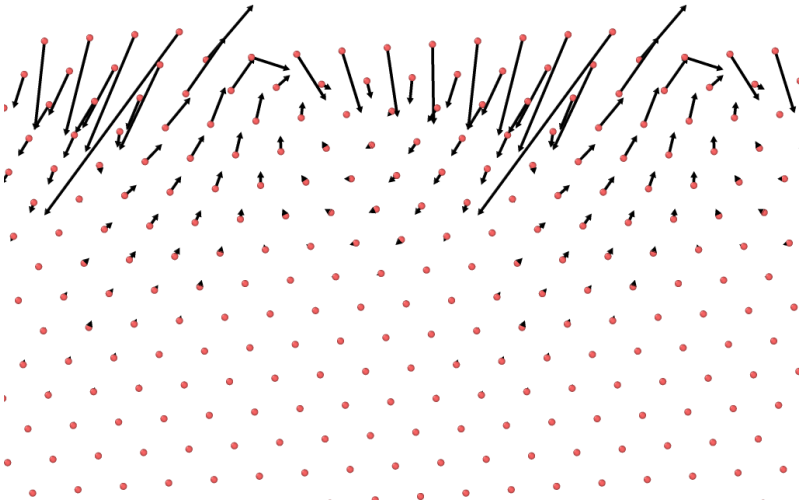
The patterns are distinctive for each surface orientation. For the (1 1 19) surfaces, both segments are monotonously rising as is predicted by the elasticity theory.

For the (9 9 11) surfaces, the second segment has a peak at atom 19 in copper and at atom 18 in nickel.

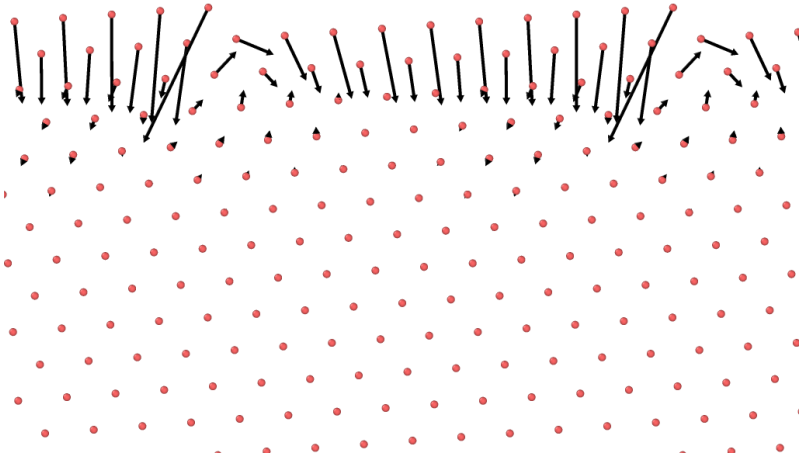
For the (10 10 8) surfaces, the segments have peaks at atoms 9 and 18 and the magnitude of the displacements of the atoms after the peak in each segment falls bellow the corresponding line denoting the amplitude of the contraction of the topmost layers of the (111) surfaces.

The patterns of the amplitudes of the displacements in the **z** direction are distinctive for each surface orientation. The magnitude of the displacements in the **z** direction of the mid-terrace atoms corresponds to the amplitude of the contraction of the interlayer distances for the low-index surfaces. The terraces thus relax by a contraction of the interlayer distances comparable to the corresponding low-index surface, while the steps introduce a distribution of the displacements around this mean value [4].

Elasticity theory describes the displacements of the topmost terrace atoms as monotonously rising with respect to their position along the terrace, which is accurate for all the



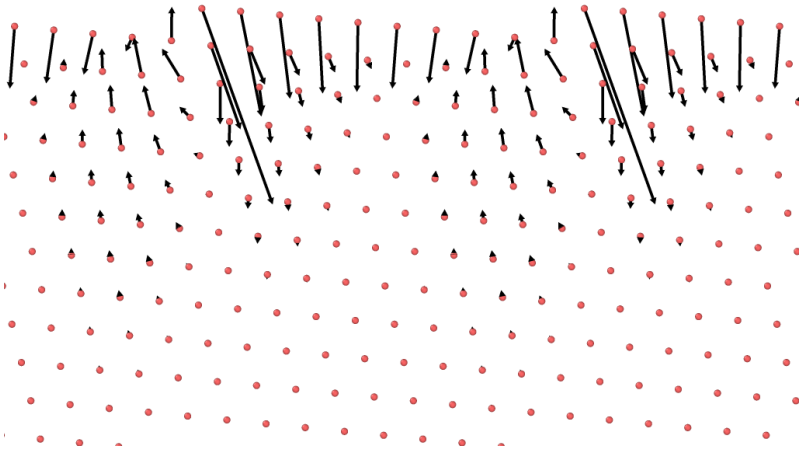
(a) Cu(1 1 19)



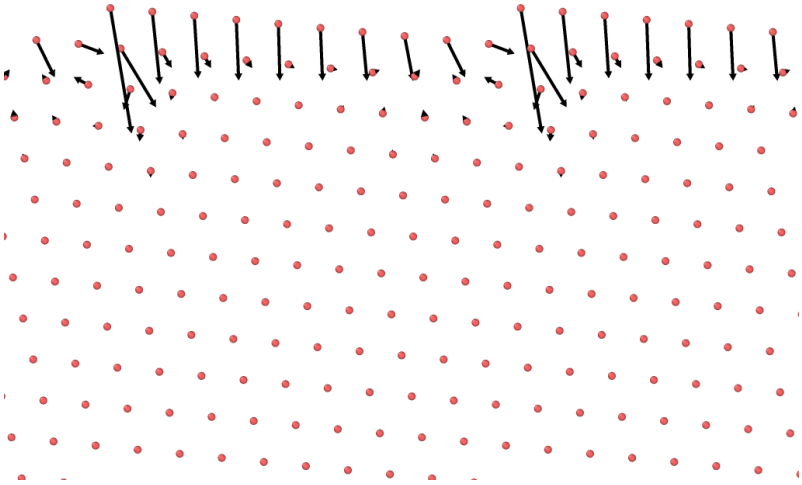
(b) Ni(1 1 19)

Figure 4.2: Displacement fields of Cu and Ni (1 1 19) vicinal surfaces. Dots denote atoms, and vectors the displacement from bulk position scaled by 100 for clarity. The displacements in copper form a vortex underneath the terrace and extend up to 10 layers into the bulk. The displacements in nickel are confined to the 5 topmost layers with no discernible vortex.

cases, except the (10 10 8) vicinals in which the 10-th atoms are displaced in the opposite direction than is expected from theory.



(a) Cu(9 9 11)

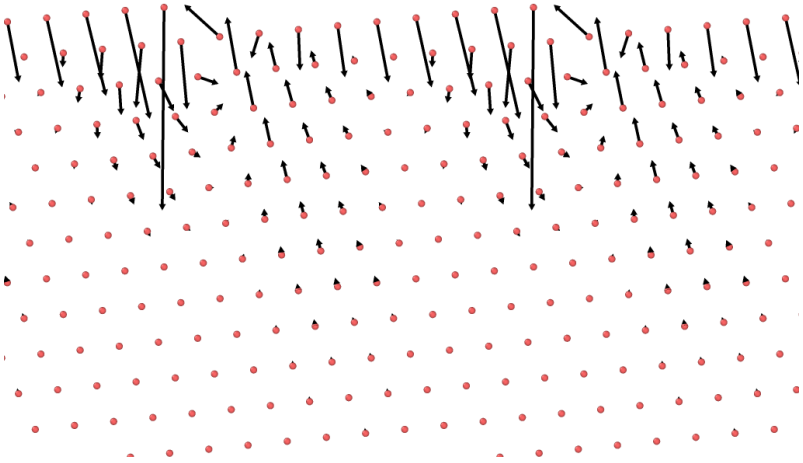


(b) Ni(9 9 11)

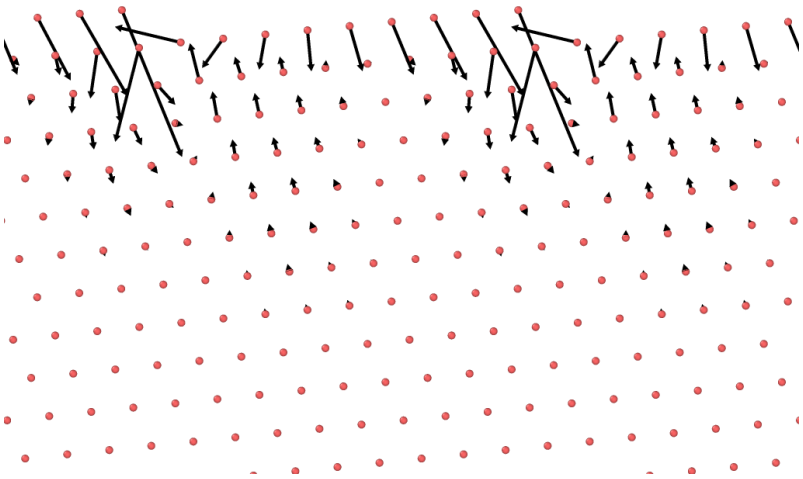
Figure 4.3: Displacement fields of Cu and Ni (9 9 11) vicinal surfaces. Dots denote atoms, and vectors the displacement from bulk position scaled by 100 for clarity. The displacement field in nickel is shallow compared to copper.

### 4.2.2 Elastic strain

Elastic strain fields of two components of the elastic tensor, $\epsilon_{zz}$ and $\epsilon_{zy}$, resulting from the displacement fields are shown in Fig. 4.9 through 4.12 and in Fig. 4.13 through 4.16, respectively. Atoms are colored according to the given component of the elastic tensor: green color denotes zero strain, compression is marked by blue and tension by red tones (color legends are included in the figures). It is important to note, that the amplitude of the strains in the case of the $\epsilon_{zy}$ is much smaller than in the case of the $\epsilon_{zz}$ and the scales



(a) Cu(10 10 8)



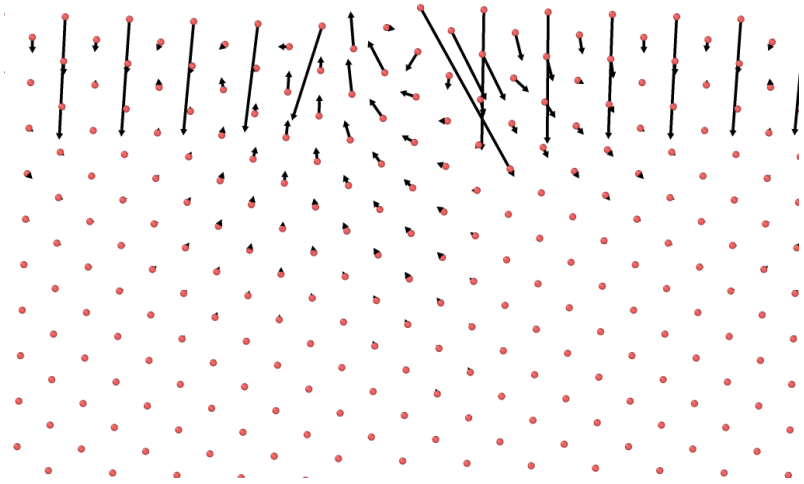
(b) Ni(10 10 8)

Figure 4.4: Displacement fields of Cu and Ni (10 10 8) vicinal surfaces. Dots denote atoms, and vectors the displacement from bulk position scaled by 100 for clarity. The displacements form vortices underneath the steps.

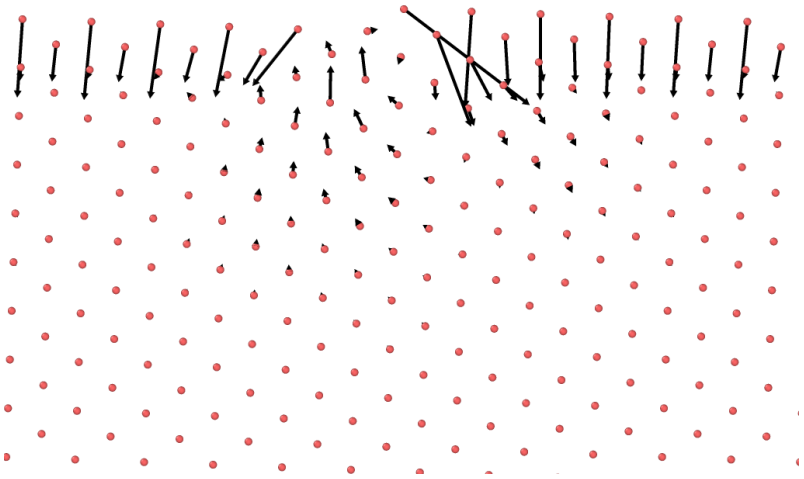
used in figures are different.

The prominent feature of the strain fields for the $\epsilon_{zz}$ component of the elastic tensor is for all the cases the compressive strain in the second topmost layer (see Fig. 4.9 through 4.12 ).

What was difficult to discern from the displacement fields of the (9 9 11) and (10 10 8) surfaces, see Fig. 4.3 and 4.4, is that compressive strain is introduced underneath the terraces in the (9 9 11) surfaces, see Fig. 4.14, while tensile strain is introduced in the case



(a) Cu(19 19 1)

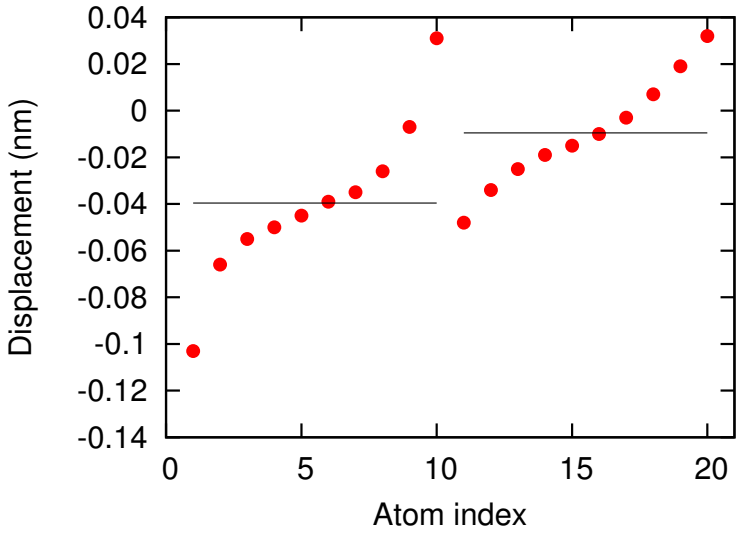


(b) Ni(19 19 1)

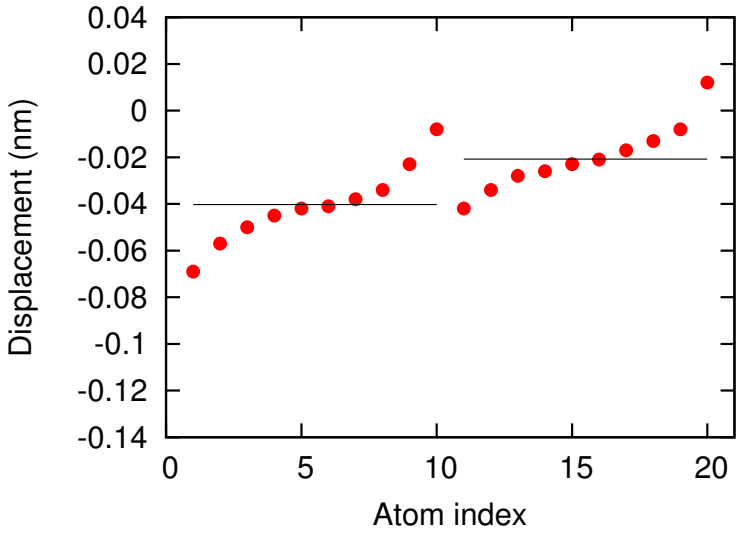
Figure 4.5: Displacement fields of Cu and Ni (19 19 1) vicinal surfaces. Dots denote atoms, and vectors the displacement from bulk position scaled by 100 for clarity. The displacements form vortices underneath the steps.

of the (10 10 8) surfaces, see Fig. 4.15.

The contours of the elastic fields are specific for each surface orientation. In comparison of copper and nickel, we find that $\epsilon_{zz}$ fields are very similar, while $\epsilon_{zy}$ fields are shallower in nickel, reaching fewer layers into the bulk, and the amplitude of the strain is smaller, especially in the cases of the (1 1 19) and (9 9 11) vicinals, see Fig. 4.13 and Fig. 4.14.

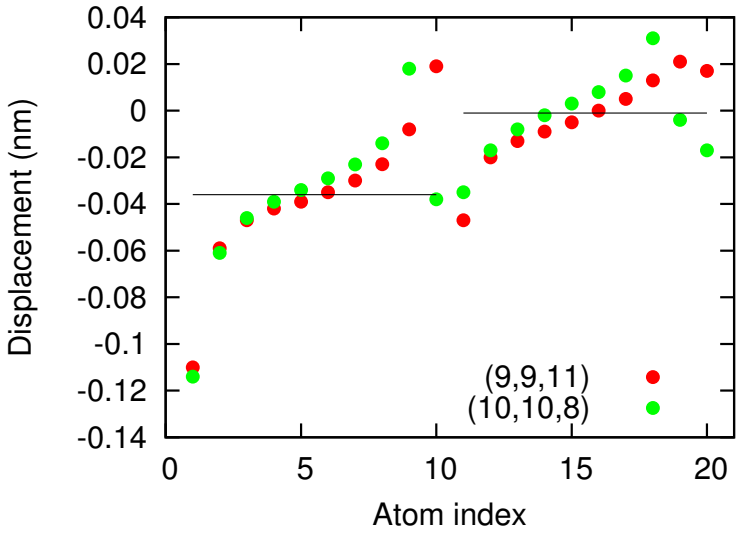



(a) Cu(1 1 19)

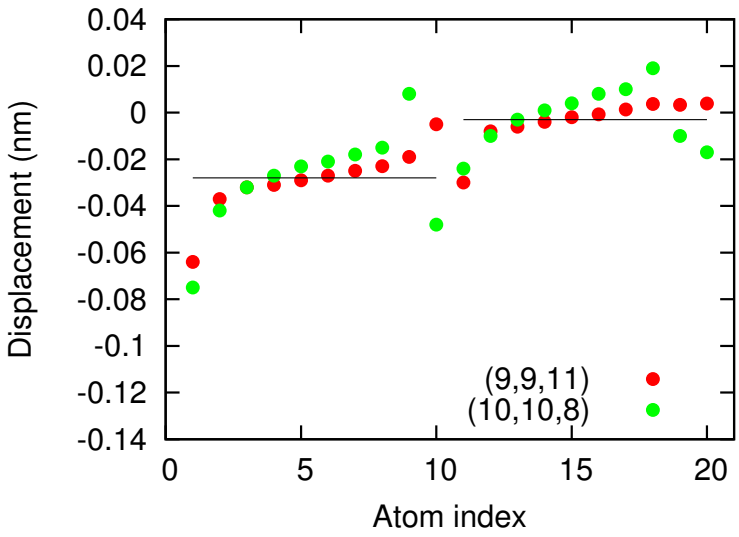



(b) Ni(1 1 19)

Figure 4.6: Displacements in the $z$ direction of Cu (a) and Ni (b) (1 1 19) vicinal surfaces at 0 K, compared with the displacements of the top two layers of the (001) surface. Dots denote the displacements of atoms of vicinal surfaces, and lines the displacements of the two topmost layers of low-index surfaces. The pattern of the displacements is similar in the two materials, with the amplitude of the displacements being larger for Cu than for Ni. The segments are monotonously rising.

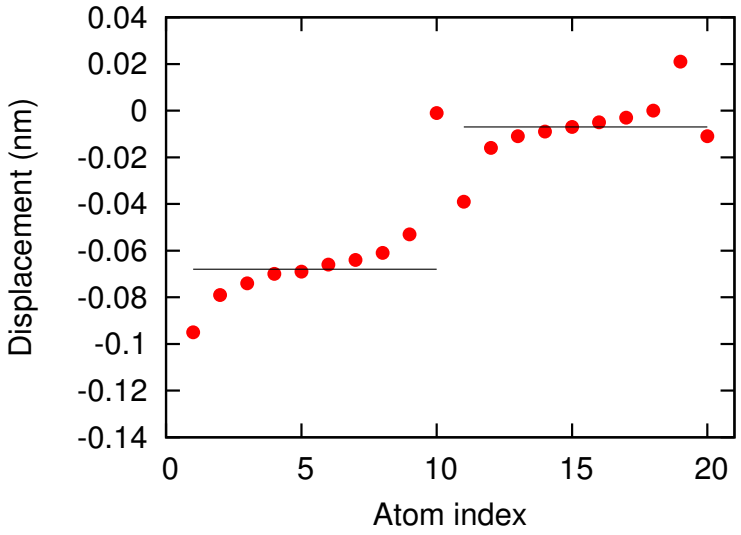



(a) Cu(9 9 11) & Cu(10 10 8)

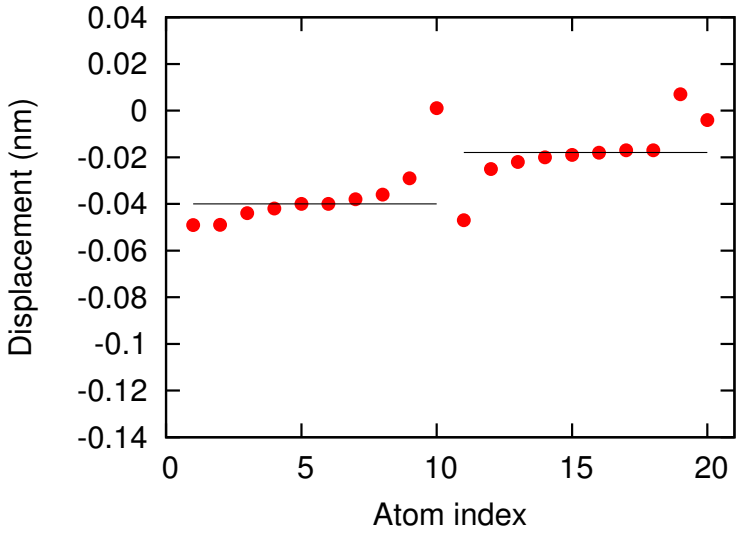



(b) Ni(9 9 11) & Ni(10 10 8)

Figure 4.7: Displacements in the $z$ direction of (a) Cu (9 9 11) and (10 10 8) surfaces, and (b) Ni (9 9 11) and (10 10 8) surfaces at 0 K, compared with the displacements of the top two layers of the (111) surface. Dots denote the displacements of atoms of vicinal surfaces, and lines the displacements of the two topmost layers of low-index surfaces. The pattern of the displacements is similar in the two materials, with the amplitude of the displacements being larger for Cu than for Ni. The patterns are distinctive for each surface orientation.

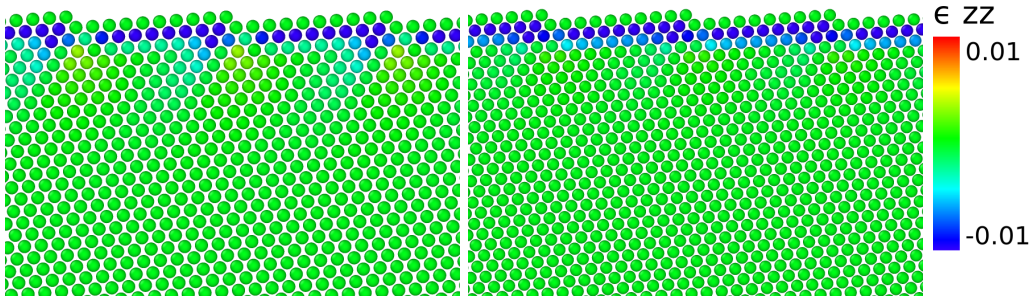



(a) Cu(19 19 1)



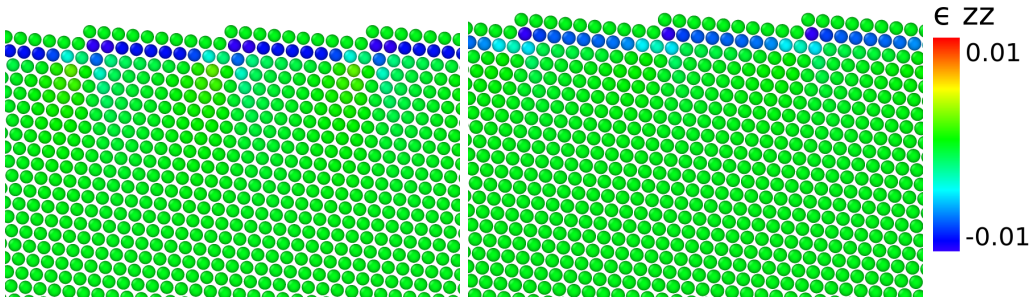

(b) Ni(19 19 1)

Figure 4.8: Displacements in the $z$ direction of Cu (a) and Ni (b) (19 19 1) surfaces at 0 K, compared with the displacements of the top two layers of the (011) surface. Dots denote the displacements of atoms of vicinal surfaces, and lines the displacements of the two topmost layers of low-index surfaces. The pattern of the displacements is similar in the two materials, with the amplitude of the displacements being larger for Cu than for Ni. The patterns are distinctive for each surface orientation.



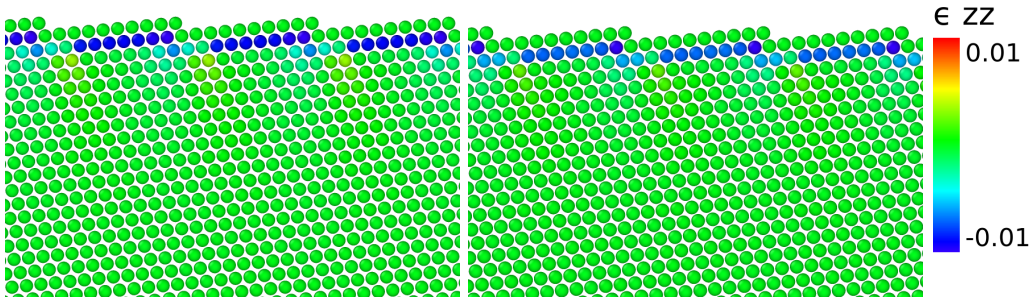

(a) Cu(1 1 19) (b) Ni(1 1 19)

Figure 4.9: Elastic strain field $\epsilon_{zz}$ of Cu and Ni (1 1 19) vicinal surfaces.



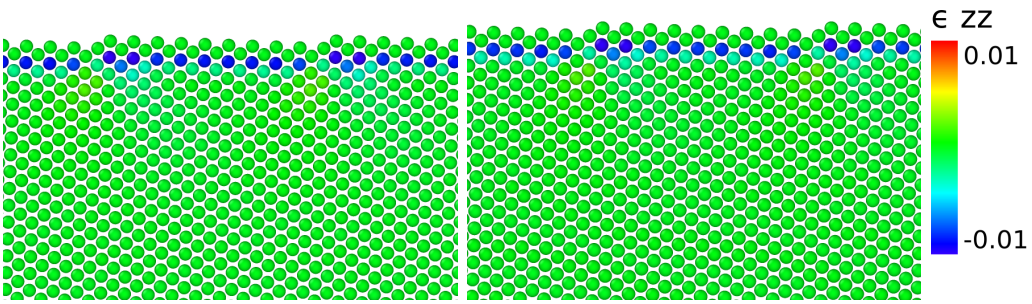

(a) Cu(9 9 11) (b) Ni(9 9 11)

Figure 4.10: Elastic strain field $\epsilon_{zz}$ of Cu and Ni (9 9 11) vicinal surfaces.



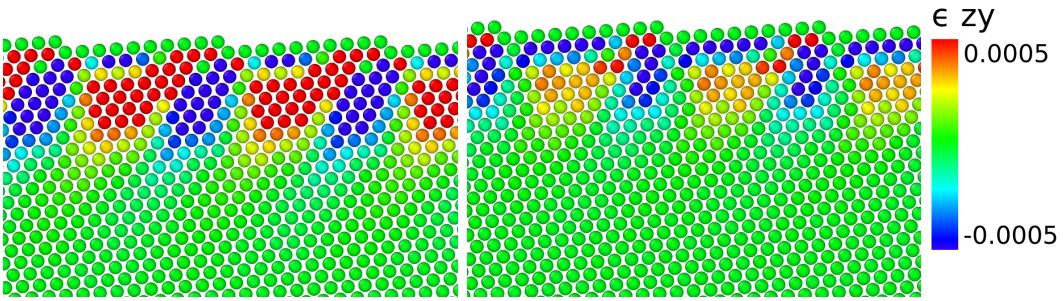

(a) Cu(10 10 8) (b) Ni(10 10 8)

Figure 4.11: Elastic strain field $\epsilon_{zz}$ of Cu and Ni (10 10 8) vicinal surfaces.



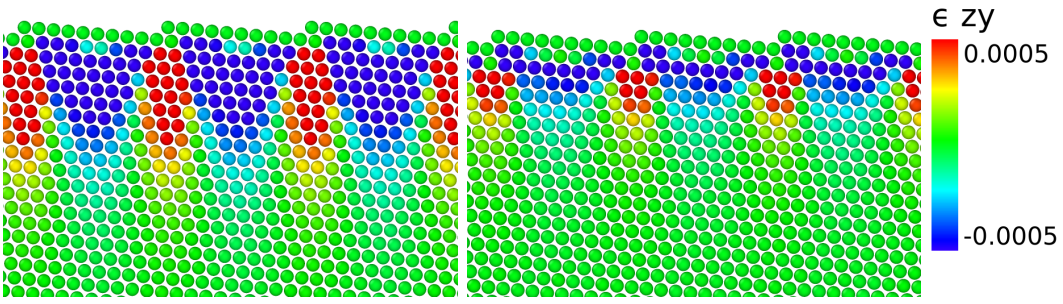

(a) Cu(19 19 1) (b) Ni(19 19 1)

Figure 4.12: Elastic strain field $\epsilon_{zz}$ of Cu and Ni (19 19 1) vicinal surfaces.



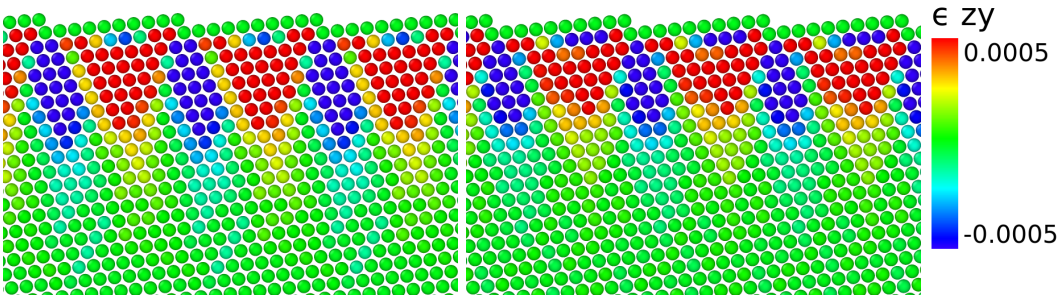

(a) Cu(1 1 19) (b) Ni(1 1 19)

Figure 4.13: Elastic strain field $\epsilon_{zy}$ of Cu and Ni (1 1 19) vicinal surfaces.



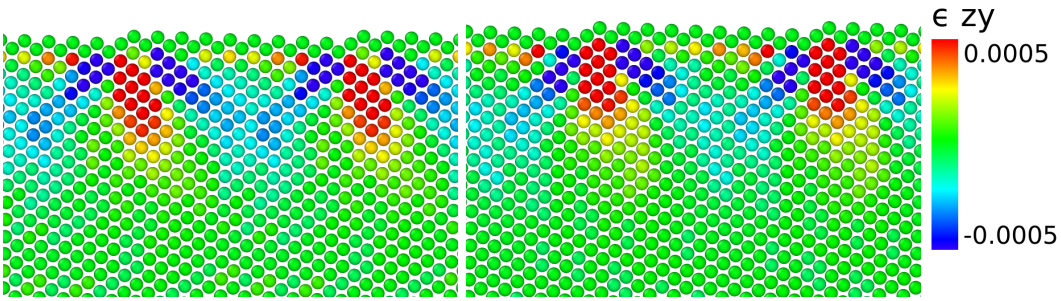

(a) Cu(9 9 11) (b) Ni(9 9 11)

Figure 4.14: Elastic strain field $\epsilon_{zy}$ of Cu and Ni (9 9 11) vicinal surfaces.




(a) Cu(10 10 8) (b) Ni(10 10 8)

Figure 4.15: Elastic strain field $\epsilon_{zy}$ of Cu and Ni (10 10 8) vicinal surfaces.




(a) Cu(19 19 1) (b) Ni(19 19 1)

Figure 4.16: Elastic strain field $\epsilon_{zy}$ of Cu and Ni (19 19 1) vicinal surfaces.

# Chapter 5

# Plastic Deformation

Results of plastic deformation studies of copper and nickel thin films with surface orientations (001) and its vicinal (1 1 19), and (111) and its vicinals (9 9 11) and (10 10 8) equilibrated to 10 K are given in this section. The analysis is twofold, consisting of stress-strain curves and identification of defects that form at the onset of plasticity. The stress-strain curves are obtained from the simulations by logging the stresses and strains at each step of the deformation simulations, and the analysis of the evolution of defects is based on the output of positions of all the atoms in each simulation every 250 steps.

The low temperature and the high strain rate of the simulations influence the deformation mechanisms. At low temperatures the diffusion-controlled processes are suppressed and the main deformation mechanism is slip [67]. At high strain rates the dislocation mobility is lowered, giving precedence to dislocation generation [67]. Low temperatures and high strain rates can also lead the deformation mechanisms to transition from slip to deformation twinning [67]. In our simulations twinning was only observed at very high compressive strains in copper.

Zimmerman et al. [33] studied Au(111) surfaces with single monoatomic steps at 0K and found that the step had no long-range influence on the deformation mechanism, and only when the indenter came into physical contact with the step, did the deformation mechanism beneath the indenter switch from dislocation emission from the surface to slip aligned with the step.

Shan et al. [34] performed a similar study of nanoindentation on thin copper films and also found no long-range effects of the step. In addition, they found that in the case when the indenter came into contact with the step, there was a significant difference in the strength of the first dislocation emission. Apart from that, it was not made clear whether any change in the deformation mechanism was observed.

Lu et al. [36] investigated the effects of surface steps on nanoindentation in Al. They found that the shear stress resulting from the step influences the choice of the active slip systems and lowers the threshold for plastic deformation.

To date no such investigations were performed for nickel vicinal surfaces.

## 5.1 Plastic deformation of the (001) and (1 1 19) surfaces

Results covered in this section have been published in *Scientific Reports* [68], see App. D.

Stress-strain curves of Cu and Ni (001) and (1 1 19) surfaces are shown in Fig. 5.1. Both materials exhibit a significant yield-stress asymmetry, with the yield stress being higher in compression than in tension. Both materials exhibit multiple peaks in the stress-strain curves in tensile deformation, see Fig. 5.1a and 5.1c, and a single pronounced peak in compressive deformation, see Fig. 5.1b and 5.1d.

In the case of Cu(001) surface in tensile deformation, dislocations nucleate at the surface and in the bulk with a pattern of deformation twins emerging at higher strains when stacking faults span the height of the sample. On the other hand, deformation twinning is the only mechanism in compression.

In the case of Ni(001) surfaces, partial dislocations nucleate at the surface, with trailing partials detaching from the surface in the case of compressive deformation, but not in the case of tensile deformation.

For Ni(1 1 19) in tension, the peaks at 5.5 % and 7.5 % strains indicate the activation of the first and the second slip system. For copper in tension, the peak at 6.0 % strain indicates the activation of the first slip system, and the peak at 9.3 % strain the beginning of the twinning. In the case of compression, multiple deformation mechanisms are activated at once at -7.2 % strain for nickel and at -7.1 % strain for copper, leading to a larger and steeper drop in stress compared to the case of tensile deformation.

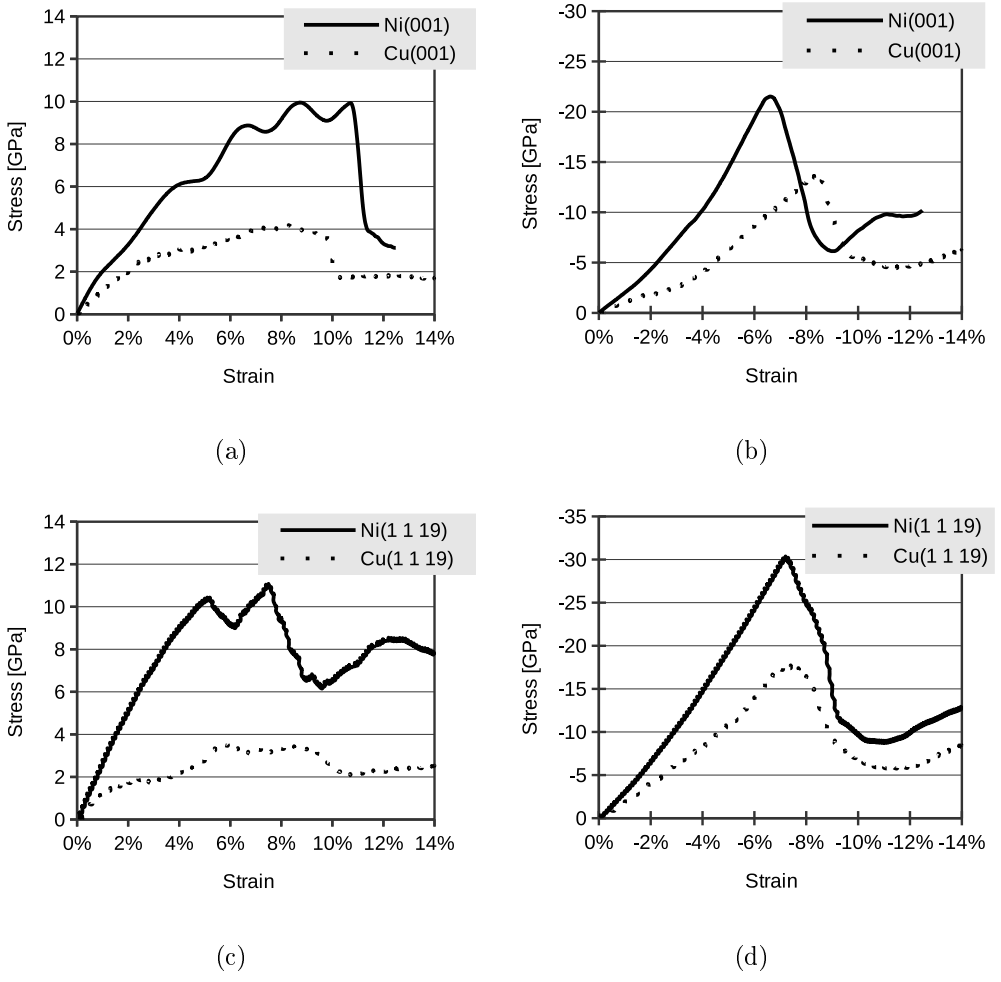



Figure 5.1: Stress-strain curves of Cu and Ni (001) and (1 1 19) surfaces deformed in tension (left column) and in compression (right column). Both materials exhibit a significant yield-stress asymmetry, with the yield stress being higher in compression than in tension. Both materials exhibit multiple peaks in the stress-strain curves in tensile deformation and a single pronounced peak in compressive deformation. The stress scales are not the same for all cases.

The arrays of steps on the (1 1 19) vicinal surfaces influence the deformation mechanisms of both metals. The regularity of the steps is translated into the regularity of the stacking faults that form in all cases.

In the case of copper, steps on the surface serve as nucleation points and both tensile and compressive strains lead to a flattening out of the surface steps. This behavior is analogous with the one expected from the theory of elasticity.

In the case of nickel, the point of dislocation nucleation lies 8–10 layers underneath the surface instead of at the surface. The nucleation sites are the same in tensile and compressive deformation, although in compression the dislocations nucleate at the surface steps as well. The defect nucleation sites buried below the surface are unexpected, since the steps are known as the stress-concentration points. The defect nucleation sites lie beneath the terraces just outside the region affected by the displacement field. In addition, the primary slip system activated in nickel deformed in tension is perpendicular to the primary system activated in copper.

In the case of copper deformed in tension, slip occurs in the (111) plane that delineates two vortices underneath adjacent terraces. The atoms involved slip in the direction of their displacements. In the case of nickel, this process is hindered by the presence of the vortices. Nucleation points are shifted into the bulk beneath the displacement field. Slip occurs in the direction in which crystal symmetry is disturbed the most by the displacement field.

In the case of nickel deformed in compression, nucleation points in the bulk and at the steps are activated. The area of the vortex is again initially avoided, then cut through by the stacking fault originating in the bulk, as was the case in tensile deformation. The nucleation of stacking faults at the steps is in this case not restricted by the displacement field.

To asses the flattening out of the surfaces we noticed in copper, the roughness profiles were derived from [69]

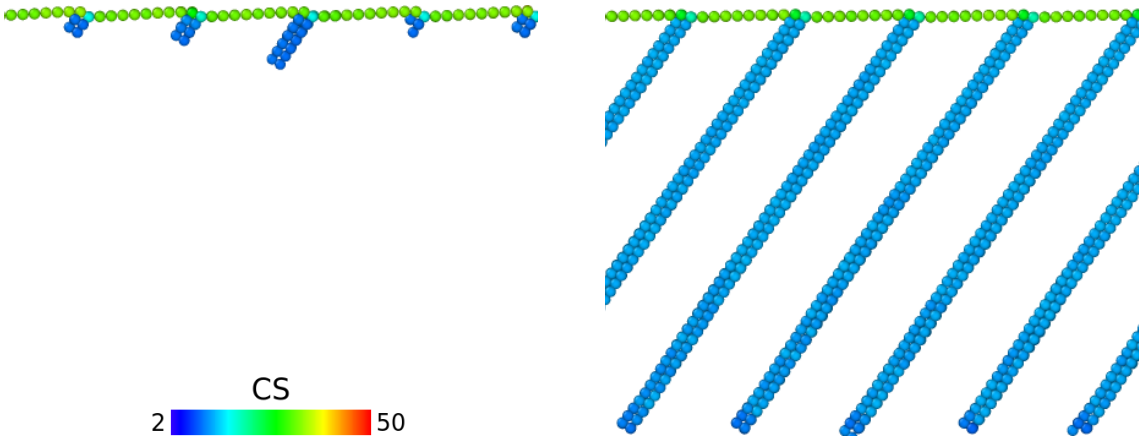
$$R_{\mathrm{a}} = \frac{1}{n}\sum_{i=1}^{n} |z_i - z_m|, \tag{5.1}$$

where $R_a$ is called the arithmetic average of absolute values, $n$ is number of surface atoms, $z_m$ is median $z$ coordinate value for the surface atoms and $z_i$ is the value for the $i$-th atom. The lower $R_{\mathrm{a}}$ the flatter the surface, as $R_{\mathrm{a}}$ gives a measure of how close the atoms are on average to the median $z_m$. The results are given in Table 5.1.

Table 5.1: Roughness profiles for Cu and Ni (1 1 19) vicinals calculated as the arithmetic averages of absolute values $R_{\mathrm{a}}$, see Eq. 5.1. There are clear dips in the values for copper at strains $\pm 5.0\%$. Nickel has a less pronounced dip in the case of compressive deformation at $-5.0\%$ and a pronounced roughening in the case of tensile deformation.

| | Strain | $R_{\mathrm{a}}^{Cu}$ (nm) | $R_{\mathrm{a}}^{Ni}$ (nm) |
|---|---|---|---|
| Compressive | 0.0 % | 0.46 | 0.45 |
| deformation | -2.5 % | 0.50 | 0.48 |
| | -5.0 % | 0.26 | 0.39 |
| | -7.5 % | 0.55 | 0.54 |
| Tensile | 0.0 % | 0.52 | 0.45 |
| deformation | 2.5 % | 0.43 | 0.48 |
| | 5.0 % | 0.13 | 0.89 |
| | 7.5 % | 0.50 | 1.02 |

### 5.1.1 Tensile deformation

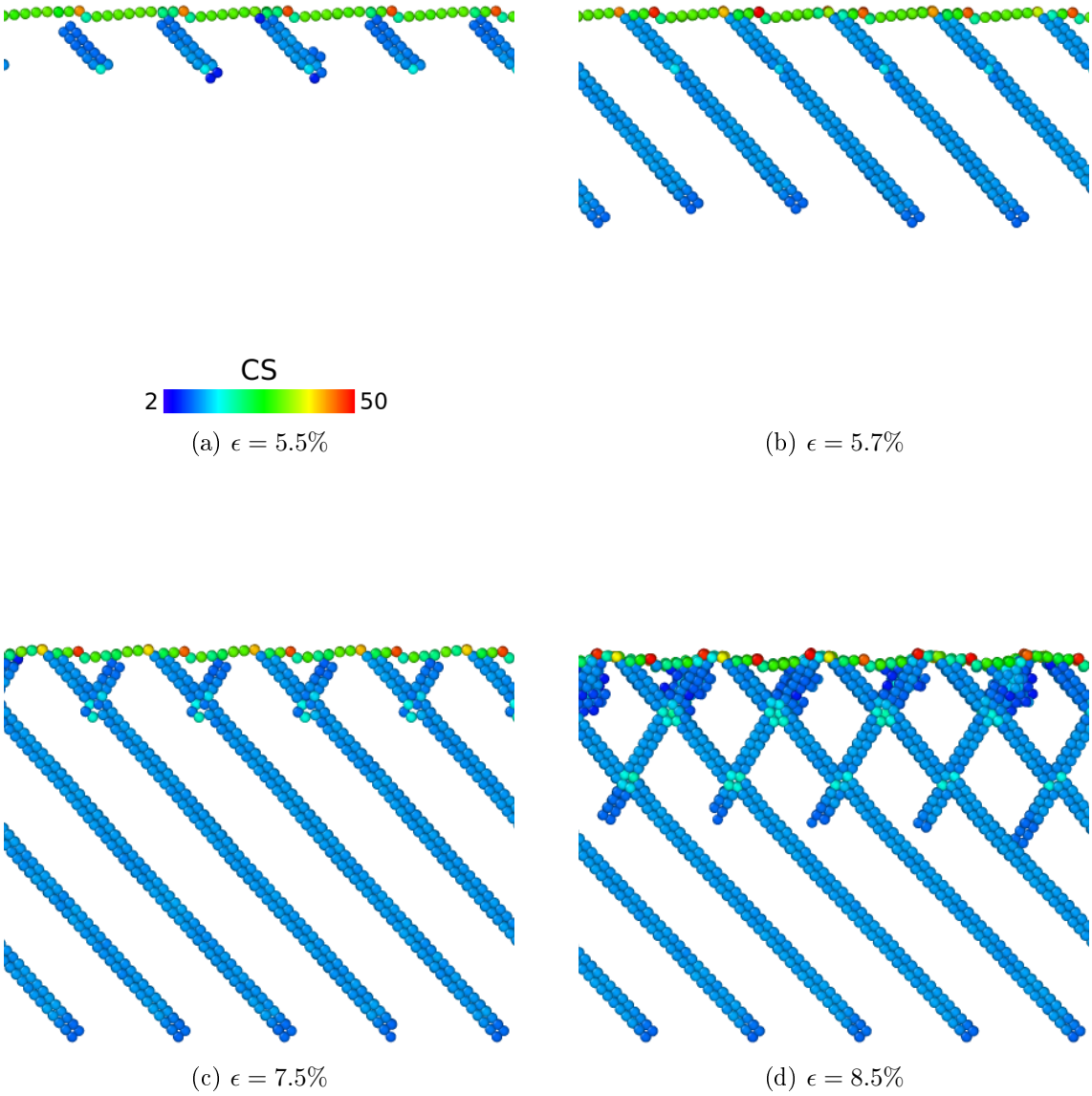



(a) $\epsilon = 6.0\%$ (b) $\epsilon = 6.7\%$

(c) $\epsilon = 10.2\%$ (d) $\epsilon = 10.5\%$

Figure 5.2: Deformation evolution of Cu(1 1 19) deformed in tension. a) Stacking faults nucleate at the surface, b) growing to the bottom of the sample. c) The perpendicular slip system is not activated, instead deformation mechanism switches to twinning. d) The perpendicular slip system is activated, with stacking faults nucleating at the surface and at the bottom of the sample. Atoms comprising surfaces and stacking faults are shown, others ($C_S < 2$) are removed for clarity. The color legend for the centrosymmetry parameter $CS$ included in (a) applies to all figures.

Nucleation and evolution of defects for the Cu(1 1 19) and Ni(1 1 19) surfaces deformed in tension are shown in Fig. 5.2 and 5.3, respectively.




(a) $\epsilon = 5.5\%$ (b) $\epsilon = 5.7\%$

(c) $\epsilon = 7.5\%$ (d) $\epsilon = 8.5\%$

Figure 5.3: Deformation evolution of Ni(1 1 19) deformed in tension. a) Dislocations nucleate in the bulk 8–10 layers underneath the surface. b) The active slip system is perpendicular to the one expected and leads to the formation of additional steps on the surface. c) After the stacking faults reach the bottom of the sample, the next slip system is activated. Partial dislocations nucleate at the same nucleation sites in the bulk, grow towards the surface and then into the bulk. d) At strains above 8.0 % a set of stacking faults begins to grow into twins. Atoms comprising surfaces and stacking faults are shown, others ($C_S < 2$) are removed for clarity. The color legend for the centrosymmetry parameter $C_S$ included in (a) applies to all figures. Atoms colored in dark orange are step edge atoms.

In the case of Cu, Shockley partial dislocations nucleate at the steps on the surface and climb into the bulk, creating stacking faults reaching from the surface ever deeper into the bulk with increasing strain, see Fig. 5.2a. Slip reduces the height of the steps and leads to a flattening-out of the surface (roughness profile is given in Table 5.1). No trailing partials detach from the surface. When the stacking faults reach the layer of fixed atoms at the bottom of the simulation box, partial cross-slip of the existing stacking faults occurs, see Fig. 5.2b, before the perpendicular slip direction is activated, see Fig. 5.2c,d.

In the case of Ni, dislocations nucleate in the bulk, 8–10 layers below the surface, see Fig. 5.3a. Shockley partial dislocations first climb towards the surface, where they intersect with the terraces and not with the steps. Slip introduces new steps on the surface, see Fig. 5.3b. Stacking faults then continue growing into the bulk of the sample by dislocation climb in the opposite direction in the same slip plane. When the stacking faults reach the layer of fixed atoms at the bottom of the sample, the slip system with the perpendicular slip direction is activated. These stacking faults originate at the same nucleation sites as the previous set. Another set of steps is introduced at the surface and a crosswise pattern of stacking faults emerges in the bulk (see Fig. 5.3d). The roughening of the surface is apparent also from the roughness profile given in Table 5.1, with $R_a$ values going from 0.45 nm at 0.0 % strain to 1.02 nm at 7.5 % strain.

In comparison, dislocations nucleate at the surface steps in copper and in the bulk in nickel. The steps on the surface act as stress concentrators and are the expected nucleation sites. In both metals the dislocations nucleate and travel evenly along the whole length of the simulated samples in the **x** direction, parallel to the direction of the steps. In addition, the primary slip system in copper is the one expected to be activated in tensile deformation, leading to a flattening-out of the surface. In the case of nickel the primary slip system is perpendicular to the one expected and leads to the formation of additional steps on the surface. Cross-slip is observed in copper but not in nickel.

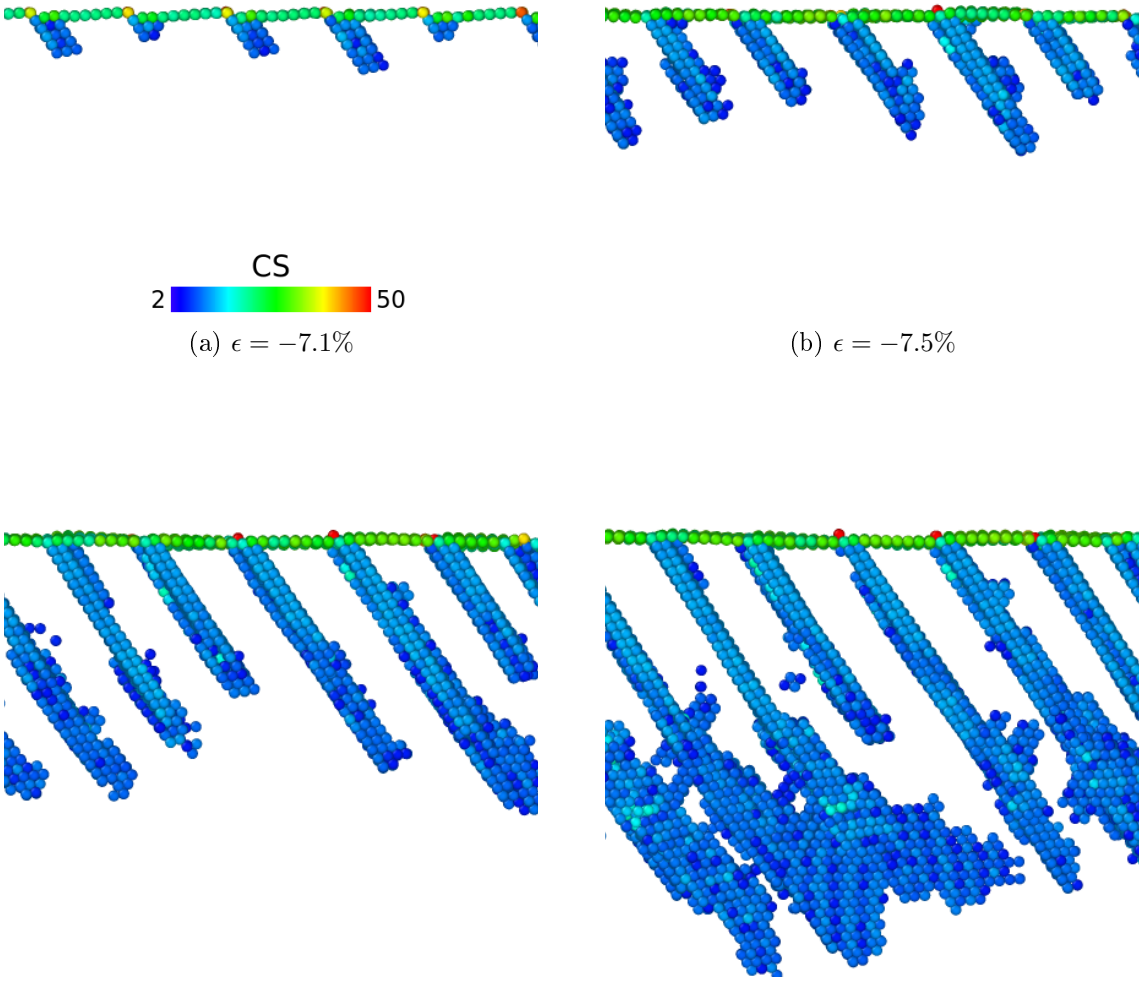
### 5.1.2 Compressive deformation

The nucleation and evolution of defects for the Cu(1 1 19) and Ni(1 1 19) surfaces deformed in compression are shown in Fig. 5.4 and 5.5, respectively.

In the case of copper deformed in compression, dislocations nucleate at the edges of the terraces, see Fig. 5.4a. The slip direction is perpendicular to the one active in tensile deformation. Cross-slip is activated and stacking faults grow wider than in the case of tensile deformation. Slip again flattens out the surface, as is evident in Table 5.1. Trailing partial dislocations nucleate at the surface in some places. Deformation mechanisms in the bulk are in this case distinct from the deformation of the surface, as deformation twinning occurs at a depth of 5–10 nm in the simulated sample, see Fig. 5.4b. The slip system perpendicular to the primary one is not activated in this case.

In the case of nickel deformed in compression, dislocations nucleate at the surface and in the bulk, Fig. 5.5a. One set of partial dislocations nucleates at the edges of the terraces. Hindered by the dislocations nucleating in the bulk, these partial dislocations cross-slip along the terraces instead of climbing deeper into the bulk. At the same time a distinct set of dislocations is nucleating in the bulk, 8–10 layers below the surface. The placement of the nucleation sites is the same as in the case of nickel deformed in tension. Three partial dislocations detach from these nucleation cores: two follow the slip direction of the dislocations nucleating at the surface and the third follows the perpendicular one, Fig. 5.5b. A complex crosswise pattern of dislocations emerges, Fig. 5.5c. The surface is flattened to a lesser degree than in the case of copper, see Table 5.1, then irregular steps appear with additional slip at higher strains.

In comparison, the bulk nucleation sites are observed in nickel, but not in copper.



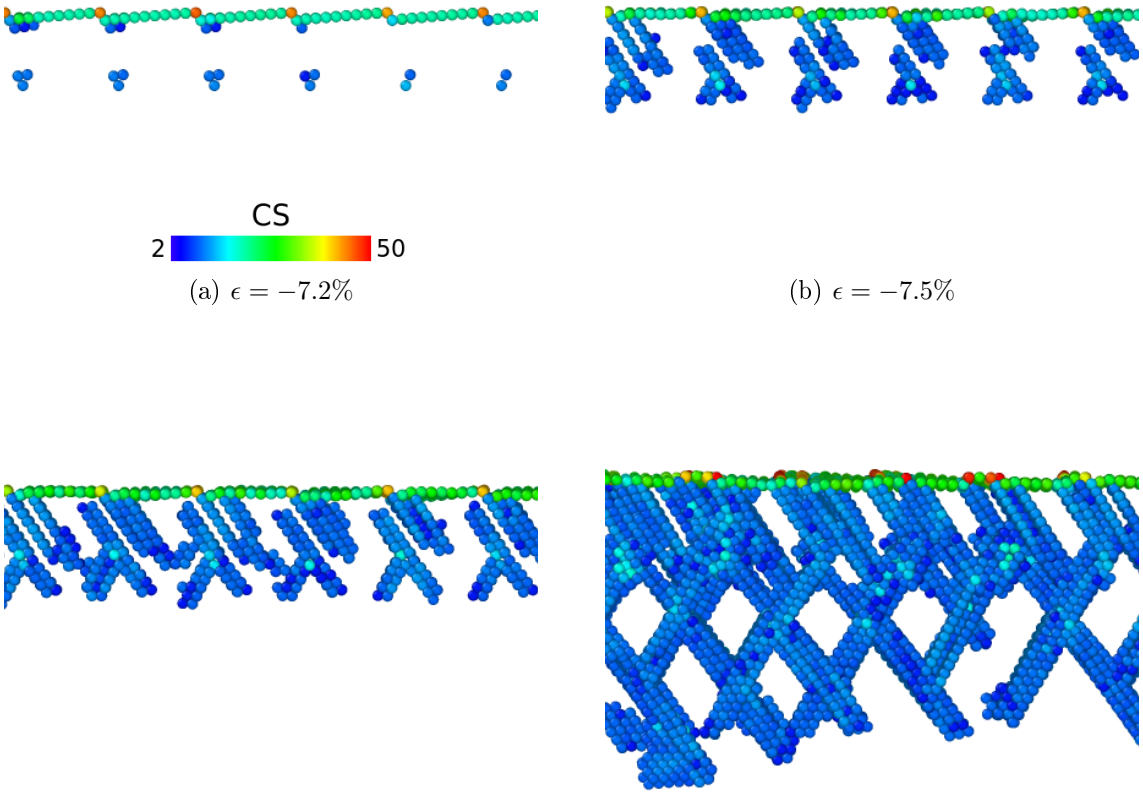

(a) $\epsilon = -7.1\%$ (b) $\epsilon = -7.5\%$

(c) $\epsilon = -8.3\%$ (d) $\epsilon = -8.5\%$

Figure 5.4: Deformation evolution of Cu(1 1 19) deformed in compression. a) Defects nucleate at the steps on the surface. b) Parallel twins grow into the bulk along the direction of the active slip system. c and d) Deformation twinning remain the prevailing deformation mechanism, the perpendicular slip system is not activated. Atoms comprising surfaces and stacking faults are shown, others ($C_S < 2$) are removed for clarity. The color legend for the centrosymmetry parameter $C_S$ included in (a) applies to all figures. Atoms colored in red are single adatoms on the surface.

Two perpendicular slip systems are active in nickel, but only one in copper. Deformation twinning occurs in copper, but not in nickel.

In both materials there seems to exist an extended near-surface volume, comprising of approximately 10 layers in nickel and approximately 5 nm in copper. The interface between the near-surface and bulk-like volumes is well defined in Ni by the rows of nucleation points. It is less obvious in copper, but the bulk-like volume undergoes deformation twinning in compression, while the near-surface area does not. This leads us to conclude that the near-surface volumes have their own elastic constants and stacking fault energies that are




(a) $\epsilon = -7.2\%$

(b) $\epsilon = -7.5\%$

(c) $\epsilon = -7.7\%$

(d) $\epsilon = -8.2\%$

Figure 5.5: Deformation evolution of Ni(1 1 19) deformed in compression. a) Dislocations nucleate in the bulk 8–10 layers underneath the surface as well as at the steps. b) From the nucleation sites in the bulk, stacking faults grow in three directions, utilizing two slip planes. Stacking faults originating at the steps switch to twinning at the strain of $-7.3$ %. c) Stacking faults and twins connect. d) Defects grow into the bulk evenly along both active slip systems. Atoms comprising surfaces and stacking faults are shown, others ($C_S < 2$) are removed for clarity. The color legend for the centrosymmetry parameter $C_S$ included in (a) applies to all figures. Atoms colored in orange are step edge atoms.

significantly different from those in the bulk and that a transition between those areas is sharp in nickel, in effect creating an ingrain boundary, and more gradual in copper, closer to what we would expect from elasticity theory.

### 5.1.3 Summary

To summarize, in tensile deformation, dislocations nucleate at the surface steps in copper and in the bulk in nickel. The steps on the surface act as stress concentrators and are

the expected nucleation sites. The primary slip system in copper is the one expected to be activated in tensile deformation, leading to a flattening-out of the surface. In the case of nickel the primary slip system is perpendicular to the one expected and leads to the formation of additional steps on the surface. Cross-slip is observed in copper but not in nickel. In compression, the bulk nucleation sites are observed in nickel, but not in copper. Two perpendicular slip systems are active in nickel, but only one in copper. Deformation twinning occurs in copper, but not in nickel.

We conclude that the near-surface volumes have their own elastic constants and stacking fault energies that are significantly different from those in the bulk and that a transition between those volumes is sharp in nickel, in effect creating an ingrain boundary, and more gradual in copper, closer to what we would expect from elasticity theory.

## 5.2 Plastic deformation of the (111) surface and its vicinals, (9 9 11) and (10 10 8)

Results covered in this section have been published in *Materials and Technology* [70], see App. E.

Stress-strain curves of Cu and Ni (111), (9 9 11) and (10 10 8) surfaces are shown in Fig. 5.6. Both materials exhibit a significant yield-stress asymmetry, with the yield stress being higher in compression than in tension. Both materials exhibit stress-strain curves with a single pronounced peak. Only in the case of the Ni(10 10 8) surface deformed in compression, see Fig. 5.6f, there is a plateau at the strain of $-8$ % when stacking faults nucleate at the steps on the surface and grow into the bulk and the main peak is moved to higher strains compared to the (111) and (9 9 11) surfaces when other slip systems activate.

In the case of the (111) surfaces, the deformation mechanisms are the same for both materials. In tensile deformation dislocations nucleate in the bulk and at the surface with no partial dislocations detaching from the surface, while in compressive deformation dislocations nucleate in the bulk and at the surface and trailing partials detach from the surface.

From the stress-strain curves, we expect the deformation mechanisms of the (10 10 8) surfaces to differ from others the most.

### 5.2.1 Tensile deformation

Deformation mechanisms of the (9 9 11) and (10 10 8) surfaces deformed in tension are characterized by the presence of the stair-rod dislocations, that are especially prevalent in copper but also present in nickel.

Active slip systems are the ones expected from crystallographic analysis. Dislocations are not aligned with the steps, although the steps serve as pinning sites, catching the dislocations as if in a well.

#### 5.2.1.1 (9 9 11)

Partial dislocations nucleate in the middle of the terraces in copper and trailing partials detach from the surface, see Fig. 5.7. Partial dislocations nucleate at the steps in nickel, see Fig. 5.8. Stair-rod dislocations form as partial dislocations interact in both materials.

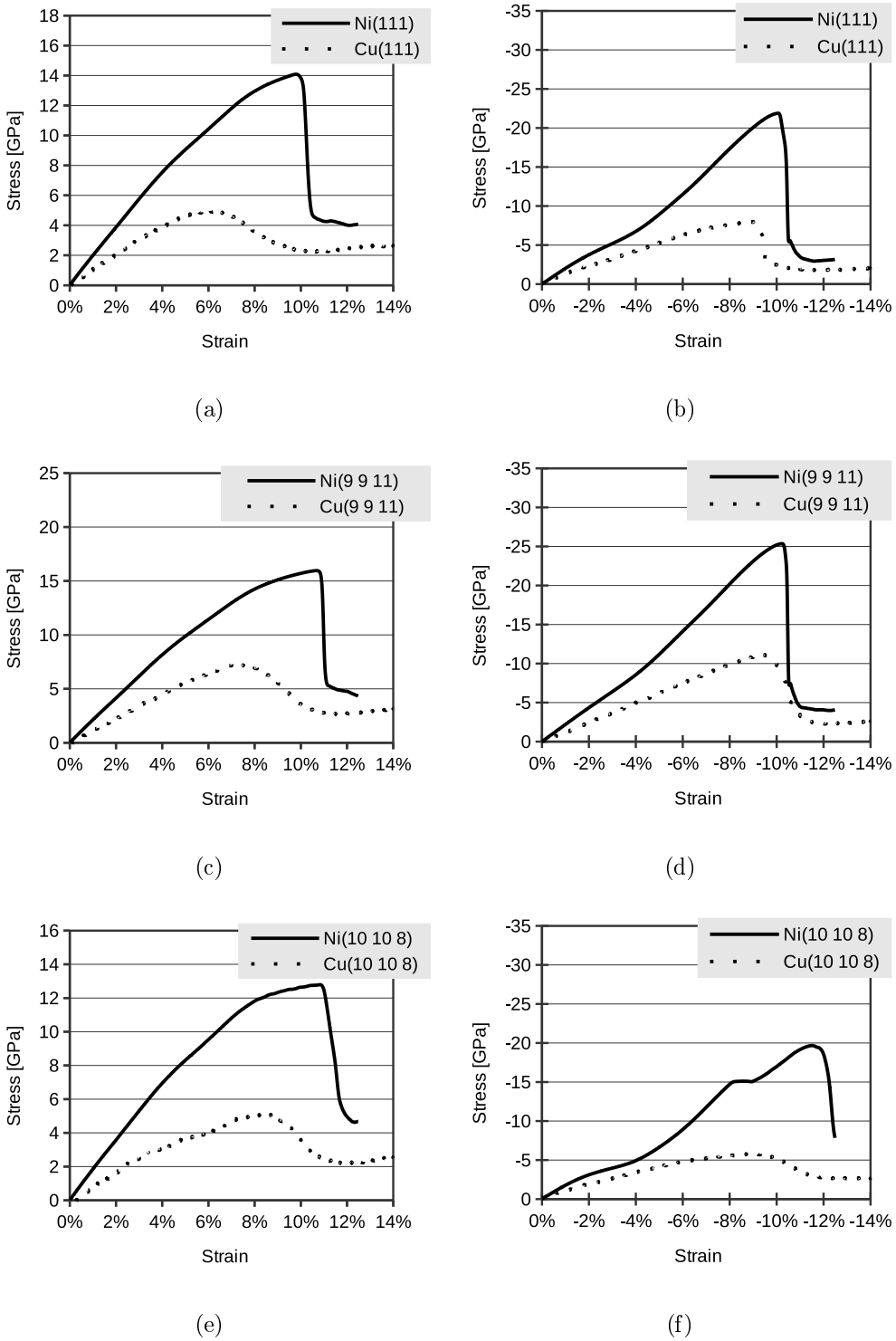
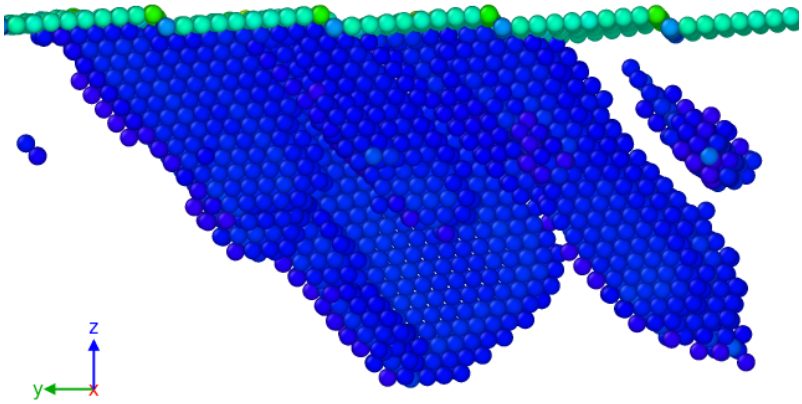
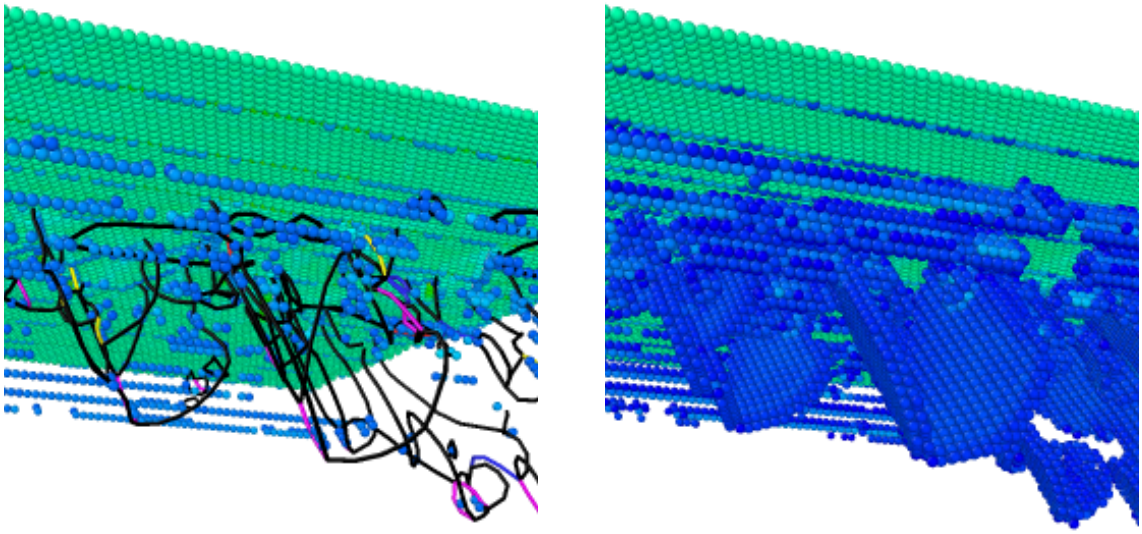



Figure 5.6: Stress-strain curves of Cu and Ni (111), (9 9 11) and (10 10 8) surfaces deformed in tension (left column) and in compression (right column). Both materials exhibit yield-stress asymmetry, with the yield stress being higher in compression than in tension. Stress-strain curves have a single pronounced peak. Only in the case of the Ni(10 10 8) surface deformed in compression, there is a plateau at the strain of $-8$ % when stacking faults nucleate along the steps, and the main peak is moved to higher strains compared to the (111) and (9 9 11) surfaces when other slip systems activate. The stress scales are not the same for all cases.

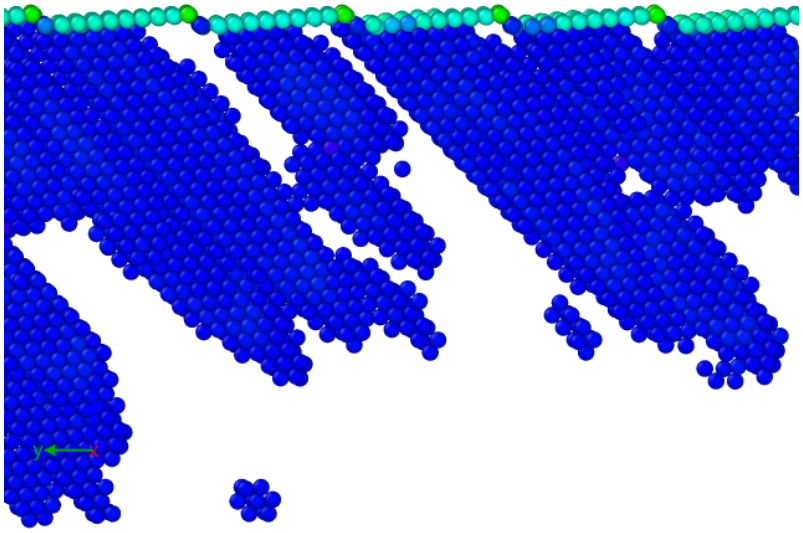



(a)

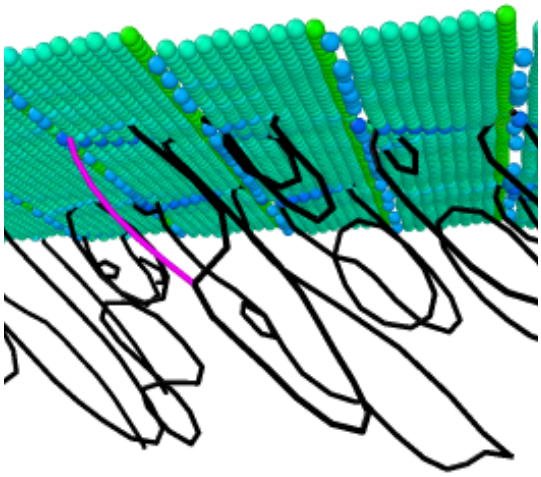


(b) (c)

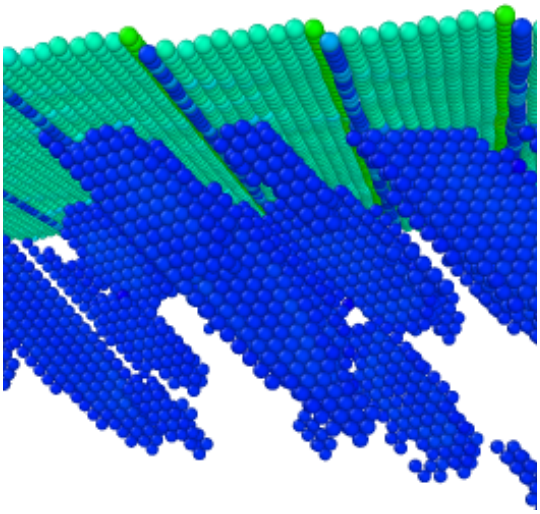
Figure 5.7: Tensile deformation of the Cu(9 9 11) surface. A side view is shown in (a) and a 3D view from beneath the surface is shown in (b and c). Partial dislocations nucleate at the surface. Partial dislocations are shown as lines in (b) and atoms with $C_S < 2$ are removed in (a and c), while atoms with $C_S < 7$ are removed in (b). (b) Shockley partial dislocations, shown as black lines, combine to form stair-rod dislocations, colored pink.



(a)



(b)

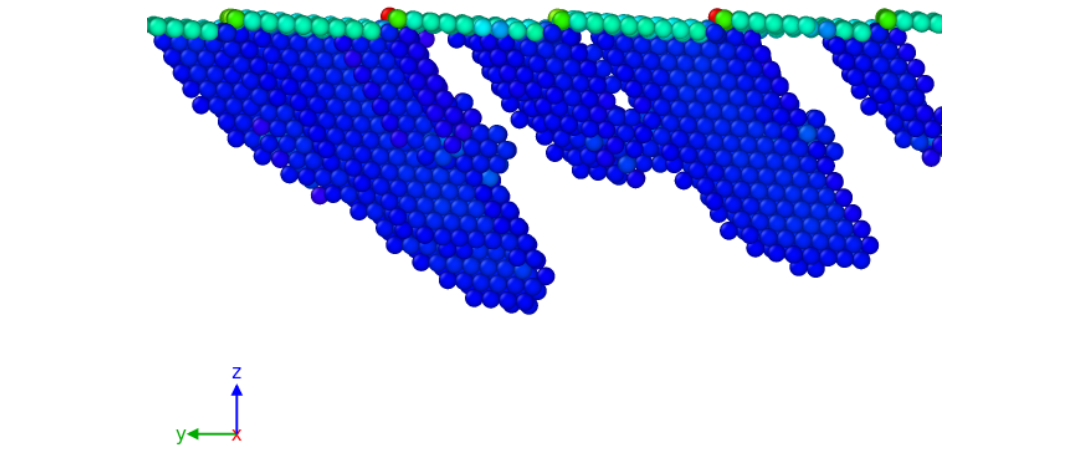


(c)

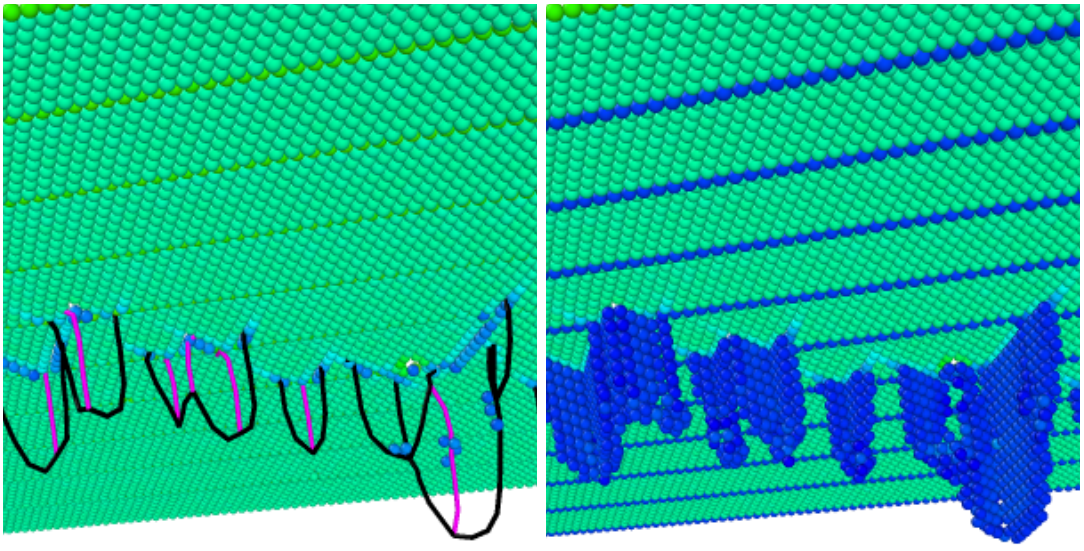
Figure 5.8: Tensile deformation of the Ni(9 9 11) surface. A side view is shown in (a) and a 3D view from beneath the surface is shown in (b and c). Partial dislocations nucleate at the surface. Dislocations are shown as lines in (b) and atoms with $C_S < 2$ are removed in (a and c), while atoms with $C_S < 7$ are removed in (b). (b) Shockley partial dislocations, shown as black lines, combine to form stair-rod dislocations, colored pink.

#### 5.2.1.2 (10 10 8)

Stair-rod dislocations nucleate at the steps in copper and no trailing partials detach from the surface, see Fig. 5.9. Partial dislocations straddle the steps in nickel, also with no trailing partial dislocations; stair-rod dislocations form as partial dislocations interact, see Fig. 5.10.

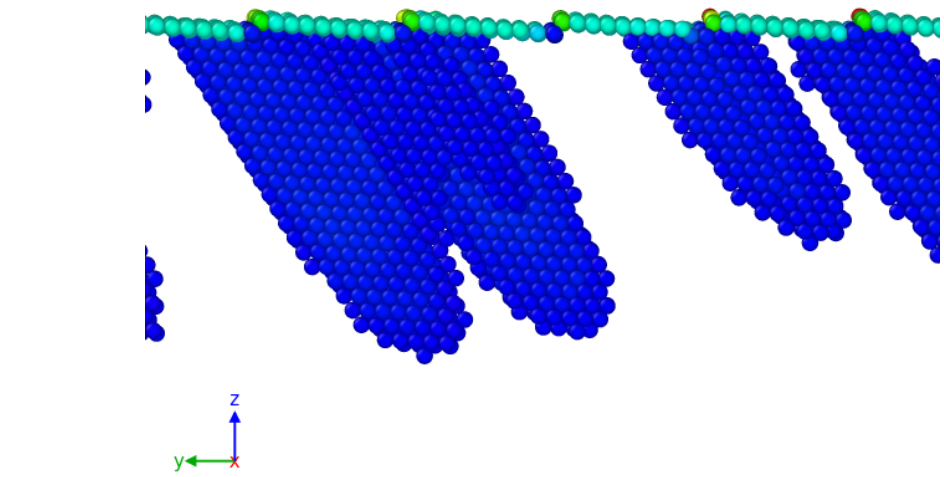



(a)

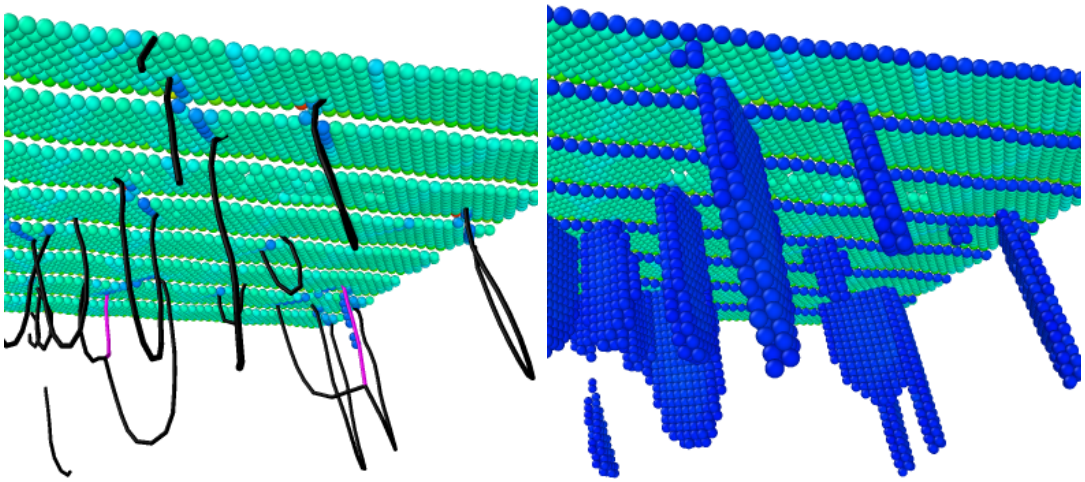


(b) (c)

Figure 5.9: Tensile deformation of the Cu(10 10 8) surface. A side view is shown in (a) and a 3D view from beneath the surface is shown in (b and c). Partial dislocations nucleate at the surface. Partial dislocations are shown as lines in (b) and atoms with $C_S < 2$ are removed in (a and c), while atoms with $C_S < 7$ are removed in (b). (b) Shockley partial dislocations, shown as black lines, combine to form stair-rod dislocations, colored pink.




(a)



(b) (c)

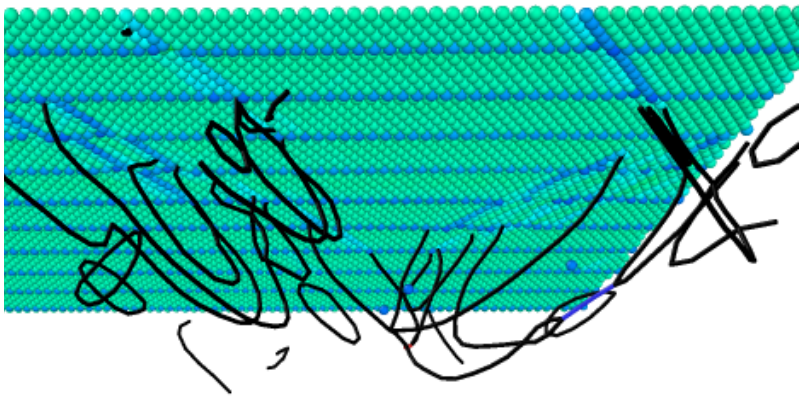
Figure 5.10: Tensile deformation of the Ni(10 10 8) surface. A side view is shown in (a) and a 3D view from beneath the surface is shown in (b and c). Partial dislocations nucleate at the surface. Dislocations are shown as lines in (b) and atoms with $C_S < 2$ are removed in (a and c), while atoms with $C_S < 7$ are removed in (b). (b) Shockley partial dislocations, shown as black lines, combine to form stair-rod dislocations, colored pink.

### 5.2.2 Compressive deformation

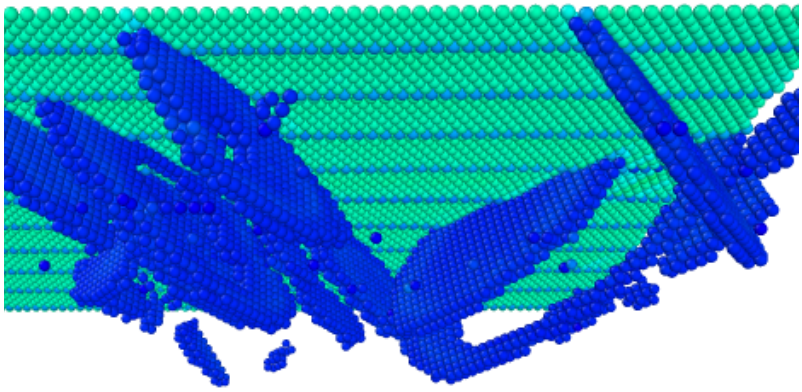
Copper and nickel have analogous deformation mechanisms, distinct for each surface orientation. Primary slip systems are activated in (9 9 11) oriented surfaces, whereas stacking faults aligned with the steps are the initial defects forming in (10 10 8) oriented surfaces and other slip systems are delayed.

#### 5.2.2.1 (9 9 11)

In the cases of the (9 9 11) surfaces, Fig. 5.11 and 5.12, partial dislocations nucleate at the surfaces, but are not aligned with the steps. Trailing partial dislocations detach from the surface. No other deformation mechanisms are active.



(a)

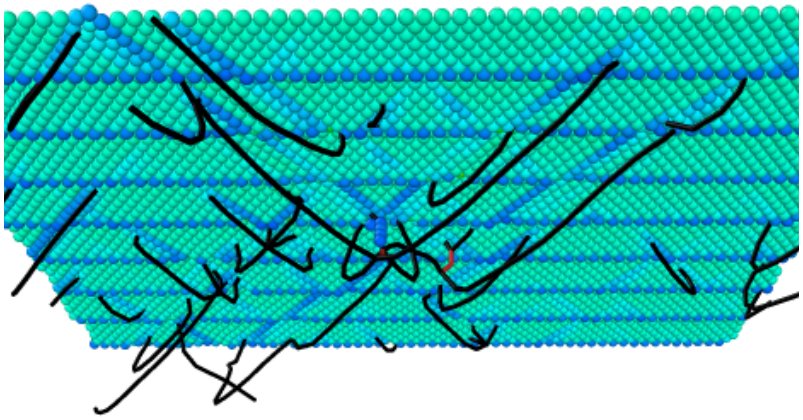


(b)

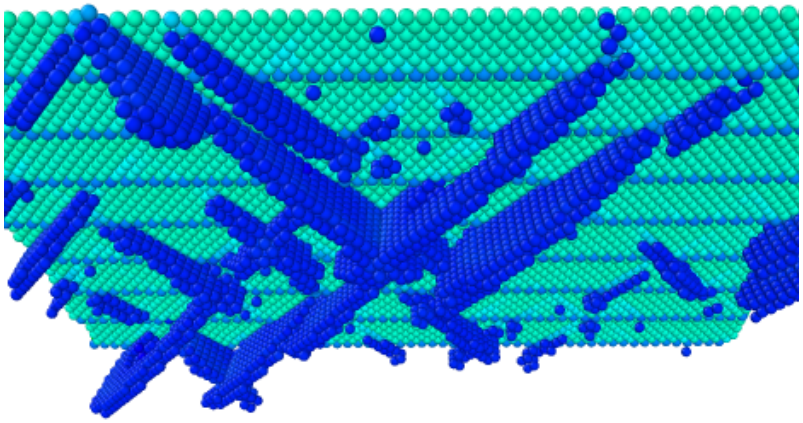
Figure 5.11: Compressive deformation of the Cu(9 9 11) surface. Partial dislocations nucleate at the surface. Partial dislocations are shown as lines and atoms with $C_S < 7$ are removed in (a) and atoms with $C_S < 2$ are removed in (b).

This deformation mechanism is analogous with the deformation mechanism of the (111) surfaces, except that no dislocations form in the bulk.

Steps on the surfaces act as pinning points for the dislocations.



(a)



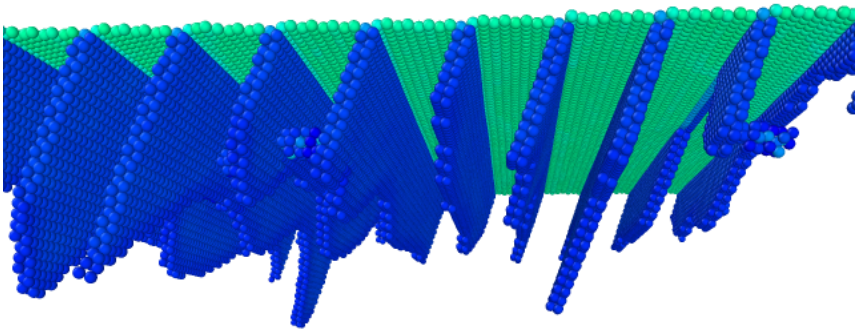
(b)

Figure 5.12: Compressive deformation of the Ni(9 9 11) surface. Partial dislocations nucleate at the surface. Dislocations are shown as lines and atoms with $C_S < 7$ are removed in (a) and atoms with $C_S < 2$ are removed in (b).

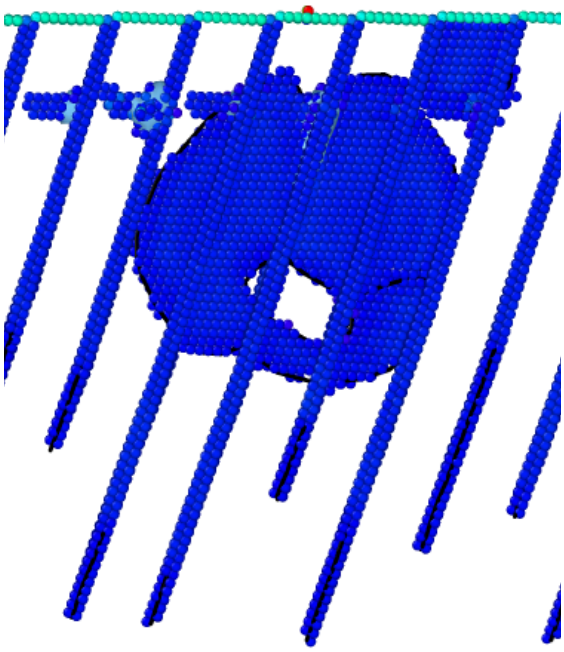
#### 5.2.2.2 (10 10 8)

The deformation mechanism of (10 10 8) deformed in compression is clearly influenced by the presence of the steps, see Fig. 5.13 and 5.14. The pre-existing compressive strains introduced by the displacements of the atoms due to the steps on the surfaces contribute to the nucleation of stacking faults aligned with the steps.

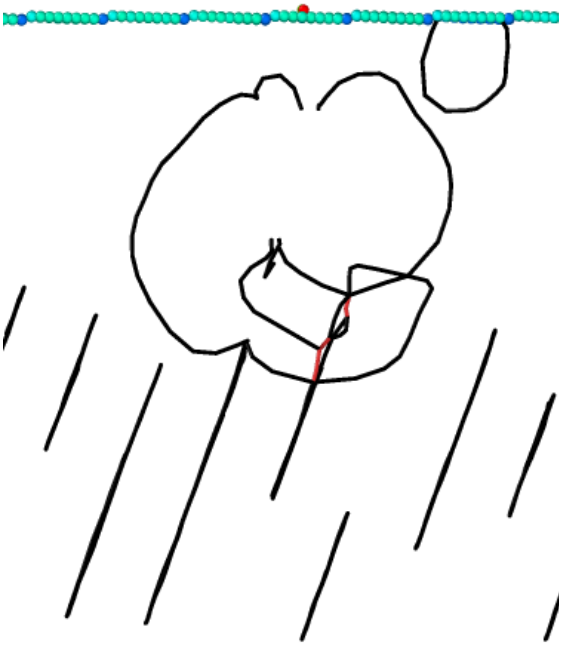
In the cases of the (10 10 8) surfaces the deformation mechanism is two-part. First, stacking faults nucleate at the surfaces aligned with the steps and grow into the bulk, see Fig. 5.13a and 5.14a. Secondly, partial dislocations form along the alternative slip systems, see Fig. 5.13b,c and 5.14b,c. In the case of nickel, the stacking faults reach the bottom of the sample before the alternative slip systems are activated, but not in copper.



(a) $\epsilon = -8$ %

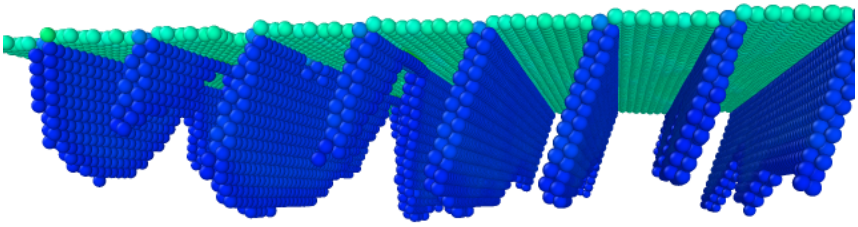


(b) $\epsilon = -11$ %

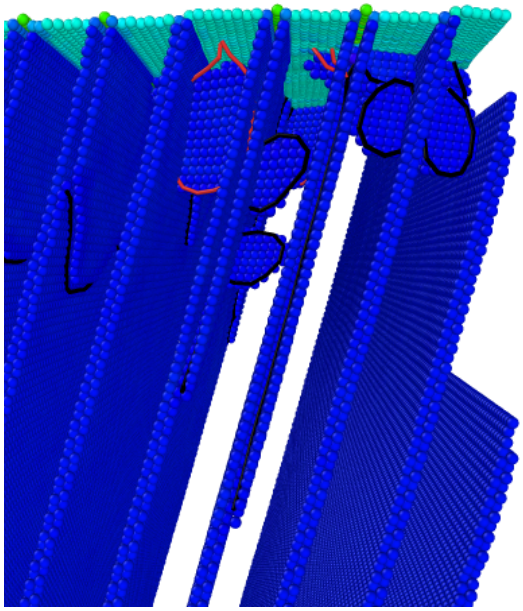


(c) $\epsilon = -11$ %

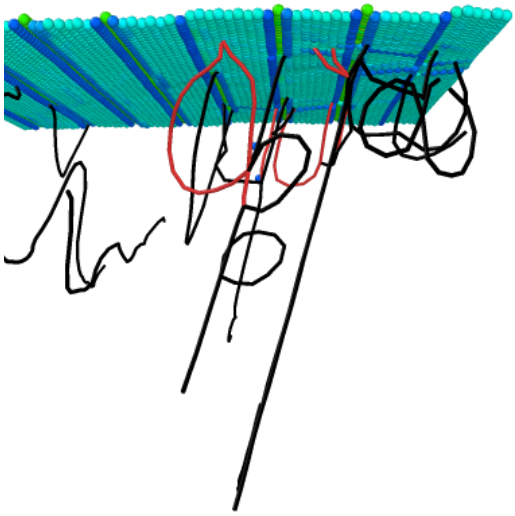
Figure 5.13: Compressive deformation of the Cu(10 10 8) surface. a) Stacking faults aligned with the steps nucleate at the surface at the strain of $-8$ %. b and c) Additional slip systems are activated at the strain of $-11$ %. Black lines denote Shockley partial dislocations. Red lines denote other types of dislocations. The red atom is a single adatom. Atoms with $C_S < 2$ are removed in (a and b), while atoms with $C_S < 7$ are removed in (c).



(a) $\epsilon = -8$ %



(b) $\epsilon = -12$ %



(c) $\epsilon = -12$ %

Figure 5.14: Compressive deformation of the Ni(10 10 8) surface. a) Stacking faults aligned with the steps nucleate at the surface at the strain of $-8$ %. b and c) Additional slip systems are activated at the strain of $-12$ %. Black lines denote Shockley partial dislocations, and red lines other types of dislocations. Atoms with $C_{\mathrm{S}} < 2$ are removed in (a and b), while atoms with $C_{\mathrm{S}} < 7$ are removed in (c).

### 5.2.3 Summary

In summary, in the cases of the surfaces vicinal to (111) we investigated, copper and nickel have analogous deformation mechanisms. Deformation mechanisms do vary with respect to the surface orientation and polarity of strain.

The (9 9 11) surfaces deform by partial dislocations along primary slip systems which are not aligned with the steps regardless of strain polarity. Alas, stair-rod dislocations that form in tensile deformation are absent in compressive deformation.

The (10 10 8) surfaces deform in tension by partial dislocation nucleation along the primary slip systems, while the deformation mechanism in compression is two-step: stacking faults aligned with the steps on the surfaces form at first, and alternative slip systems are activated at higher strains.

We conclude that the distinction between the A-steps forming (9 9 11) vicinals, and the B-steps forming (10 10 8) vicinals, is an important one with regard to the deformation mechanisms.

# Chapter 6

# Conclusions

The uniaxial deformation of copper and nickel thin films with low-index and vicinal surfaces was investigated by molecular dynamics and statics simulations.

In answer to the hypotheses (Sec. 1.2), the following conclusions were reached:

1. The study confirms that elastic fields emerging on the vicinal surfaces due to the presence of equidistant steps disrupt the lattice symmetry of the near-surface atoms and play a role in the response of the surfaces to uniaxial tensile and compressive strains, leading to material-dependent positioning and activity of the nucleation sites. In the cases of the (1 1 19) vicinals, there is a clear distinction between the near-surface and bulk-like volume. In the case of Ni(1 1 19) the transition between the two volumes is sharp, in effect forming an ingrain boundary marked by the series of nucleation points. In the case of Cu(1 1 19) the difference is visible in the different deformation mechanisms: the bulk-like volume deforms by twinning, whereas the near-surface volume does not. We conclude that the near-surface and bulk-like volumes differ in elastic constants and stacking fault energies.

2. The strain required for plastic deformation is different for tensile deformation compared to compressive deformation, which was confirmed by yield stress asymmetry in all the cases. In multiple cases the yields stress asymmetry is accompanied by the differences in the deformation mechanisms, which include different nucleation points and different active slip systems.

3. Defect nucleation mechanisms vary with regard to strain-axis inclination. It is important as well, whether the strain-axis inclination is aligned with the primary slip systems in a thin film. The primary slip systems were aligned with the strain axis in the case of the (1 1 19) surface, but not in the cases of (9 9 11) and (10 10 8). In the case of the (10 10 8) surface, the influence of the steps led to a switch in the deformation mechanisms: stacking faults aligned with the steps formed in compression, but not in tension. Additionally, as the stacking-fault energy of nickel is higher than that of copper, it was expected that any possible transitions of deformation mechanisms from dislocation emission to stacking-fault nucleation to twinning will occur at lesser strains in copper than in nickel, and this was indeed the case.

## 6.1 Contribution to Science

1. This thesis represents the first molecular-dynamics-based simulation of uniaxial deformation for the vicinal surfaces of copper and nickel, showing that elastic fields of vicinal surfaces play a role in the deformation mechanisms of these surfaces beyond

that described by elasticity theory. The ambiguous material-dependent positioning and activity of the nucleation sites in the cases of the (1 1 19) surfaces, where dislocations nucleate at the surface steps in copper, while in nickel dislocations form in the bulk in tensile deformation and in the bulk as well as at the steps in compressive deformation, indicates the importance of displacement fields of vicinal surfaces for the deformation mechanisms of vicinal surfaces. We believe that the near-surface areas have their own elastic constants and stacking fault energies that are significantly different from those in the bulk and that a transition between those areas is sharp in Ni(1 1 19), in effect creating an ingrain boundary, and more gradual in Cu(1 1 19), closer to what we would expect from elasticity theory.

2. A switch in active slip systems from those predicted by geometric analysis to those aligned with the steps is possible in the case of vicinal surfaces deformed with uniaxial loading, but it occurs for specific orientations of the surfaces and strains.

3. The distinction between the A-steps forming (9 9 11) vicinals, and the B-steps forming (10 10 8) vicinals, is an important one with regard to the deformation mechanisms. The two step types result in distinct elastic strain fields with opposite compressive and tensile areas. This in turn leads to two different deformation mechanisms in compression: in the cases of the (9 9 11) surfaces dislocations are aligned with geometrically expected slip systems, and in the cases of the (10 10 8) surfaces stacking faults are aligned with the steps.

4. The influence of the polarity of the strain is noticeable in all the cases through the yield stress asymmetry exhibited by both materials. In multiple cases it is additionally emphasized by the difference in the deformation mechanisms, of which the most glaring example are the (10 10 8) surfaces, that only deform by the parallel stacking faults aligned with the steps in compressive deformation, but not in tensile deformation.

5. The deformation mechanisms of vicinal surfaces are dependent on the strain-axis inclination. For instance, we have observed twinning in the deformation of (1 1 19) surfaces, but not in the other cases. In addition, as was expected from the values of their stacking fault energies, transitions of deformation mechanisms from dislocation emission to stacking fault nucleation to twinning occur at lesser strains in copper than in nickel.

## 6.2 Outlook

This study has shown that vicinal surfaces exhibit deformation mechanisms different from low-index surfaces and that the displacement fields induced by the steps on the surfaces lead to a variety of deformation mechanisms. A more comprehensive study of the influence of strain-axis inclination with regard to the surface orientation could give a clearer picture of when deformation mechanisms switch and why. The influence of shear could also be investigated.

With regard to the simulation parameters, there are several options. Thicker films could be investigated to asses any simulation boundary artifacts. Also thinner films could be investigated to asses a thickness at which no discernible bulk properties remain, especially for the cases that exhibit a clear difference in properties or deformation mechanisms between the near-surface and the bulk-like volumes as is the case in the (1 1 19) vicinals. Similarly effective would be symmetric boundary conditions in the $z$ direction, resulting in a slab with two vicinal surfaces. As the strain rate of these simulations was rather high

due to the limits of the simulation runtime, a study at lower deformation rates would be of value. In addition, these simulations were performed at a relatively low temperature of 10 K, at which diffusion processes are suppressed. An additional study at room temperatures would be beneficial and would avail itself better to any comparisons with experiments.

Typical experiments involving thin metallic films include substrates onto which the metallic thin films are grown, and the focus of the investigation is invariably on the substrate-film interfaces. This is understandable, especially in the cases which rely on the difference in thermal coefficients between the materials to induce the deformation, since those are the cases in which strains are highest at the substrate-film interfaces. We have found that our results align better with experiments on miniaturized tensile tests, such as those performed by Kiener *et al.* [71] on Cu single crystal substrates. For instance, we have found a striking resemblance in the deformation mechanism of the rods cut from a copper single crystal using a diamond wire saw and further machined with FIB (Focused Ion Beam), in a way so that the (-2 3 4) crystal direction was aligned with the length axis of the samples, shown in Kiener *et al.* [71], to the deformation mechanism of Cu(1 1 19) deformed in tension in our study. In their experiments only one slip direction was active for the strains of up to 22.6 %.

# Appendix A

# LAMMPS Script: Minimization

**Algorithm A.1:** A sample LAMMPS script for the energy minimization.

```
variable element index Cu
variable latparam equal 3.6149
variable psty index eam/alloy
variable potential index ../Cu_mishin1.eam
variable Lx equal 5.0000
variable Ly equal 18.1500
variable Lz equal 34.5715

units metal
boundary p p m
atom_style atomic
lattice fcc $latparam orient z 1 1 19 orient x 1 -1 0 orient y 19 19 -2
lattice box block 0 $Lx 0 $Ly 0 $Lz
create_box 1 box
create_atoms 1 region box
lattice frozen block INF INF INF INF INF 4.0
group frozen region frozen
lattice edge block INF INF INF INF 30.0 INF
group edge region edge
delete_atoms group edge
timestep 0.01
pair_style $psty
pair_coeff * * $potential $element

dump pre all custom 1 pre.qmin.dump id type x y z
run 0
undump pre
fix f1 frozen setforce 0.0 0.0 0.0
min_style quickmin
minimize 1.0e-35 1.0e-35 40000 40000
dump post all custom 1 post.qmin.dump id type x y z
run 0
```

# Appendix B

# LAMMPS Script: Equilibration

**Algorithm B.1:** A sample LAMMPS script for equilibration to 10 K.

```
variable element index Cu
variable latparam equal 3.6149
variable psty index eam/alloy
variable potential index ../Cu_mishin1.eam
variable Lx equal sqrt(2)*$latparam*30/5.11224
variable Ly equal sqrt(726)*$latparam*2/5.36646
variable Lz equal 40.0

units metal
boundary p p m
atom_style atomic
lattice fcc $latparam orient z 1 1 19 orient x 1 -1 0 orient y 19 19 -2
lattice box block 0 $Lx 0 $Ly 0 $Lz
create_box 1 box
create_atoms 1 region box
lattice edge block INF INF INF INF 30.0 INF
group edge region edge
delete_atoms group edge
pair_style $psty
pair_coeff * * $potential $element

timestep 0.001
velocity all create 10 12345 mom yes rot no
fix NPT all npt temp 10 10 1 x 0 0 1 y 0 0 1 drag 2
run 50000
unfix NPT
write_restart equilibrated.10K.res
```

# Appendix C

# LAMMPS Script: Deformation

**Algorithm C.1:** A sample LAMMPS script for simulations of deformation.

```
variable element index Cu
variable latparam equal 3.6149
variable psty index eam/alloy
variable potential index ../Cu_mishin1.eam

read_restart equilibrated.10K.res

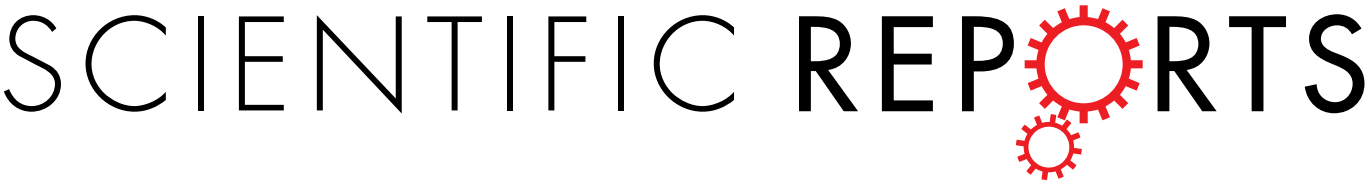
lattice fcc $latparam orient z 1 1 19 orient x 1 -1 0 orient y 19 19 -2
lattice frozen block INF INF INF INF INF 2.95
group frozen region frozen
lattice dynamic block INF INF INF INF 2.99 INF
group dynamic region dynamic
change_box all z final 0 55
pair_style $psty
pair_coeff * * $potential $element

variable L0 equal "ly"
print "Initial Length, L0: $L0"

fix NPT dynamic npt temp 10 10 1 x 0 0 1 drag 1
run 0
variable srate equal -2.5e9/1.0e12
fix compression all deform 1 y erate $srate units box remap x
variable strain equal "(ly - v_L0)/v_L0"
variable p1 equal "v_strain"
variable p2 equal "-pxx/10000"
variable p3 equal "-pyy/10000"
variable p4 equal "-pzz/10000"
fix output-system all print 50 "$p1 $p2 $p3 $p4" file compression.txt screen no
dump output-atoms all custom 250 compression.*.dump type xs ys zs id fx fy fz
run 50000
```

# Appendix D

# Article: A comparison of the uniaxial deformation of copper and nickel (1 1 19) surfaces: a molecular dynamics study



OPEN

# A comparison of the uniaxial deformation of copper and nickel (1 1 19) surfaces: a molecular dynamics study

Received: 26 October 2016
Accepted: 03 January 2017
Published: 07 February 2017

Nuša Pukšič[1,2], Monika Jenko[1,2], Matjaž Godec[1] & Paul J. McGuiness[1,2]

**While a lot is known about the deformation of metallic surfaces from experiments, elasticity theory and simulations, this investigation represents the first molecular-dynamics-based simulation of uniaxial deformation for the vicinal surfaces in a comparison of copper and nickel. These vicinal surfaces are composed of terraces divided by equidistant, mono-atomic steps. The periodicity of vicinals makes them good candidates for the study of the surface steps' influences on surface dynamics. The simulations of tensile and compressive uniaxial deformations were performed for the (1 1 19) vicinal surfaces. Since the steps on the surfaces serve as stress concentrators, the first defects were expected to nucleate here. In the case of copper, this was found to be the case. In the case of nickel, however, dislocations nucleated beneath the near-surface layer affected by the displacement field generated by the steps. Slip was hindered at the surface step by the vortex in the displacement field. The differences in the deformation mechanisms for the Ni(1 1 19) and Cu(1 1 19) surfaces can be linked to the differences in their displacement fields. This could lead to novel bottom-up approaches to the nanostructuring of surfaces using strain.**

In the past 20 years investigations of stress and strain effects in the field of surface physics have become increasingly important as the manufacture of nanoscale materials and devices has become more widespread, leading to studies based on a combination of theoretical, computational and experimental investigations[1]. As a result, the definitions of surface stress and surface strain that allow for numerical thermodynamic studies based on atomistic models have now been established, and elastically mediated interactions between various surface defects such as "steps" and "islands" have been described. It is clear that the displacement fields induced by these surface defects can profoundly affect the morphology of the surface. For example, in homo- or hetero-epitaxial growth, steps on a surface can act as nucleation centres or decrease the diffusion of adsorbed species due to the Ehrlich–Schwoebel barrier; in catalytic reactions stepped surfaces often have a different catalytic activity to that of flat surfaces[2–7]. Controlled deformation also appears to be a potential tool for the self-organization of surfaces, applicable in a bottom-up approach to the nanostructuring of materials.

Elasticity also provides pressure maps that can help to predict the stress release resulting from atomic rearrangements[1]; however, on the subject of vicinal surfaces under an externally applied stress the data from both experiments and simulations is scarce. These vicinal surfaces are defined by terraces divided by equidistant, monoatomic steps, and can be exposed by cutting a crystal at a small angle to one of the low-index planes. The elastic fields that the steps induce in the crystal reach into the bulk and therefore influence the mechanical properties of the surface[1,2,8–11].

Experiments on the nanoscale can be very time consuming and costly, requiring expensive equipment, particularly sensors; however, they confirm an array of unusual mechanical properties of nanoscale materials[12]. This serves as a motivation to use atomistic simulations in order to better understand the deformation mechanisms on the nanoscale. In previous studies of the mechanical properties of nanocrystalline materials and thin films by molecular statics and dynamics, most of the research was centered on the influence of phase and grain boundaries on the response of the material to an external load or deformation. And when molecular dynamics simulations

[1]Institute of Metals and Technology, Physics and Chemistry of Materials, Ljubljana, 1000, Slovenia. [2]Jožef Stefan International Postgraduate School, Ljubljana, 1000, Slovenia. Correspondence and requests for materials should be addressed to N.P. (email: nusa.puksic@imt.si)

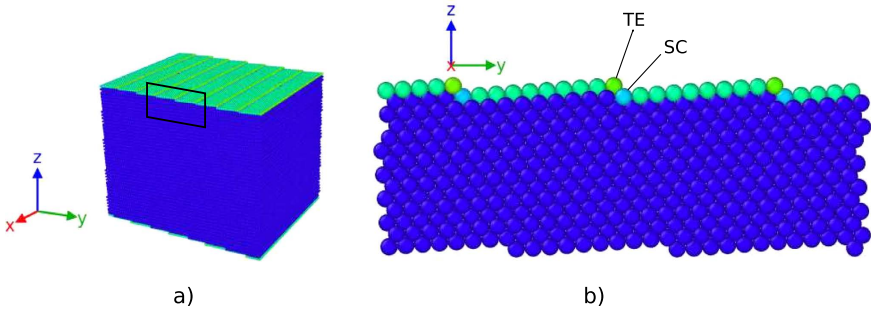



**Figure 1. Two-dimensional schematic of a (1 1 19) surface.** The terrace edge (TE) and step corner (SC) atoms are marked. The width of the terraces is 10 atomic rows. Orientation of the terraces is (001). The (1 1 19) and (19 19 $\bar{2}$) directions correspond to the **z** and **y** simulation box axes. The **y** direction is also the direction of the applied strain.

of the plastic deformation of nanocrystalline materials are considered, the focus is mainly on the generation of dislocations at the grain boundaries and the effectiveness of the grain boundaries in slowing the rate of plastic deformation[13–17].

Nano-indentation studies focus on dislocation nucleation beneath the indenter. The stress that is applied via the frictionless rigid indenter is non-uniform, but it can lead to homogeneous defect nucleation in a perfect crystal. The substrates are thin films[18–20], with controlled impurities, i.e., vacancies[21], voids[22], grain boundaries[23] and steps[24–27], added in some cases.

As nanowires have a large surface-to-bulk ratio, the most comprehensive studies of the influence of free surfaces on the mechanical properties of metallic materials using molecular dynamics were made with samples of nanowires[28–32]. For instance, in nanowires, the orientation of the surface can influence which deformations are energetically favorable, overriding the crystallographically preferred deformation mechanisms[31].

In this study molecular dynamics simulations of copper and nickel (1 1 19) vicinal surfaces under an externally applied uniaxial strain were performed and the beginning of plastic deformation was studied in order to determine the stability of the surface steps during deformation and their influence on the deformation mechanisms. The (1 1 19) surfaces were chosen because the steps on this surface, vicinal to the (1 0 0) nominal surface, are dense, and yet the distance between the steps is large enough to ensure that the interaction between the steps is weak: the relaxations of the step edge atoms are only slightly modified by the presence of the other steps[2].

## Results

A two-dimensional schematic of a (1 1 19) surface is shown in Fig. 1. These vicinal surfaces are composed of (001)-oriented terraces divided by equidistant, monoatomic steps with (111) microfacets. There are 10 rows of atoms per terrace. The terrace edge (TE) and step corner (SC) atoms are marked.

**Displacement fields.** The steps on the surface of a metallic material play a role in the atomic arrangement of the surface layers. Near-surface atoms are displaced from their bulk positions to accommodate the lack of neighbours at the surface. In the case of the vicinal surfaces this minimal energy arrangement of atoms leads to a complex displacement field, stretching several layers into the bulk specific for each surface orientation and material[2,8].

Although the displacement fields have been studied for a range of metals and surface orientations, their influence on the deformation mechanisms of the surfaces has never been investigated before. We have compared the displacement fields of Ni(1 1 19) and Cu(1 1 19) surfaces with their deformation mechanisms to investigate whether any influence of the displacement fields on the deformation mechanisms could be discerned.

The displacement fields for the Ni(1 1 19) and Cu(1 1 19) surfaces are shown in Fig. 2. Dots denote the atoms and arrows show their displacements from the bulk positions (multiplied by 100 for clarity). The grey lines trace the surface atoms. The step height is slightly reduced by the displacements, as TE atoms are displaced towards the bulk and SC atoms are displaced outwards.

In the case of nickel (Fig. 2a), some of the terrace atoms are displaced towards the bulk and some away from the bulk, with a turning point in the middle of the terraces, where the displacements are minimal. The TE and SC atoms are displaced the most. The magnitudes of the displacements of the TE and SC atoms are 0.007 nm and 0.005 nm, which equal 1.9% and 1.3% of the lattice parameter, respectively. The displacements form vortices that are located near the steps.

In the case of copper (Fig. 2b), all the terrace atoms are displaced towards the bulk and the step corner atoms are displaced outwards. The TE and SC atoms are displaced the most. The magnitudes of the displacements of the TE and SC atoms are 0.013 nm and 0.004 nm, which equal 3.6% and 1.2% of the lattice parameter, respectively. The displacements form vortices that are located underneath the terraces.

In the case of nickel, the vortices can be thought of as straddling the (111) plane intersecting with the step, whereas in the case of copper the vortices can be seen as contained between two (111) planes intersecting with adjacent steps. In the view presented in Fig. 2, the vortices in nickel are rotated counter-clockwise and the vortices in copper clockwise.

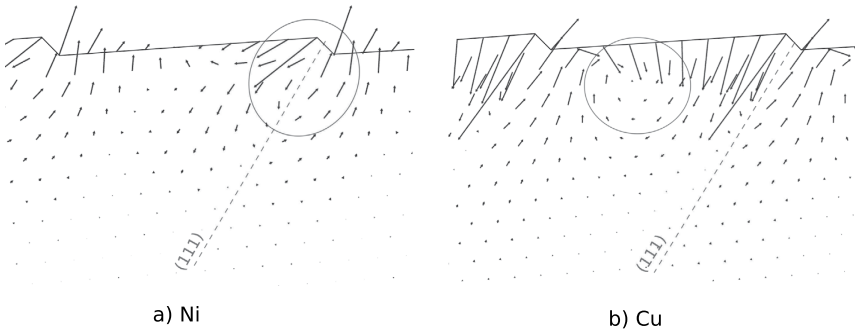



**Figure 2. Displacement fields of Ni(1 1 19) and Cu(1 1 19) surfaces are shown.** Arrows show the displacements of the atoms from their bulk positions (multiplied by 100 for clarity). Surface atoms are traced by grey lines. Dashed lines mark the (111) planes. The general regions of the displacement vortices are circled. In the case of the Ni(1 1 19) surface (**a**) some of the terrace atoms are displaced towards the bulk and others away from the bulk. The step corner and terrace edge atoms are displaced the most and the atoms in the middle of the terrace are displaced the least. The vortex is centered on the (111) plane marked with a dashed line. In the case of the Cu(1 1 19) surface (**b**) all the terrace atoms are displaced towards the bulk, whereas the step corner atom is displaced outwards. The displacements form a vortex underneath the terrace.

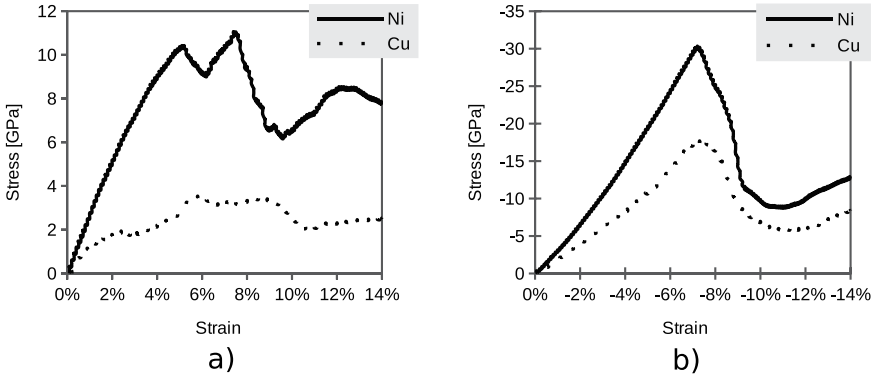



**Figure 3. Stress-strain curves for Ni and Cu(1 1 19) oriented thin films deformed in tension and in compression.** Both materials exhibit a yield-stress asymmetry. (**a**) In the case of Ni, the peaks at 5.5% and 7.5% strains indicate the activation of the first and the second slip system. For copper, the peak at 6.0% strain indicates the activation of the first slip system, and the peak at 9.3% strain the beginning of twinning. (**b**) In the case of compression, multiple deformation mechanisms are activated at once at −7.2% strain for nickel and at −7.1% strain for copper.

**Results of deformation simulations.** Copper and nickel both have a face-centered cubic (fcc) lattice. In fcc crystals the close-packed planes and directions are preferred for slip. However, which slip systems are the most favorable is additionally determined by the direction of the strain. In our case the strain direction was (19 19 $\bar{2}$); therefore, the primary slip systems are $\{111\}\langle 0\bar{1}1\rangle$ and $\{111\}\langle\bar{1}01\rangle$.

As both materials have low stacking-fault energy, both are expected to deform by partial dislocations and twinning.

*Stress-strain curves.* The stress-strain curves for tensile deformation are shown in Fig. 3a, and those for compression are shown in Fig. 3b. Both materials exhibit a significant yield-stress asymmetry, with the yield stress being higher in compression than in tension. Both materials exhibit multiple peaks in the stress-strain curves in tensile deformation, Fig. 3a, and a single pronounced peak in compressive deformation, Fig. 3b. For nickel in tension, the peaks at 5.5% and 7.5% strains indicate the activation of the first and the second slip system. For copper in tension, the peak at 6.0% strain indicates the activation of the first slip system, and the peak at 9.3% strain the beginning of the twinning. In the case of compression, multiple deformation mechanisms are activated at once at −7.2% strain for nickel and at −7.1% strain for copper, leading to a larger and steeper drop in stress compared to the case of tensile deformation.

*Tensile deformation.* In the case of Ni, Fig. 4, the first slip system is activated at the strain of 5.5%, when dislocations nucleate in the bulk, 8–10 layers below the surface, Fig. 4a. Stacking faults first climb towards the surface, where they intersect with the terraces and not with the steps. Slip introduces new steps on the surface, Fig. 4b. Stacking faults then continue growing into the bulk of the sample by dislocation climb in the opposite direction

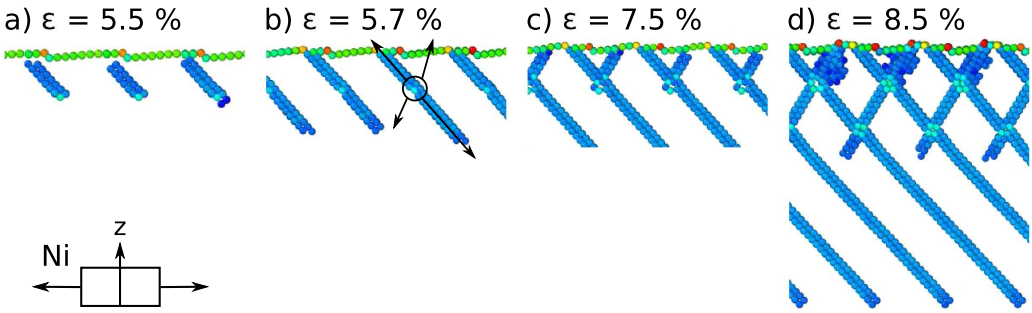



**Figure 4. Deformation evolution of Ni(1 1 19) deformed in tension.** (**a**) Dislocations nucleate in the bulk 8–10 layers underneath the surface. (**b**) The active slip system is perpendicular to the one expected and leads to the formation of additional steps on the surface. (**c**) After the stacking faults reach the bottom of the sample, the next slip system is activated. Partial dislocations nucleate at the same nucleation sites in the bulk, grow towards the surface and then into the bulk. (**d**) At strains above 8.0% a set of stacking faults begins to grow into twins. Atoms comprising surfaces and stacking faults are shown, others ($CS < 2$) are removed for clarity.

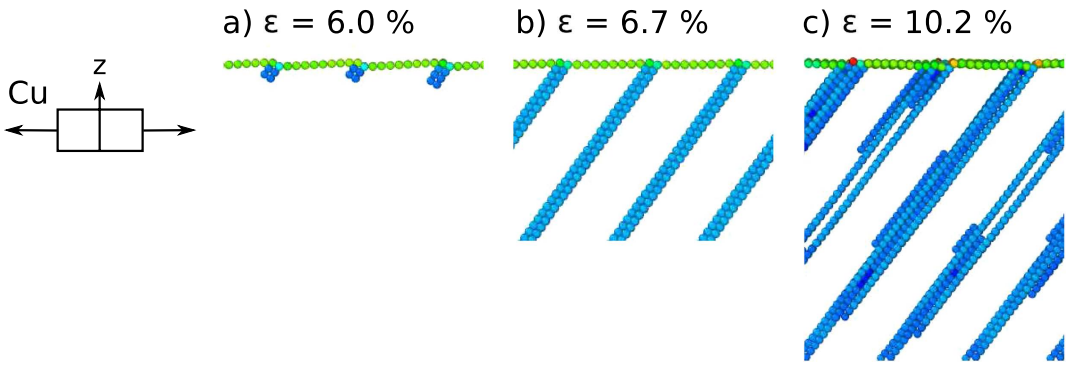



**Figure 5. Deformation evolution of Cu(1 1 19) deformed in tension.** (**a**) Stacking faults nucleate at the surface, (**b**) growing to the bottom of the sample. (**c**) The perpendicular slip system is not activated, instead deformation mechanism switches to twinning. Atoms comprising surfaces and stacking faults are shown, others ($CS < 2$) are removed for clarity.

in the same slip plane. When the stacking faults reach the layer of fixed atoms at the bottom of the sample, the slip system with the perpendicular slip direction is activated, at the strain of 7.5%, Fig. 4c. These stacking faults originate at the same nucleation sites as the previous set. Another set of steps is introduced at the surface and a crosswise pattern of stacking faults emerges in the bulk, Fig. 4d. In addition, at strains above 8.0% a set of near-surface stacking faults grow into twins.

In the case of Cu, Fig. 5, Shockley partial dislocations nucleate at the steps on the surface and climb into the bulk, creating stacking faults reaching from the surface ever deeper into the bulk with increasing strain, Fig. 5a,b. Slip reduces the height of the steps and leads to a flattening-out of the surface. No trailing partials detach from the surface. When the stacking faults reach the bottom of the sample, Fig. 5c, stacking faults grow into twins.

In comparison, dislocations nucleate at the surface steps in copper and in the bulk in nickel. The steps on the surface act as stress concentrators and are the expected nucleation sites. In both metals the dislocations nucleate and travel evenly along the whole length of the simulated samples in the **x** direction, parallel to the direction of the steps. In addition, the primary slip system in copper is the one expected to be activated in tensile deformation, leading to a flattening-out of the surface. In the case of nickel the primary slip system is perpendicular to the one expected and leads to the formation of additional steps on the surface. Both materials start twinning at strains above 8.0%.

*Compressive deformation.* In the case of nickel, dislocations nucleate at the steps and in the bulk 8–10 layers beneath the surface (a). The bulk nucleation sites in nickel are the same as in the case of tensile deformation. Two perpendicular slip systems are activated at once. A dense mesh of dislocations forms. Due to the lack of space available, the dislocations that have nucleated at the surface climb along the terraces instead of growing into the bulk. In the case of copper, only one slip system is activated (b). As expected, the slip plane is perpendicular to the one active in tensile deformation. After the dislocations reach the bottom of the sample, deformation twinning is observed in the bulk (d). The slip system perpendicular to the primary one is not activated. In comparison, the bulk nucleation sites are present in nickel but not in copper and two slip systems are active in nickel, whereas only one is active in copper. In addition, deformation twinning is observed in copper but not in nickel.

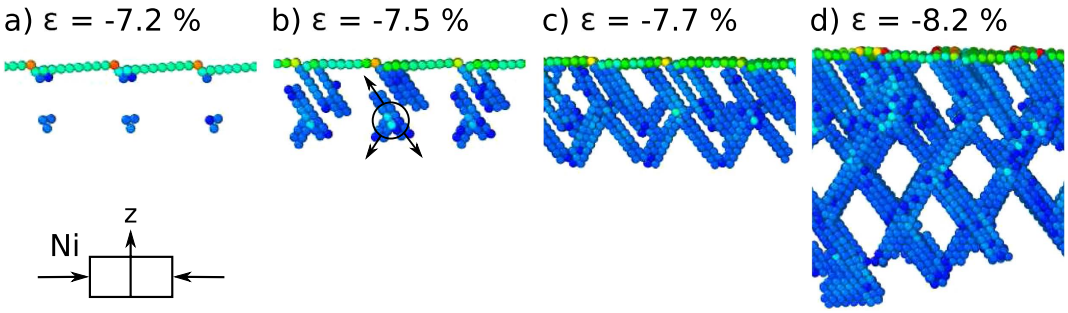



**Figure 6. Deformation evolution of Ni(1 1 19) deformed in compression.** (**a**) Dislocations nucleate in the bulk 8–10 layers underneath the surface as well as at the steps. (**b**) From the nucleation sites in the bulk, stacking faults grow in three directions, utilizing two slip planes. Stacking faults originating at the steps switch to twinning at the strain of −7.3%. (**c**) Stacking faults and twins connect. (**d**) Defects grow into the bulk evenly along both active slip systems. Atoms comprising surfaces and stacking faults are shown, others ($CS < 2$) are removed for clarity.

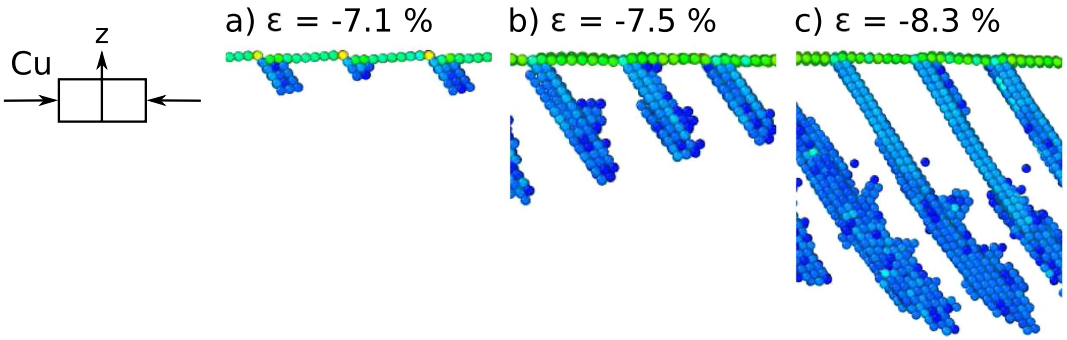



**Figure 7. Deformation evolution of Cu(1 1 19) deformed in compression.** (**a**) Defects nucleate at the steps on the surface. (**b**) Parallel twins grow into the bulk along the direction of the active slip system. (**c**) Twins remain the prevailing deformation mechanism, the perpendicular slip system is not activated. Atoms comprising surfaces and stacking faults are shown, others ($CS < 2$) are removed for clarity.

In the case of nickel deformed in compression, Fig. 6, dislocations nucleate at the surface and in the bulk, Fig. 6a. The deformation mechanism is a combination of slip and twinning. One set of partial dislocations nucleates at the edges of the terraces. Hindered by the dislocations nucleating in the bulk, these partial dislocations switch to twinning instead of climbing deeper into the bulk, Fig. 6b. The partial dislocations nucleating in the bulk, 8–10 layers below the surface, grow along three slip directions on two slip planes, Fig. 6b. The placement of the nucleation sites is the same as in the case of nickel deformed in tension. A complex crosswise pattern of dislocations and twins emerges, Fig. 6c, and continues to grow evenly into the bulk along both active slip systems, Fig. 6d. Compared to tensile deformation, where twinning emerges at strains higher than 8.0%, in tension twinning emerges sooner at a strain of −7.5%.

In the case of copper deformed in compression, dislocations nucleate at the edges of the terraces, Fig. 7. The deformation mechanism is a combination of slip and twinning. The slip direction is perpendicular to the one active in tensile deformation. Slip again flattens out the surface. Trailing partial dislocations nucleate at the surface in some places. The slip system perpendicular to the primary one is not activated in this case. Twinning is the prevailing deformation mechanism.

In comparison, the bulk nucleation sites are observed in nickel, but not in copper. Two perpendicular slip system are active in nickel, while only one is active in copper. Deformation twinning occurs in both materials, starting at strains of −7.1% for copper and −7.5% for nickel.

## Discussion

We have investigated the plastic deformation of the (1 1 19) vicinal surfaces of copper and nickel thin films deformed in tension and in compression with a uniaxial engineering strain at a rate of 2.5% $ps^{-1}$. Although the metals are very similar, we have found very significant differences in their plastic deformation mechanisms.

The low temperature and the high strain rate of the simulations influence the deformation mechanisms. At low temperatures the diffusion-controlled processes are suppressed and the main deformation mechanism is slip[33]. At high strain rates the dislocation mobility is lowered, giving precedence to dislocation generation[33]. Low temperatures and high strain rates can also lead the deformation mechanisms to transition from slip to deformation twinning[33].

In the size range of our simulations, i.e., approximately 10 nm, partial dislocations are generally preferred over full dislocations as the deformation mechanisms for metallic materials[12,34].

As both metals have low stacking-fault energies, the expected deformation mechanisms were by partial dislocation slip and by twinning. As the stacking fault energy and the predicted twinning stress of nickel are higher than that of copper, a preference of twinning over slip is expected to be more pronounced in copper[35]. We found that to be the case in tension and in compression. In addition, nickel is able to endure exceptional elastic lattice distortion[36].

Multiple criteria are met, for both materials, predicting partial dislocations and twinning as the main deformation mechanisms, and both are observed in all the cases, superseding full dislocation nucleation.

The arrays of steps on the (1 1 19) vicinal surfaces influence the deformation mechanisms of both metals. The regularity of the steps is translated into the regularity of the stacking faults that form in all cases.

In the case of copper, steps on the surface serve as nucleation points and both tensile and compressive strains lead to a flattening out of the surface steps. This is as expected from the theory of elasticity.

In the case of nickel, the point of dislocation nucleation lies 8–10 layers underneath the surface instead of at the surface. The nucleation sites are the same in tensile and compressive deformation, although in compression the dislocations nucleate at the surface steps as well. The defect nucleation sites buried below the surface are unexpected, since the steps are known as the stress-concentration points. The defect nucleation sites lie beneath the terraces just outside the region affected by the displacement field. In addition, the primary slip system activated in nickel deformed in tension is perpendicular to the primary system activated in copper.

In the case of copper deformed in tension, slip occurs in the (111) plane that delineates two vortices underneath adjacent terraces. The atoms involved slip in the direction of their displacements. In the case of nickel, this process is hindered by the presence of the vortices. Nucleation points are shifted into the bulk beneath the displacement field. Slip occurs in the direction in which crystal symmetry is disturbed the most by the displacement field.

In the case of nickel deformed in compression, nucleation points in the bulk and at the steps are activated. The area of the vortex is again initially avoided, then cut through by the stacking fault originating in the bulk, as was the case in tensile deformation. The nucleation of stacking faults at the steps is in this case not restricted by the displacement field.

Zimmerman *et al.*[24] studied Au(111) surfaces with single monoatomic steps at 0 K and found that the step had no long-range influence on the deformation mechanism, and only when the indenter came into physical contact with the step, did the deformation mechanism beneath the indenter switch from dislocation emission from the surface to slip aligned with the step. We also found a preference for slip aligned with the steps.

Shan *et al.*[25] performed a similar study of nano-indentation on thin copper films and also found no long-range effects of the step. In addition, they found that in the case when the indenter came into contact with the step, there was a significant difference in the strength of the first dislocation emission. Apart from that, it was not made clear whether any change in the deformation mechanism was observed.

Lu *et al.*[26,27] investigated the effects of surface steps on nano-indentation in Al. They found that the shear stress resulting from the step influences the choice of the active slip systems and lowers the threshold for plastic deformation.

To date no such investigations were performed for nickel vicinal surfaces.

As the surfaces were first to deform in our study, we are in agreement with Shan *et al.*[25] and Lu *et al.*[26,27], that the steps influence the choice of the active slip system and have a lower threshold for plastic deformation compared to the bulk.

We have observed distinct deformation mechanisms depending on the sign of the strain. Both materials were similarly affected, as a switch to a different deformation mechanism occurred in tensile deformation at higher strains, while multiple deformation mechanisms were activated at once in compression. Experiments show there are cases of different deformation mechanisms depending on the sign of strain[37] as well as switching of deformation mechanisms at higher strains[37].

## Conclusions

We conclude that the displacement fields of vicinal surfaces play a role in their deformation mechanisms. As expected, the regularity of the steps on the surface translates into the regularity of the dislocations and stacking faults that form beneath the surface. While all the dislocations were expected to nucleate at the steps, this was the case for copper, but not for nickel. In tensile deformation, the displacement field in the vicinity of the step in nickel seems to prevent slip in the (111) plane, which is the first to activate in the case of copper. In compressive deformation, the nucleation points beneath the surface in nickel are activated in addition to the ones at the surface that follow the expected pattern, as evidenced in copper.

As the displacement fields are orientation dependent, differences in the deformation mechanism might also arise for other vicinal surfaces.

As was shown for nickel, a patterned surface can be achieved, which has repercussions for bottom-up approaches to the nano-structuring of surfaces using strain. A high density of steps can be achieved, which could be used for templates, in catalysis[3–7,38] or for orienting or growing nanotubes or nanowires[39,40].

## Methods

Copper and nickel thin films of 10 nm thickness with (1 1 19) surface orientation were simulated. The simulations of the tensile and compressive uniaxial deformations were performed at 10 K, applying engineering strain at a strain rate of $\pm 2.5\%\ ps^{-1}$. The strain direction was (19 19 $\bar{2}$), perpendicular to the steps.

Copper and nickel single-crystal substrates were used in the molecular dynamics simulations, which were carried out using the LAMMPS Molecular Dynamics Simulator[41] and the following EAM potentials: for copper by Mishin *et al.*[42] and for nickel by Sheng *et al.*[43].

The axes of the simulation boxes were $\mathbf{x} = (1\ \bar{1}\ 0)$, $\mathbf{y} = (19\ 19\ \bar{2})$ and $\mathbf{z} = (1\ 1\ 19)$.

The boundaries of the simulation boxes were periodic in the **x** and **y** directions and fixed in the **z** direction.

In the **y** direction the size of the simulation box was subject to requirements for periodicity of the terraces and steps for vicinal surfaces. The number of steps and terraces included was 8.

In the **z** direction the simulated films were bound by a free surface at the top and by a layer of fixed atoms at the bottom to prevent the loss of atoms at the border of the simulation box and to simulate defect-free bulk. The thickness of this frozen layer was 1.2 nm. These atoms were fixed at the positions they had when equilibrated to 10 K and were remapped at every deformation of the simulation box. All the forces acting on these atoms were otherwise reset to zero.

Physical dimensions of the simulated samples were as follows. The lattice parameter of copper was 0.36149 nm and the size of the simulated sample was 20.4 nm × 19.5 nm × 11.2 nm. The lattice parameter of nickel was 0.35200 nm and the size of the simulated sample was 19.9 nm × 19.0 nm × 11.2 nm.

Damped dynamics[44] were used to find the minimum energy states of the surfaces at 0 K. Afterwards, the substrates were equilibrated to 10 K. Then, to simulate engineering compressive and tensile strains, the simulation box was deformed in the **y** direction in increments of 0.5% with 200 fs periods of equilibration in-between, resulting in the overall strain rate of 2.5% $ps^{-1}$. The stress in the **x** direction was kept to zero.

OVITO[45] was used for visualization and analysis of the simulation data.

The centro-symmetry parameter is used to identify dislocations and stacking faults in the simulations. In solid-state systems the centro-symmetry parameter is a useful measure of the local lattice disorder around an atom and can be used to characterize whether the atom is part of a perfect lattice, a local defect (e.g., a dislocation or stacking fault), or at a surface. This parameter is computed using the following formula[46]

$$CS = \sum_{i=1}^{N/2} |\mathbf{R}_i + \mathbf{R}_{i+N/2}|^2 \tag{1}$$

where the $N$ nearest neighbours of each atom are identified and $\mathbf{R}_i$ and $\mathbf{R}_{i+N/2}$ are vectors from the central atom to a particular pair of nearest neighbors. For an fcc lattice $N$ is 12. For an atom on a lattice site, surrounded by atoms on a perfect lattice, the centro-symmetry parameter will be 0. It will be near 0 for small thermal perturbations of a perfect lattice. If a point defect exists, the symmetry is broken, and the parameter will be a larger positive value. An atom at a surface will have a large positive parameter.

Primary slip systems are defined as having the largest Schmid factors for the given strain direction, which are calculated as $m = (\mathbf{s_P} \cdot \mathbf{y})(\mathbf{s_D} \cdot \mathbf{y})$, where $\mathbf{s_P}$, $\mathbf{s_D}$ and **y** denote the slip-plane normal, the slip direction and the strain direction.

## References


1. Muller, P. Elastic effects on surface physics. *Surface Science Reports* **54,** 157–258 (2004).
2. Prévot, G., Cohen, C., Schmaus, D., Hecquet, P. & Salanon, B. Temperature dependence of the atomic relaxations and vibrations on a stepped surface: a molecular dynamics study of Cu (1, 1, 19). *Surface science* **506,** 272–286 (2002).
3. Ferre-Vilaplana, A., Gisbert, R. & Herrero, E. On the electrochemical properties of platinum stepped surfaces vicinal to the (100) pole. a computational study. *Electrochimica Acta* **125,** 666–673 (2014).
4. Xu, J., Abd-El-Latif, A.-E.-A. A., Chen, Y.-X. & Baltruschat, H. Electrodeposition of silver on stepped platinum electrode surfaces with (1 0 0)-oriented terraces: Generation of confined reaction sites. *Journal of Electroanalytical Chemistry* **716,** 93–100, Special Issue in Honour of Kingo Itaya (2014).
5. Godowski, P. J. & Onsgaard, J. Adsorption of NO on potassium-modified Cu (100) vicinal surfaces. *Vacuum* **94,** 6–13 (2013).
6. Gómez-Marín, A. M. & Feliu, J. M. Thermodynamic properties of hydrogen–water adsorption at terraces and steps of Pt(111) vicinal surface electrodes. *Surface Science* **646,** 269–281, Surface science for heterogeneous catalysis, a special issue in Honour of Richard Lambert (2016).
7. Rodriguez, P., García-Aráez, N., Herrero, E. & Feliu, J. New insight on the behavior of the irreversible adsorption and underpotential deposition of thallium on platinum (111) and vicinal surfaces in acid electrolytes. *Electrochimica Acta* **151,** 319–325 (2015).
8. Prévot, G. & Croset, B. Elastic relaxations and interactions on metallic vicinal surfaces: testing the dipole model. *Physical Review B* **74,** 235410 (2006).
9. Yang, J., Hu, W., Deng, H. & Zhao, D. Temperature dependence of atomic relaxation and vibrations for the vicinal Ni (9 7 7) surface: a molecular dynamics study. *Surface Science* **572,** 439–448 (2004).
10. Yıldırım, H. & Durukanoğlu, S. Structural relaxations of cu vicinals. *Surface Science* **557,** 190–200 (2004).
11. Spišák, D. Structure and energetics of Cu(1 0 0) vicinal surfaces. *Surface Science* **489,** 151–160 (2001).
12. Wang, L., Zhang, Z. & Han, X. *In situ* experimental mechanics of nanomaterials at the atomic scale. *NPG Asia Materials* e40 (2013).
13. Spearot, D., Capolungo, L., Qu, J. & Cherkaoui, M. On the elastic tensile deformation of ⟨100⟩ bicrystal interfaces in copper. *Computational Materials Science* **42,** 57–67 (2008).
14. Chassagne, M., Legros, M. & Rodney, D. Atomic-scale simulation of screw dislocation/coherent twin boundary interaction in Al, Au, Cu and Ni. *Acta Materialia* **59,** 1456–1463 (2011).
15. Bachurin, D., Weygand, D. & Gumbsch, P. Dislocation–grain boundary interaction in ⟨111⟩ textured thin metal films. *Acta Materialia* **58,** 5232–5241 (2010).
16. You, Z. *et al.* Plastic anisotropy and associated deformation mechanisms in nanotwinned metals. *Acta Materialia* **61,** 217–227 (2013).
17. Shan, Z. *et al.* Grain boundary-mediated plasticity in nanocrystalline nickel. *Science* **305,** 654–657 (2004).
18. Choi, Y., Van Vliet, K. J., Li, J. & Suresh, S. Size effects on the onset of plastic deformation during nanoindentation of thin films and patterned lines. *Journal of Applied Physics* **94,** 6050 (2003).
19. Zhu, T. Predictive modeling of nanoindentation-induced homogeneous dislocation nucleation in copper. *Journal of the Mechanics and Physics of Solids* **52,** 691–724 (2004).
20. Lilleodden, E., Zimmerman, J., Foiles, S. & Nix, W. Atomistic simulations of elastic deformation and dislocation nucleation during nanoindentation. *Journal of the Mechanics and Physics of Solids* **51,** 901–920 (2003).

21. Salehinia, I. & Medyanik, S. N. Effects of Vacancies on the Onset of Plasticity in Metals—An Atomistic Simulation Study. *Metallurgical and Materials Transactions A* **42,** 3868–3874 (2011).
22. Tan, C.-M. & Jeng, Y.-R. Computer simulations of nanoindentation on Cu (111) with a void. *International Journal of Solids and Structures* **46,** 1884–1889 (2009).
23. Jang, H. & Farkas, D. Interaction of lattice dislocations with a grain boundary during nanoindentation simulation. *Materials Letters* **61,** 868–871 (2007).
24. Zimmerman, J. A., Kelchner, C. L., Klein, P. A., Hamilton, J. C. & Foiles, S. M. Surface step effects on nanoindentation. *Phys. Rev. Lett.* **87,** 165507 (2001).
25. Shan, D., Yuan, L. & Guo, B. Multiscale simulation of surface step effects on nanoindentation. *Materials Science and Engineering: A* **412,** 264–270 (2005).
26. Lu, H. & Ni, Y. Effect of surface step on nanoindentation of thin films by multiscale analysis. *Thin Solid Films* **520,** 4934–4940 (2012).
27. Lu, H., Ni, Y., Mei, J., Li, J. & Wang, H. Anisotropic plastic deformation beneath surface step during nanoindentation of FCC al by multiscale analysis. *Computational Materials Science* **58,** 192–200 (2012).
28. Huang, D., Zhang, Q. & Qiao, P. Molecular dynamics evaluation of strain rate and size effects on mechanical properties of FCC nickel nanowires. *Computational Materials Science* **50,** 903–910 (2011).
29. Setoodeh, A., Attariani, H. & Khosrownejad, M. Nickel nanowires under uniaxial loads: A molecular dynamics simulation study. *Computational Materials Science* **44,** 378–384 (2008).
30. Wen, Y.-H., Zhu, Z.-Z., Shao, G.-F. & Zhu, R.-Z. The uniaxial tensile deformation of Ni nanowire: atomic-scale computer simulations. *Physica E: Low-dimensional Systems and Nanostructures* **27,** 113–120 (2005).
31. Ma, F., Xu, K.-W. & Chu, P. K. Surface-induced structural transformation in nanowires. *Materials Science and Engineering: R: Reports* **74,** 173–209 (2013).
32. Park, H. S., Gall, K. & Zimmerman, J. A. Deformation of FCC nanowires by twinning and slip. *Journal of the Mechanics and Physics of Solids* **54,** 1862–1881 (2006).
33. Armstrong, R. W. & Walley, S. M. High strain rate properties of metals and alloys. *International Materials Reviews* 105–128 (2008).
34. Wang, L. *et al. In Situ* observation of dislocation behavior in nanometer grains. *Phys. Rev. Lett.* **105,** 135501 (2010).
35. Kibey, S., Liu, J., Johnson, D. & Sehitoglu, H. Predicting twinning stress in fcc metals: Linking twin-energy pathways to twin nucleation. *Acta Materialia* **55,** 6843–6851 (2007).
36. Wang, L. *et al. In situ* atomic-scale observation of continuous and reversible lattice deformation beyond the elastic limit. *Nature Communications* 2413 (2013).
37. Wang, L. *et al.* Deformation mechanisms of bent Si nanowires governed by the sign and magnitude of strain. *Applied Physics Letters* **108,** 151903 (2016).
38. Gellman, A. J., Baker, L. & Holsclaw, B. Xe adsorption site distributions on Pt(111), Pt(221) and Pt(531). *Surface Science* **646,** 83–89, Surface science for heterogeneous catalysis, a special issue in Honour of Richard Lambert (2016).
39. Zhang, X., Xie, D., Huang, G. & Sun, X.-H. Nanowires and nanoneedles nucleation on vicinal substrate. *Physica B: Condensed Matter* **456,** 78–81 (2015).
40. Spišák, D. & Hafner, J. Magnetism of monoatomic wires on vicinal surfaces. *Computational Materials Science* **27,** 138–150, E-MRS Symposium Spring Meeting - Symposium A: Atomic Scale Materials Design (2003).
41. Plimpton, S. Fast Parallel Algorithms for Short-Range Molecular Dynamics. *Journal of Computational Physics* 1–19, http://lammps.sandia.gov/ (1995).
42. Mishin, Y., Mehl, M., Papaconstantopoulos, D., Voter, A. & Kress, J. Structural stability and lattice defects in copper: Ab initio, tight-binding, and embedded-atom calculations. *Physical Review B* **63,** 224106 (2001).
43. Sheng, H. W., Kramer, M. J., Cadien, A., Fujita, T. & Chen, M. W. Highly optimized embedded-atom-method potentials for fourteen FCC metals. *Phys. Rev. B* **83,** 134118 (2011).
44. Sheppard, D., Terrell, R. & Henkelman, G. Optimization methods for finding minimum energy paths. *The Journal of chemical physics* **128,** 134106 (2008).
45. Stukowski, A. Visualization and analysis of atomistic simulation data with OVITO–the Open Visualization Tool. *Modelling and Simulation in Materials Science and Engineering* **18,** 015012 (2010).
46. Kelchner, C. L., Plimpton, S. J. & Hamilton, J. C. Dislocation nucleation and defect structure during surface indentation. *Physical Review B* **58,** 11085–11088 (1998).


## Acknowledgements

The authors acknowledge the financial support of the Slovenian Research Agency (ARRS). This study forms part of the research effort in Program Group P2-0132.

## Author Contributions

N.P., M.J. and M.G. conceived the simulations, N.P. conducted the simulations and analyzed the results, P.J.M. helped write the manuscript. All authors reviewed the manuscript.

## Additional Information

**Competing financial interests:** The authors declare no competing financial interests.

**How to cite this article**: Pukšič, N. *et al.* A comparison of the uniaxial deformation of copper and nickel (1 1 19) surfaces: a molecular dynamics study. *Sci. Rep.* **7**, 42234; doi: 10.1038/srep42234 (2017).

**Publisher's note:** Springer Nature remains neutral with regard to jurisdictional claims in published maps and institutional affiliations.

This work is licensed under a Creative Commons Attribution 4.0 International License. The images or other third party material in this article are included in the article's Creative Commons license, unless indicated otherwise in the credit line; if the material is not included under the Creative Commons license, users will need to obtain permission from the license holder to reproduce the material. To view a copy of this license, visit http://creativecommons.org/licenses/by/4.0/

© The Author(s) 2017

# Appendix E

# Article: Molecular dynamics simulations of plastic deformation of metallic surfaces

UDK 67.017:669.058:620.172.2
Original scientific article/Izvirni znanstveni članek

ISSN 1580-2949
MTAEC9, 51(1)153(2017)

# MOLECULAR DYNAMICS SIMULATIONS OF PLASTIC DEFORMATION OF METALLIC SURFACES

## SIMULACIJE PLASTIČNE DEFORMACIJE KOVINSKIH POVRŠIN Z METODO MOLEKULARNE DINAMIKE

**Nuša Pukšič[1,2], Monika Jenko[1,2], Matjaž Godec[1]**

[1]Institute of Metals and Technology, Lepi pot 11, Ljubljana, Slovenia
[2]Jožef Stefan International Postgraduate School, Jamova cesta 39, Ljubljana, Slovenia
nusa.puksic@imt.si

*Prejem rokopisa – received: 2016-12-12; sprejem za objavo – accepted for publication: 2016-12-23*

doi:10.17222/mit.2016.334

An understanding of the physical properties of a wide array of geometries is important in the quest for ever smaller and more fine-tuned devices and their parts. Surfaces play a key role in the deformation of nano-scale systems. Molecular dynamics simulations of compressive and tensile deformation were performed on nickel and copper thin films with (111), (9 9 11) and (10 10 8) surface orientations at 10 K. The (9 9 11) and (10 10 8) surfaces are vicinal to (111) and consist of a series of equidistant monoatomic steps. All the cases exhibit a yield stress asymmetry, with the yield stress being higher in compression than in tension. The near-surface region is the first to plastically deform and dislocations nucleate at the surface. The influence of the surface is most pronounced for the cases of the (10 10 8) surfaces deformed in compression, where parallel stacking faults nucleate at the steps on the surfaces in both materials, overriding the primary slip systems.

Keywords: molecular dynamics (MD), metallic surfaces, thin films, deformation

Dobro razumevanje mehanskih lastnosti široke palete geometrij je pomembno pri izboljšavah vedno manjših in zahtevnejših naprav in njihovih delov. Površine igrajo pomembno vlogo pri deformaciji sistemov na nano-skali. Z metodo molekularne dinamike smo raziskali deformacijo (111), (9 9 11) in (10 10 8) orientiranih nikljevih in bakrovih tankih filmov ob raztezanju in krčenju pri temperaturi 10 K. Površini (9 9 11) in (10 10 8) sta sosednji nominalni površini (111) in sta sestavljeni iz ekvidistantnih stopnic. Vse površine imajo asimetrično mejo plastičnosti, ki je višja pri stiskanju kot pri raztezanju. Območja tik pod površino se najprej deformirajo in dislokacije izvirajo na površinah. Vpliv površine je najbolj izrazit za primera orientacije (10 10 8) pri stiskanju, ko se oba materiala deformirata s serijo vzporednih napak zloga, ki izvirajo iz stopnic na površinah in, ki nadomestijo primarne drsne sisteme.

Ključne besede: molekularna dinamika (MD), kovinske površine, tanki filmi, deformacija

## 1 INTRODUCTION

Experiments at the nanoscale can be very time consuming and costly, in addition, they often turn out ambiguous due to lack of constraint on the thin foils examined. Such experiments also require expensive equipment and sensors, which further motivates us to use atomistic simulations to better understand deformation mechanisms at the nanoscale. Molecular dynamics (MD) simulations can serve as an effective tool for analysing dislocation nucleation mechanisms in metallic materials.[1–4]

Whereas the misorientation of adjacent grains determines the precise positioning of the atoms close to the boundaries, leading to diverse defect nucleation sites, the surface condition similarly influences the mechanical response of a material to external loads or deformation due to the relaxation of the topmost layers minimizing the surface energy and the adjacent free space into which the atoms can move.[5–8]

Vicinal surfaces, such as (10 10 8) and (9 9 11) investigated here, are produced by cutting a crystal close to a dense plane, and consist of terraces divided by equidistant monoatomic steps. When cutting or growing polycrystalline materials, such surfaces are unavoidable. As is the case with grain boundaries, the steps on the surface provide favourable nucleation sites for dislocations and stacking faults, key elements of plastic deformation. We show that deformation mechanisms in copper and nickel are influenced by the presence of steps at the surface.

## 2 EXPERIMENTAL PART

The simulations were performed on an array of substrates, with surface orientations (111), (9 9 11) and (10 10 8). The (9 9 11) and (10 10 8) surfaces are vicinal to (111) and consist of a series of equidistant monoatomic steps that have (001) and (-1-11) oriented microfacets, respectively.

Copper and nickel single crystal thin films of 10 nm thickness were simulated. The simulations of the tensile and compressive uniaxial deformations were performed at 10 K, applying engineering strain at a strain rate of ±2.5% /ps. The strain direction was perpendicular to the steps.

The boundaries of the simulation boxes were periodic in the **x** and **y** directions and fixed in the **z** direction.

In the **z** direction the simulated films were bound by a free surface at the top and by a layer of fixed atoms at the bottom to prevent the loss of atoms at the border of the simulation box and to simulate defect-free bulk. The thickness of this frozen layer was 1.2 nm. These atoms were fixed at the positions they had when equilibrated to 10 K and were remapped at every deformation of the simulation box. All the forces acting on these atoms were otherwise reset to zero.

In the **y** direction the size of the simulation box was subject to requirements for periodicity of the terraces and steps for vicinal surfaces. The number of steps and terraces included was 8.

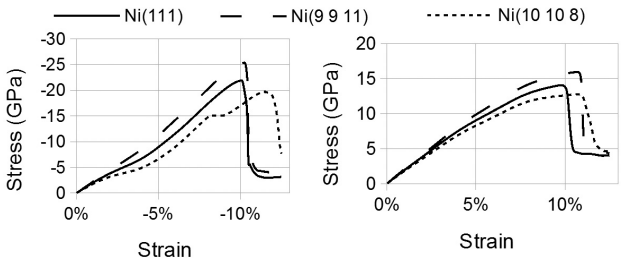
To simulate engineering compressive and tensile strains, the simulation box was deformed in the **y** direction in increments of 0.5 % with 200 fs periods of equilibration in-between, resulting in the overall strain rate of 2.5% /ps. The stress in the **x** direction was kept to zero.

The molecular dynamics simulations were carried out using the LAMMPS Molecular Dynamics Simulator[9] and EAM potentials by Y. Mishin et al.[10] OVITO[11] was used for visualization and analysis of the simulation data. Dislocation detection algorithm by A. Stukowski[11] implemented in OVITO was used in post-processing.

## 3 RESULTS

Deformation mechanisms of copper and nickel (111), (9 9 11) and (10 10 8) surfaces were investigated. Stress-strain curves are shown in **Figures 1** and **2**. As is expected from the direction of the strain, the Young modulus (expressed as the steepness of the stress-strain curve) is highest for the (9 9 11) surfaces and lowest for the (10 10 8) surfaces.

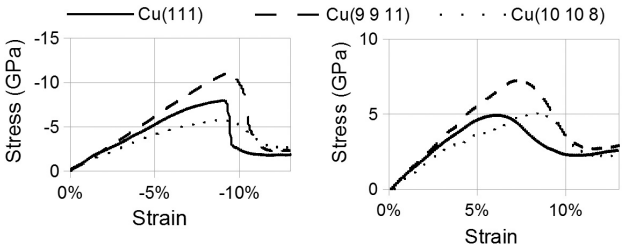
Yield stress is lower in copper than in nickel. Both materials exhibit the yield stress asymmetry, with yield stress being higher in compression than in tension. This is connected to the fact that the deformation mechanisms in compression and tension are not the same for any of the surfaces we investigated, although strict geometric analysis suggests otherwise: primary slip systems, namely {-111}(0-11) and {1-11}(-101), are the same for all the surfaces we investigated, with Schmidt factors of




(a) Nickel, compressive deformation (b) Nickel, tensile deformation

**Figure 1:** a) Stress-strain curves for nickel deformed in compression and b) in tension.

**Slika 1:** Diagrama napetost-raztezek za nikelj; a) pri kompresiji, b) pri napetosti.




(a) Copper, compressive deformation (b) Copper, tensile deformation

**Figure 2:** a) Stress-strain curves for copper deformed in a) compression and b) in tension.

**Slika 2:** Diagrama napetost-raztezek za baker: a) pri kompresiji, b) pri napetosti

0.408 for the (111) surface, 0.377 for (9 9 11) and 0.433 for (10 10 8).

In the case of Cu(111) surface deformed in tension, mostly stair-rod dislocations form throughout the bulk and are not limited to the near-surface region, while in compression, dislocations first nucleate at the surface as Schockley partials and no trailing partials detach from the surface.

In the case of Ni(111) surface deformed in tension, Schockeley partial dislocations nucleate in the bulk, while in compression, Schockley partials nucleate at the surface and trailing partials detach from the surface.

For all the (9 9 11) surfaces, Schockley partial dislocation nucleate at the surface and trailing partials detach from the surface. Stair-rod dislocations form in Cu(9 9 11) and Ni(9 9 11) deformed in tension, **Figures 3b** and **3f**.

In the case of Cu(10 10 8) surface deformed in tension, **Figure 3a**, stair-rod dislocations nucleate at the surface, while in compression, **Figure 3c**, parallel stacking faults nucleate at the steps and grow into the bulk.

In the case of Ni(10 10 8) surface deformed in tension, **Figure 3e**, Schockley partial dislocation nucleate at the surface and in the near-surface region, while in compression, **Figure 3g**, parallel stacking faults nucleate at the steps and grow into the bulk.

## 4 DISCUSSION

We found two cases of easy glide where only one slip system is active: Cu(10 10 8) and Ni(10 10 8) surfaces deformed in compression, **Figures 3c** and **3g**. Schockley partial dislocations nucleate at all the steps on the surface and grow evenly into the bulk. The stress-strain curves have a small plateau in the region just before the peak of the curve is expected, more pronounced in the case of nickel, and the peak is moved to higher strains, **Figures 1a** and **2a**.

In the case of Cu(10 10 8) deformed in tension, **Figure 3a**, Schockley partial dislocations wrapped around stair-rod dislocations form, also nucleating at the steps on the surface. As the stair-rod dislocations only move with diffusion, which is limited at this temperature, the

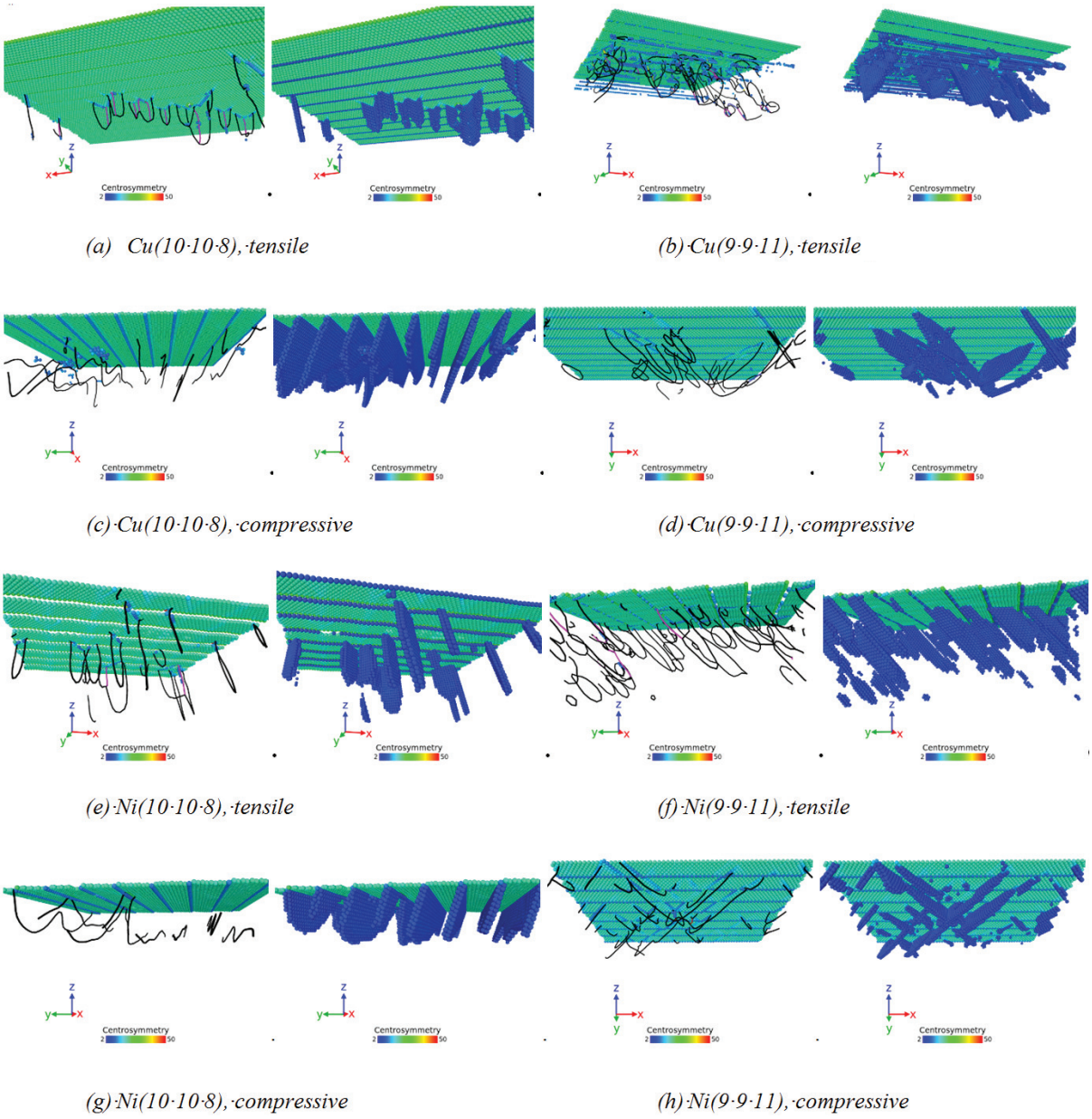



**Figure 3:** Dislocation nucleation in copper and nickel thin films deformed in tension and in compression. Two views are shown for each case: dislocations as lines (left) and atoms with centrosymmetry parameter CS > 2 (right). Black lines denote Schockley partial dislocations and pink lines denote stair-rod dislocations.

**Slika 3:** Začetki plastične deformacije v bakrovih in nikljevih stiskanih in raztezanih tankih filmih. Vsak primer prikazujeta dva pogleda: dislokacije označene s črtami (levo) in atomi s parametrom središčne simetrije CS > 2 (desno). Črne črte označujejo Schocklyeve delne dislokacije, roza črte pa Lomer-Cottrell stike.

effect on stress is the same as if only one slip system were active and the stress-strain curve exhibits a change in slope, **Figure 2b**.

A. Zimmerman et al.[12] studied Au(111) surfaces with single monoatomic steps at 0K and found that when the indenter came into physical contact with the step, the deformation mechanism beneath the indenter switched from dislocation emission from the surface to slip aligned with the step.

D. Shan et al.[13] performed a similar study of nanoindentation on thin copper films and found that when the indenter came into contact with the step, there was a significant difference in the strength of the first dislocation emission.

H. Lu and Y. Ni[14] and H. Lu et al.[15] investigated the effects of surface steps on nanoindentation in Al and found that the shear stress resulting from the step influences the choice of the active slip systems and lowers the threshold for plastic deformation.

Our analysis shows that it is not only the presence of steps that influences deformation mechanisms. While a switch to slip aligned with the steps occurs for the (10 10

8) surfaces deformed in compression for both materials we investigated, we found no such switch for the (9 9 11) surfaces.

The near-surface region is the first to plastically deform and dislocations nucleate at the surface, therefore the surfaces are softer than the bulk. We conclude that the stress inherent in the steps also lowered the threshold for plastic deformation in our systems.

## 5 CONCLUSIONS

Deformation mechanisms of copper and nickel thin films we investigated are more complex than geometric analysis would suggest. The surfaces are softer than the bulk, as the near-surface region is the first to plastically deform and dislocations nucleate at the surface. We conclude that the stress inherent in the steps lowered the threshold for plastic deformation in the thin films we investigated.

In tensile deformation in both materials, stair-rod dislocations nucleate at the surfaces and are not created by dislocation interactions.

The influence of the surface is most pronounced for the cases of the (10 10 8) surfaces deformed in compression, where parallel stacking faults nucleate at the steps on the surfaces in both materials, overriding the primary slip systems. The presence of the steps does not in itself influence the choice of slip systems. While a switch to slip aligned with the steps occurs for the (10 10 8) surfaces deformed in compression for both materials we investigated, we found no such switch for the (9 9 11) surfaces.

### Acknowledgement

The authors acknowledge the financial support of the Slovenian Research Agency (ARRS).

## 6 REFERENCES

[1] P. Muller, Elastic effects on surface physics, Surface Science Reports, 54 (**2004**) 157–258, doi:10.1016/j.surfrep.2004.05.001

[2] Z. You, X. Li, L. Gui, Q. Lu, T. Zhu, H. Gao, L. Lu, Plastic anisotropy and associated deformation mechanisms in nanotwinned metals, Acta Materialia, 61 (**2013**) 217–227, doi:10.1016/j.actamat.2012.09.052

[3] D. Huang, Q. Zhang, P. Qiao, Molecular dynamics evaluation of strain rate and size effects on mechanical properties of FCC nickel nanowires, Computational Materials Science, 50 (**2011**) 903–910, doi:10.1016/j.commatsci.2010.10.028

[4] F. Ma, K.-W. Xu, P. K. Chu, Surface-induced structural transformation in nanowires, Materials Science and Engineering: R: Reports, 74 (**2013**) 173–209, doi:10.1016/j.mser.2013.05.001

[5] D. Spearot, L. Capolungo, J. Qu, M. Cherkaoui, On the elastic tensile deformation of d bicrystal interfaces in copper, Computational Materials Science, 42 (**2008**) 57–67, doi:10.1016/j.commatsci.2007.06.008

[6] M. Chassagne, M. Legros, D. Rodney, Atomic-scale simulation of screw dislocation/coherent twin boundary interaction in Al, Au, Cu and Ni, Acta Materialia, 59 (**2011**) 1456–1463, doi:10.1016/j.actamat.2010.11.007

[7] D. Bachurin, D. Weygand, P. Gumbsch, Dislocation–grain boundary interaction in o textured thin metal films, Acta Materialia, 58 (**2010**) 5232–5241, doi:10.1016/j.actamat.2010.06.026

[8] H. S. Park, K. Gall, J. A. Zimmerman, Deformation of FCC nanowires by twinning and slip, Journal of the Mechanics and Physics of Solids, 54 (**2006**) 1862–1881, doi:10.1016/j.jmps.2006.03.006

[9] S. Plimpton, Fast Parallel Algorithms for Short-Range Molecular Dynamics, Journal of Computational Physics, (**1995**) 1–19, doi:10.1006/jcph.1995.1039, URL http://lammps.sandia.gov/

[10] Y. Mishin, M. Mehl, D. Papaconstantopoulos, A. Voter, J. Kress, Structural stability and lattice defects in copper: Ab initio, tight-binding, and embedded-atom calculations, Physical Review B, 63 (**2001**) 224106, doi:10.1103/PhysRevB.63.224106

[11] A. Stukowski, Visualization and analysis of atomistic simulation data with OVITO–the Open Visualization Tool, Modelling and Simulation in Materials Science and Engineering, 18 (**2010**) 015012, doi:10.1088/0965-0393/18/1/015012

[12] J.A. Zimmerman, C. L. Kelchner, P. A. Klein, J. C. Hamilton, S. M. Foiles, Surface step effects on nanoindentation, Phys. Rev. Lett., 87 (**2001**) 165507, doi:10.1103/PhysRevLett.87.165507

[13] D. Shan, L. Yuan, B. Guo, Multiscale simulation of surface step effects on nanoindentation, Materials Science and Engineering: A, 412 (**2005**) 264–270, doi:10.1016/j.msea.2005.08.198

[14] H. Lu, Y. Ni, Effect of surface step on nanoindentation of thin films by multiscale analysis, Thin Solid Films, 520 (**2012**) 4934–4940, doi:10.1016/j.tsf.2012.03.019

[15] H. Lu, Y. Ni, J. Mei, J. Li, H. Wang, Anisotropic plastic deformation beneath surface step during nanoindentation of FCC Al by multiscale analysis, Computational Materials Science, 58 (**2012**), 192–200, doi:10.1016/j.commatsci.2012.01.026

# References


[1] P. Muller, "Elastic effects on surface physics," *Surface Science Reports*, vol. 54, no. 5-8, pp. 157–258, Aug. 2004. DOI: 10.1016/j.surfrep.2004.05.001.

[2] J. Yang, W. Hu, H. Deng, and D. Zhao, "Temperature dependence of atomic relaxation and vibrations for the vicinal Ni(977) surface: a molecular dynamics study," *Surface Science*, vol. 572, no. 2, pp. 439–448, 2004.

[3] J. Yang and W. Hu, "Anharmonicity in Al vicinal surfaces of (100) with (111) step," 2006.

[4] G. Prévot, C. Cohen, D. Schmaus, P. Hecquet, and B. Salanon, "Temperature dependence of the atomic relaxations and vibrations on a stepped surface: a molecular dynamics study of Cu (1, 1, 19)," *Surface science*, vol. 506, pp. 272–286, 2002.

[5] G. Prévot and B. Croset, "Elastic relaxations and interactions on metallic vicinal surfaces: testing the dipole model," *Physical Review B*, vol. 74, p. 235 410, 2006.

[6] J. Yang, W. Hu, H. Deng, and D. Zhao, "Temperature dependence of atomic relaxation and vibrations for the vicinal Ni(9 7 7) surface: a molecular dynamics study," *Surface Science*, vol. 572, no. 2–3, pp. 439–448, 2004. DOI: 10.1016/j.susc.2004.09.027.

[7] H. Yıldırım and S. Durukanoğlu, "Structural relaxations of cu vicinals," *Surface Science*, vol. 557, no. 1–3, pp. 190–200, 2004. DOI: 10.1016/j.susc.2004.03.035.

[8] D. Spišák, "Structure and energetics of Cu(1 0 0) vicinal surfaces," *Surface Science*, vol. 489, no. 1–3, pp. 151–160, 2001. DOI: 10.1016/S0039-6028(01)01173-6.

[9] A. Ferre-Vilaplana, R. Gisbert, and E. Herrero, "On the electrochemical properties of platinum stepped surfaces vicinal to the (100) pole. a computational study," *Electrochimica Acta*, vol. 125, pp. 666–673, 2014. DOI: 10.1016/j.electacta.2014.01.138.

[10] J. Xu, A.-E.-A. A. Abd-El-Latif, Y.-X. Chen, and H. Baltruschat, "Electrodeposition of silver on stepped platinum electrode surfaces with (1 0 0)-oriented terraces: generation of confined reaction sites," *Journal of Electroanalytical Chemistry*, vol. 716, pp. 93–100, 2014, Special Issue in Honour of Kingo Itaya. DOI: 10.1016/j.jelechem.2013.11.036.

[11] P. J. Godowski and J. Onsgaard, "Adsorption of NO on potassium-modified Cu(100) vicinal surfaces," *Vacuum*, vol. 94, pp. 6–13, 2013. DOI: /10.1016/j.vacuum.2013.01.011.

[12] A. M. Gómez-Marín and J. M. Feliu, "Thermodynamic properties of hydrogen–water adsorption at terraces and steps of Pt(111) vicinal surface electrodes," *Surface Science*, vol. 646, pp. 269–281, 2016, Surface science for heterogeneous catalysis, a special issue in Honour of Richard Lambert. DOI: 10.1016/j.susc.2015.10.003.

[13] P. Rodriguez, N. García-Aráez, E. Herrero, and J. Feliu, "New insight on the behavior of the irreversible adsorption and underpotential deposition of thallium on platinum (111) and vicinal surfaces in acid electrolytes," *Electrochimica Acta*, vol. 151, pp. 319–325, 2015. DOI: 10.1016/j.electacta.2014.11.019.

[14] L. Wang, Z. Zhang, and X. Han, "In situ experimental mechanics of nanomaterials at the atomic scale," *NPG Asia Materials*, no. 5, e40, 2013.

[15] D. Spearot, L. Capolungo, J. Qu, and M. Cherkaoui, "On the elastic tensile deformation of <100> bicrystal interfaces in copper," *Computational Materials Science*, vol. 42, no. 1, pp. 57–67, Mar. 2008. DOI: 10.1016/j.commatsci.2007.06.008.

[16] M. Chassagne, M. Legros, and D. Rodney, "Atomic-scale simulation of screw dislocation/coherent twin boundary interaction in Al, Au, Cu and Ni," *Acta Materialia*, vol. 59, no. 4, pp. 1456–1463, 2011.

[17] D. Bachurin, D. Weygand, and P. Gumbsch, "Dislocation–grain boundary interaction in <111> textured thin metal films," *Acta Materialia*, vol. 58, no. 16, pp. 5232–5241, Sep. 2010. DOI: 10.1016/j.actamat.2010.05.037.

[18] Z. You, X. Li, L. Gui, Q. Lu, T. Zhu, H. Gao, and L. Lu, "Plastic anisotropy and associated deformation mechanisms in nanotwinned metals," *Acta Materialia*, vol. 61, no. 1, pp. 217–227, Jan. 2013. DOI: 10.1016/j.actamat.2012.09.052.

[19] Z. Shan, E. A. Stach, J. M. K. Wiezorek, J. A. Knapp, D. M. Follstaedt, and S. X. Mao, "Grain boundary-mediated plasticity in nanocrystalline nickel," *Science*, vol. 305, no. 5684, pp. 654–657, 2004. DOI: 10.1126/science.1098741.

[20] X. Z. Liao, S. G. Srinivasan, Y. H. Zhao, M. I. Baskes, Y. T. Zhu, F. Zhou, E. J. Lavernia, and H. F. Xu, "Formation mechanism of wide stacking faults in nanocrystalline Al," *Applied Physics Letters*, vol. 84, no. 18, pp. 3564–3566, 2004. DOI: 10.1063/1.1734689.

[21] M. Tschopp, G. Tucker, and D. McDowell, "Atomistic simulations of tension–compression asymmetry in dislocation nucleation for copper grain boundaries," *Computational Materials Science*, vol. 44, no. 2, pp. 351–362, 2008.

[22] V. Yamakov, D. Wolf, S. R. Phillpot, A. K. Mukherjee, and H. Gleiter, "Dislocation processes in the deformation of nanocrystalline aluminium by molecular-dynamics simulation," *Nature Materials*, vol. 1, no. 1, pp. 45–49, 2002. DOI: 10.1038/nmat700.

[23] V. Yamakov, D. Wolf, S. Phillpot, and H. Gleiter, "Deformation twinning in nanocrystalline Al by molecular-dynamics simulation," *Acta Materialia*, vol. 50, no. 20, pp. 5005–5020, 2002. DOI: 10.1016/S1359-6454(02)00318-X.

[24] M. Chen, E. Ma, K. J. Hemker, H. Sheng, Y. Wang, and X. Cheng, "Deformation twinning in nanocrystalline aluminum," *Science*, vol. 300, no. 5623, pp. 1275–1277, 2003.

[25] D. E. Spearot, K. I. Jacob, and D. L. McDowell, "Nucleation of dislocations from [001] bicrystal interfaces in aluminum," *Acta Materialia*, vol. 53, no. 13, pp. 3579–3589, Aug. 2005. DOI: 10.1016/j.actamat.2005.04.012.

[26] L. Yuan, Z. Xu, D. Shan, and B. Guo, "Molecular dynamics study on the equal biaxial tension of Cu/Ag bilayer films," *Applied Surface Science*, vol. 282, pp. 450–455, 2013.

[27] Y. Choi, K. J. Van Vliet, J. Li, and S. Suresh, "Size effects on the onset of plastic deformation during nanoindentation of thin films and patterned lines," *Journal of Applied Physics*, vol. 94, no. 9, p. 6050, 2003. DOI: 10.1063/1.1615702.

[28] T. Zhu, "Predictive modeling of nanoindentation-induced homogeneous dislocation nucleation in copper," *Journal of the Mechanics and Physics of Solids*, vol. 52, no. 3, pp. 691–724, Mar. 2004. DOI: 10.1016/j.jmps.2003.07.006.

[29] E. Lilleodden, J. Zimmerman, S. Foiles, and W. Nix, "Atomistic simulations of elastic deformation and dislocation nucleation during nanoindentation," *Journal of the Mechanics and Physics of Solids*, vol. 51, no. 5, pp. 901–920, May 2003. DOI: 10.1016/S0022-5096(02)00119-9.

[30] I. Salehinia and S. N. Medyanik, "Effects of Vacancies on the Onset of Plasticity in Metals—An Atomistic Simulation Study," *Metallurgical and Materials Transactions A*, vol. 42, no. 13, pp. 3868–3874, Mar. 2011. DOI: 10.1007/s11661-011-0653-8.

[31] C.-M. Tan and Y.-R. Jeng, "Computer simulations of nanoindentation on Cu (111) with a void," *International Journal of Solids and Structures*, vol. 46, no. 9, pp. 1884–1889, May 2009. DOI: 10.1016/j.ijsolstr.2008.12.022.

[32] H. Jang and D. Farkas, "Interaction of lattice dislocations with a grain boundary during nanoindentation simulation," *Materials Letters*, vol. 61, no. 3, pp. 868–871, Feb. 2007. DOI: 10.1016/j.matlet.2006.06.004.

[33] J. A. Zimmerman, C. L. Kelchner, P. A. Klein, J. C. Hamilton, and S. M. Foiles, "Surface step effects on nanoindentation," *Phys. Rev. Lett.*, vol. 87, p. 165 507, 16 Oct. 2001.

[34] D. Shan, L. Yuan, and B. Guo, "Multiscale simulation of surface step effects on nanoindentation," *Materials Science and Engineering: A*, vol. 412, no. 1-2, pp. 264–270, Dec. 2005. DOI: 10.1016/j.msea.2005.08.198.

[35] H. Lu and Y. Ni, "Effect of surface step on nanoindentation of thin films by multiscale analysis," *Thin Solid Films*, vol. 520, no. 15, pp. 4934–4940, 2012. DOI: 10.1016/j.tsf.2012.03.019.

[36] H. Lu, Y. Ni, J. Mei, J. Li, and H. Wang, "Anisotropic plastic deformation beneath surface step during nanoindentation of FCC al by multiscale analysis," *Computational Materials Science*, vol. 58, pp. 192–200, 2012. DOI: 10.1016/j.commatsci.2012.01.026.

[37] D. Huang, Q. Zhang, and P. Qiao, "Molecular dynamics evaluation of strain rate and size effects on mechanical properties of FCC nickel nanowires," *Computational Materials Science*, vol. 50, no. 3, pp. 903–910, Jan. 2011. DOI: 10.1016/j.commatsci.2010.10.028.

[38] A. Setoodeh, H. Attariani, and M. Khosrownejad, "Nickel nanowires under uniaxial loads: A molecular dynamics simulation study," *Computational Materials Science*, vol. 44, no. 2, pp. 378–384, Dec. 2008. DOI: 10.1016/j.commatsci.2008.03.035.

[39] Y.-H. Wen, Z.-Z. Zhu, G.-F. Shao, and R.-Z. Zhu, "The uniaxial tensile deformation of Ni nanowire: atomic-scale computer simulations," *Physica E: Low-dimensional Systems and Nanostructures*, vol. 27, no. 1-2, pp. 113–120, Mar. 2005. DOI: 10.1016/j.physe.2004.10.009.

[40] F. Ma, K.-W. Xu, and P. K. Chu, "Surface-induced structural transformation in nanowires," *Materials Science and Engineering: R: Reports*, vol. 74, no. 6, pp. 173–209, Jun. 2013. DOI: 10.1016/j.mser.2013.05.001.

[41] H. S. Park, K. Gall, and J. a. Zimmerman, "Deformation of FCC nanowires by twinning and slip," *Journal of the Mechanics and Physics of Solids*, vol. 54, no. 9, pp. 1862–1881, Sep. 2006. DOI: 10.1016/j.jmps.2006.03.006.

[42] H. Van Swygenhoven, P. Derlet, and a.G. Frøseth, "Nucleation and propagation of dislocations in nanocrystalline fcc metals," *Acta Materialia*, vol. 54, no. 7, pp. 1975–1983, Apr. 2006. DOI: 10.1016/j.actamat.2005.12.026.

[43] H. Van Swygenhoven and J. R. Weertman, "Deformation in nanocrystalline metals," *Materials Today*, vol. 9, no. 5, pp. 24–31, 2006.

[44] T. Shimokawa, A. Nakatani, and H. Kitagawa, "Grain-size dependence of the relationship between intergranular and intragranular deformation of nanocrystalline al by molecular dynamics simulations," *Physical Review B*, vol. 71, no. 22, 224110, p. 224 110, Jun. 2005. DOI: 10.1103/PhysRevB.71.224110.

[45] Y. Mishin, D. Farkas, M. J. Mehl, and D. A. Papaconstantopoulos, "Interatomic potentials for monoatomic metals from experimental data and *ab initio* calculations," *Phys. Rev. B*, vol. 59, pp. 3393–3407, 5 Feb. 1999. DOI: 10.1103/PhysRevB.59.3393. [Online]. Available: http://link.aps.org/doi/10.1103/PhysRevB.59.3393.

[46] Y. Mishin, M. Mehl, D. Papaconstantopoulos, a. Voter, and J. Kress, "Structural stability and lattice defects in copper: Ab initio, tight-binding, and embedded-atom calculations," *Physical Review B*, vol. 63, no. 22, p. 224 106, May 2001. DOI: 10.1103/PhysRevB.63.224106.

[47] S. Plimpton, "Fast Parallel Algorithms for Short-Range Molecular Dynamics," *Journal of Computational Physics*, no. 117, pp. 1–19, 1995, http://lammps.sandia.gov.

[48] D. Sheppard, R. Terrell, and G. Henkelman, "Optimization methods for finding minimum energy paths.," *The Journal of chemical physics*, vol. 128, no. 13, p. 134 106, Apr. 2008. DOI: 10.1063/1.2841941.

[49] W. D. J. Callister, *Fundamentals of materials science and engineering*. The Univeristy of Utah, Department of metalurgical engineering, 2001, ISBN: 047139551X.

[50] C. L. Kelchner, S. J. Plimpton, and J. C. Hamilton, "Dislocation nucleation and defect structure during surface indentation," *Physical Review B*, vol. 58, pp. 11 085–11 088, 17 Nov. 1998. DOI: 10.1103/PhysRevB.58.11085.

[51] R. W. Cahn and P. Haasen, Eds., *Physical Metallurgy*, Fourth, revised and ehanced edition. Elsevier Science B.V., 1996.

[52] M. F. de Campos, "Selected values for the stacking fault energy of face centered cubic metals," in *Advanced Powder Technology VI*, ser. Materials Science Forum, vol. 591, Trans Tech Publications, Oct. 2008, pp. 708–711. DOI: 10.4028/www.scientific.net/MSF.591-593.708.

[53] B. Liu and Y. Huang, "The Stable Finite Element Method for Minimization Problems," *Journal of Computational and Theoretical Nanoscience*, vol. 5, no. 7, pp. 1251–1254, Jul. 2008. DOI: 10.1166/jctn.2008.007.

[54] W. C. Swope, H. C. Andersen, P. H. Berens, and K. R. Wilson, "A computer simulation method for the calculation of equilibrium constants for the formation of physical clusters of molecules: Application to small water clusters," *The Journal of Chemical Physics*, vol. 76, pp. 637–649, Jan. 1982. DOI: 10.1063/1.442716.

[55] N. Ashcroft and N. Mermin, *Solid State Physics*. Cengage Learning, 2011, ISBN: 9788131500521.

[56] F. Ercolessi, M. Parrinello, and E. Tosatti, "Simulation of gold in the glue model," *Philosophical magazine A*, vol. 58, no. 1, pp. 213–226, 1988.

[57] F. H. Stillinger and T. A. Weber, "Computer simulation of local order in condensed phases of silicon," *Phys. Rev. B*, vol. 31, pp. 5262–5271, 8 Apr. 1985. DOI: 10.1103/PhysRevB.31.5262.

[58] M. S. Daw, S. M. Foiles, and M. I. Baskes, "The embedded-atom method: a review of theory and applications," *Materials Science Reports*, vol. 9, no. 7, pp. 251–310, 1993.

[59] S. Corporation, *Lammps documentation*, http://lammps.sandia.gov/doc/Manual.html, Mar. 2017.

[60] A. Stukowski, "Visualization and analysis of atomistic simulation data with OVITO–the Open Visualization Tool," en, *Modelling and Simulation in Materials Science and Engineering*, vol. 18, no. 1, p. 015 012, Jan. 2010. DOI: 10.1088/0965-0393/18/1/015012.

[61] A. Stukowski, V. V. Bulatov, and A. Arsenlis, "Automated identification and indexing of dislocations in crystal interfaces," *Modelling and Simulation in Materials Science and Engineering*, vol. 20, no. 8, p. 085 007, 2012.

[62] T. Williams, C. Kelley, and et al., *Gnuplot 4.4: an interactive plotting program*, http://gnuplot.sourceforge.net/, Mar. 2011.

[63] H. L. Davis and J. R. Noonan, "Multilayer relaxation in metallic surfaces as demonstrated by leed analysis," *Surface Science*, vol. 126, pp. 245–252, Mar. 1983. DOI: 10.1016/0039-6028(83)90717-3.

[64] D. Adams, H. Nielsen, and J. Andersen, "Oscillatory relaxation of the cu(110) surface," *Surface Science*, vol. 128, no. 2, 1983. DOI: 10.1016/S0039-6028(83)80033-8.

[65] Y. Gauthier, R. Baudoing, C. Gaubert, and L. Clarke, "Extensive leed analysis of ni(110). i. experiment," *Journal of Physics C: Solid State Physics*, vol. 15, no. 14, p. 3223, 1982.

[66] D. L. Adams, L. E. Petersen, and C. S. Sorensen, "Oscillatory relaxation of the ni(110) surface: a leed study," *Journal of Physics C: Solid State Physics*, vol. 18, no. 8, p. 1753, 1985.

[67] R. W. Armstrong and S. M. Walley, "High strain rate properties of metals and alloys," *International Materials Reviews*, vol. 53, no. 3, pp. 105–128, 2008.

[68] N. Pukšič, M. Jenko, M. Godec, and P. J. McGuiness, "A comparison of the uniaxial deformation of copper and nickel (1 1 19) surfaces: a molecular dynamics study," *Scientific Reports*, no. 7, p. 42 234, 2017. DOI: 10.1038/srep42234.

[69] E. P. Degarmo, J. Black, and R. A. Kohser, *Materials and Processes in Manufacturing (9th ed.)* Wiley, 2003, ISBN: 0-471-65653-4.

[70] N. Pukšič, M. Jenko, and M. Godec, "Molecular dynamics simulations of plastic deformation of metallic surfaces," *Materials and Technology*, vol. 51, no. 1, pp. 153–156, 2017. DOI: 10.17222/mit.2016.334.

[71] D. Kiener, W. Grosinger, G. Dehm, and R. Pippan, "A further step towards an understanding of size-dependent crystal plasticity: in situ tension experiments of miniaturized single-crystal copper samples," *Acta Materialia*, vol. 56, no. 3, pp. 580–592, 2008. DOI: 10.1016/j.actamat.2007.10.015.

# Bibliography

## Publications Related to the Thesis

### Journal Articles

N. Pukšič, M. Jenko, and M. Godec, "Molecular dynamics simulations of plastic deformation of metallic surfaces," *Materials and Technology*, vol. 51, no. 1, pp. 153–156, 2017. DOI: 10.17222/mit.2016.334.

N. Pukšič, M. Jenko, M. Godec, and P. J. McGuiness, "A comparison of the uniaxial deformation of copper and nickel (1 1 19) surfaces: a molecular dynamics study," *Scientific Reports*, no. 7, p. 42 234, 2017. DOI: 10.1038/srep42234.

### Conference Paper

N. Pukšič, M. Jenko, and M. Godec, "Molecular dynamics study of incipient plasticity of the (1,1,19) nickel surface," in *Proceedings of the 4th Jožef Stefan International Postgraduate School Students Conference*, N. Trdin, J. Pavlič, B. Cvetković, N. Aničić, M. Pavlin, and A. Rešetič, Eds., Ljubljana: Mednarodna podiplomska šola Jožefa Stefana, 2014.

## Other Publications

### Journal Articles

A. Bytyqi, N. Pukšič, M. Jenko, and M. Godec, "Characterization of the inclusions in spring steel using light microscopy and scanning electron microscopy," *Materials and Technology*, vol. 45, no. 1, pp. 55–59, 2011.

J. A. Montoya, G. Figueroa, and N. Pukšič, "Profile Likelihood Estimation of the Vulnerability P(X>v) and the Mixing Proportion p Parameters in the Gumbel Mixture Model," *Revista Colombiana de Estadistica*, vol. 36, no. 2, pp. 193–208, 2013.

### Conference Paper

N. Pukšič and M. Jenko, "Estimating the size of the maximum inclusion in a large sample area of steel," in *Proceedings of the 4th Jožef Stefan International Postgraduate School Students Conference*, D. Petelin, A. Tavčar, and B. Kaluža, Eds., Ljubljana: Mednarodna podiplomska šola Jožefa Stefana, 2012.

# Biography

Nuša Pukšič studied physics at the Faculty of Mathematics and Physics, University of Ljubljana, concluding her studies in 2010 with a Bachelor's degree and the thesis entitled "A comparative analysis of the 51CrV4 alloy and structuring of the results". The work was done under the supervision of Prof. Dr. Janez Dolinšek, Faculty of Mathematics and Physics, University of Ljubljana, and Prof. Dr. Monika Jenko, Institute of Metals and Technology, IMT, Ljubljana. The results and the subsequent work on this subject were published in two articles and one proceedings paper.

She had a scholarship from the Institute of Metals and Technology, IMT, Ljubljana from 2006 to 2010 and has been employed there from 2010 to 2016 as a young researcher. In 2010 she had also enrolled in the Nanosciences and Nanotechnologies doctoral study program at the Jožef Stefan International Postgraduate School and started her work in the field of molecular dynamics simulations of metallic materials.

She had also attended an extra-curricular course on ThermoCalc Software, used in modeling of thermodynamic properties of complex alloys.

She concluded her coursework at the Jožef Stefan International Postgraduate School in 2015 with an average grade of 9.95.